Reporter Review: Magnetospheric ULF Waves

Frederick Menk

University of Newcastle, Australia

Structure of the Review

1. ULF Wave Sources

Solar wind; boundary instabilities; nightside

2. Wave Generation and Propagation

Global modes; field line resonances; poloidal modes; other modes; Pi2

3. EMIC Waves

New theoretical developments; new observations

4. The Ionospheric Boundary

Effects on ULF waves; IAR; effects of waves on ionosphere

5. Applications

Magnetospheric remote sensing; transport and acceleration of particles; loss of energetic particles; other applications

Notation

AG=Ann. Geophys., GRL=Geophys.Res.Lett.; JGR=J.Geophys.Res.; JASTP=J.Atmos.Solar-Terr.Phys.; PSS=Planet.Space.Sci.

Scope

Examined ~300 papers published over past ~4 years with ‘ULF waves’ or similar in title or abstract. However, important and favourite papers will no doubt have been missed.

This review does not cover auroral and substorm effects, waves at other planets, and the spectrum of wave-particle interactions, which are dealt with elsewhere.

Most work shown here is post-2008. A review up to 2010 entitled “Magnetospheric ULF Waves: A Review”, is in *The Dynamic Magnetosphere*, eds. M. Fujimoto and W. Liu, Springer, arising from the 2009 IAGA meeting.

In past 2 years much new work has focused on analysis of multipoint (Cluster, THEMIS) spacecraft observations, and observations and modelling of EMIC wave generation.

1.1 Wave Sources – Solar Wind

Summary

Statistical and event studies show that periodic variations in solar wind dynamic pressure may stimulate magnetospheric Pc5 waves and FLRs, especially at discrete 'magic' frequencies (0.7, 1.4, 2.0, 4.8 mHz) [Ghosch et al., JGR 2009; Mthembu et al., AG 2009; Viall et al., JGR 2009; Claudepierre et al., GRL 2009, JGR 2010; Stephenson & Walker, AG 2010; Zhang et al., JGR 2010; Villante & Piersanti, JASTP 2011].

- Why would such discrete frequencies be present in the solar wind?
- How important are these as a source of 'everyday' Pc5 and other ULF waves?

1.1 Wave Sources – Solar Wind

Summary (cont).

Multipoint observations show evidence of upstream waves entering and propagating through the magnetosphere as compressional waves [Constantinescu et al., AG 2007; Heilig et al., AG 2007; Clausen et al., JGR 2008].

Statistical studies confirm that Pc4-5 power is strongly related to solar wind speed [Pahud et al., JASTP 2009; Liu et al., JGR 2010]. Multiple regression analysis shows that several parameters play a role, including IMF B_z for Pc5 [Simms et al., JGR 2010] and solar wind density for Pc3 [De Lauretis et al., JGR 2010; Heilig et al., AG 2010].

- Is solar wind speed or pressure NV^2 more important?
- Do we now have robust empirical models for nowcasting Pc3 and Pc5 activity? Can these be used in radiation belt models?

Wave Sources – Solar Wind

Viall et al. [JGR 2009] looked for common spectral peaks in 11 yrs of WIND and GOES data.

They used phase coherence and narrow band tests on 6-hr intervals per 3-yr blocks. They found discrete 'magic' frequencies are seen in the magnetosphere 54% of the time they occur in solar wind.

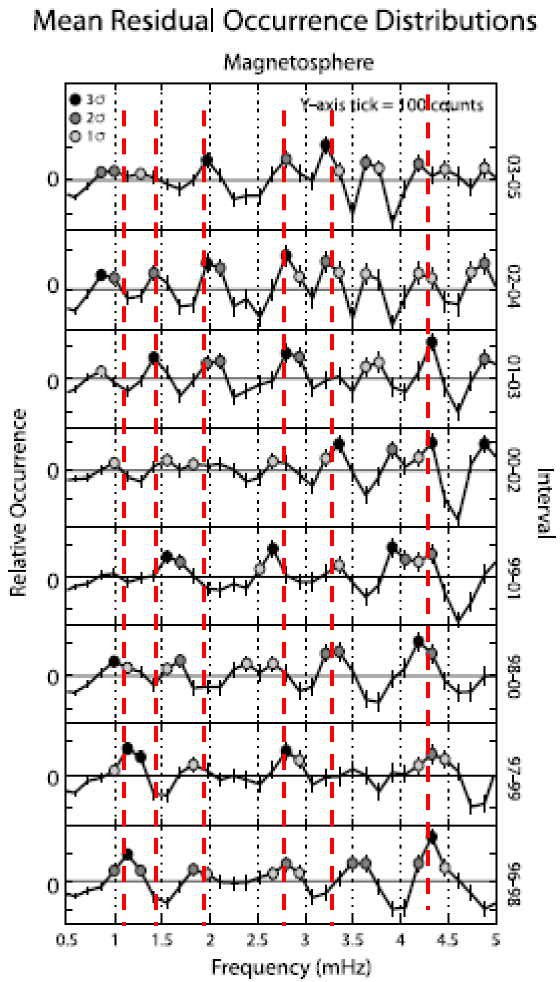

Figure 5. Mean residuals of 3-year occurrence distributions of discrete frequencies found in the dayside magnetosphere from 1996 to 2005. Vertical lines at each frequency indicate ±1 standard deviation of the residual at that frequency, and dots indicate statistically significant occurrence enhancements at the 1 (light gray), 2 (dark gray), and 3 (black) standard deviation thresholds. *y* axis tick marks indicate 100 counts. The horizontal line indicates a mean residual value of zero.

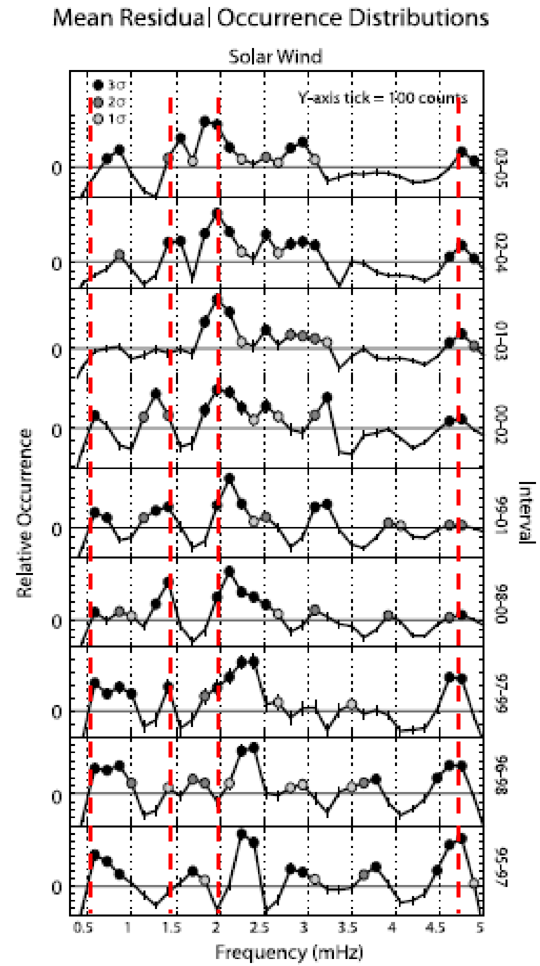

Figure 4. Mean residuals of 3-year occurrence distributions of all statistically significant frequencies for 1995–2005 found in the solar wind number density. Vertical lines at each frequency indicate ±1 standard deviation of the residual at that frequency, and dots indicate statistically significant occurrence enhancements at the 1 (light gray), 2 (dark gray), and 3 (black) standard deviation thresholds. *y* axis tick marks indicate 100 counts. The horizontal line indicates a mean residual value of zero.

Wave Sources – Solar Wind

Time series and wavelet spectra of 1.9 mHz FLR detected with the Goose Bay radar and oscillations at WIND suggest they are causally related [Mthembu et al., AG 2009].

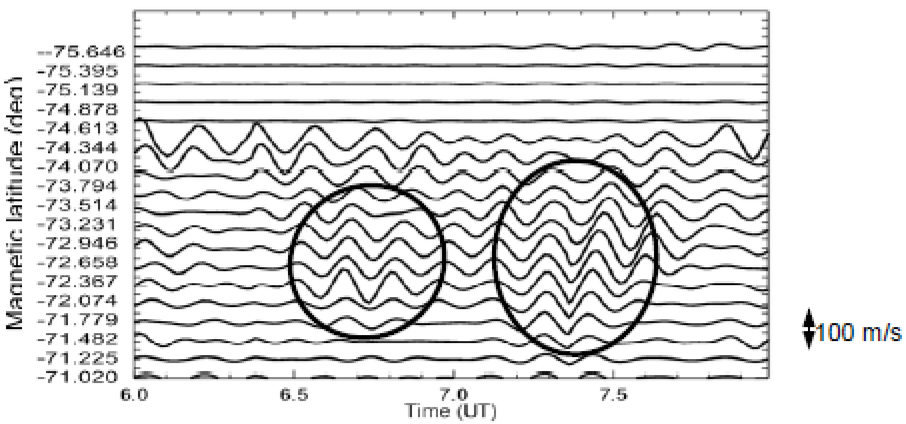

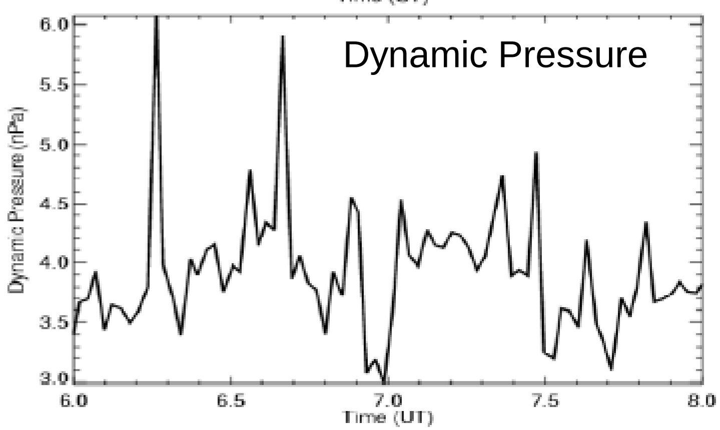

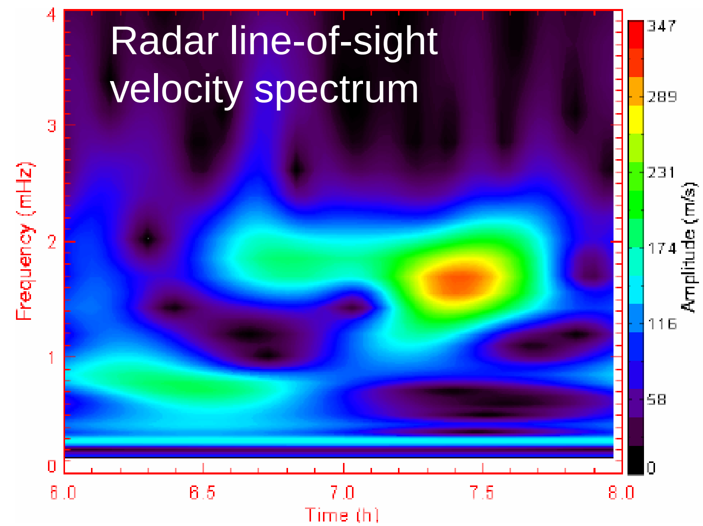

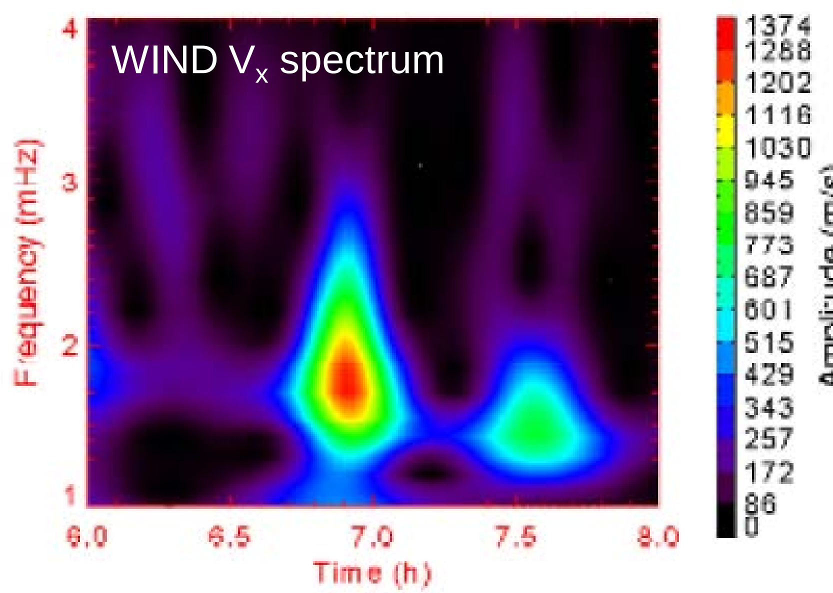

Wave Sources – Solar Wind

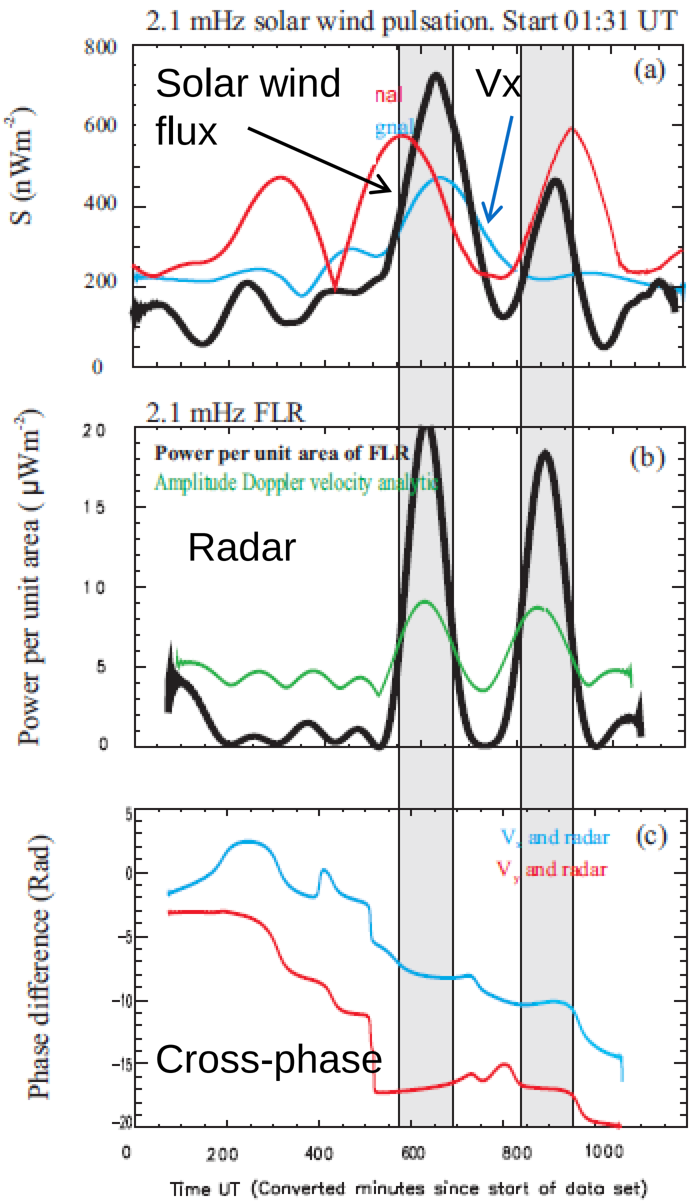

Multi-taper spectrum analysis of 2.1 mHz oscillations detected upstream and by the SHARE HF radar at SANAE [Stephenson & Walker, AG 2010]. Top: solar wind; middle: FLR power; bottom: solar wind-radar cross-phase.

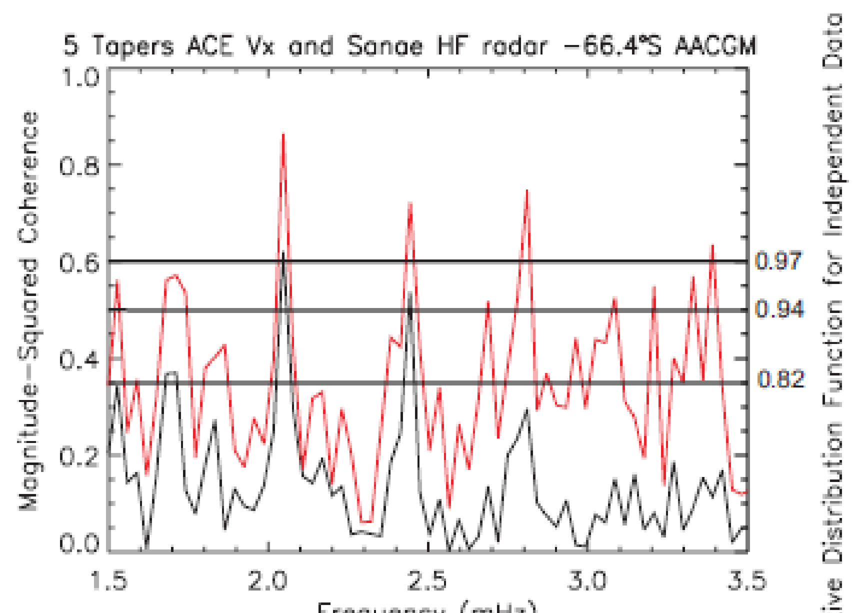

ACE V_x and HF radar coherence estimates.

Wave Sources – Solar Wind

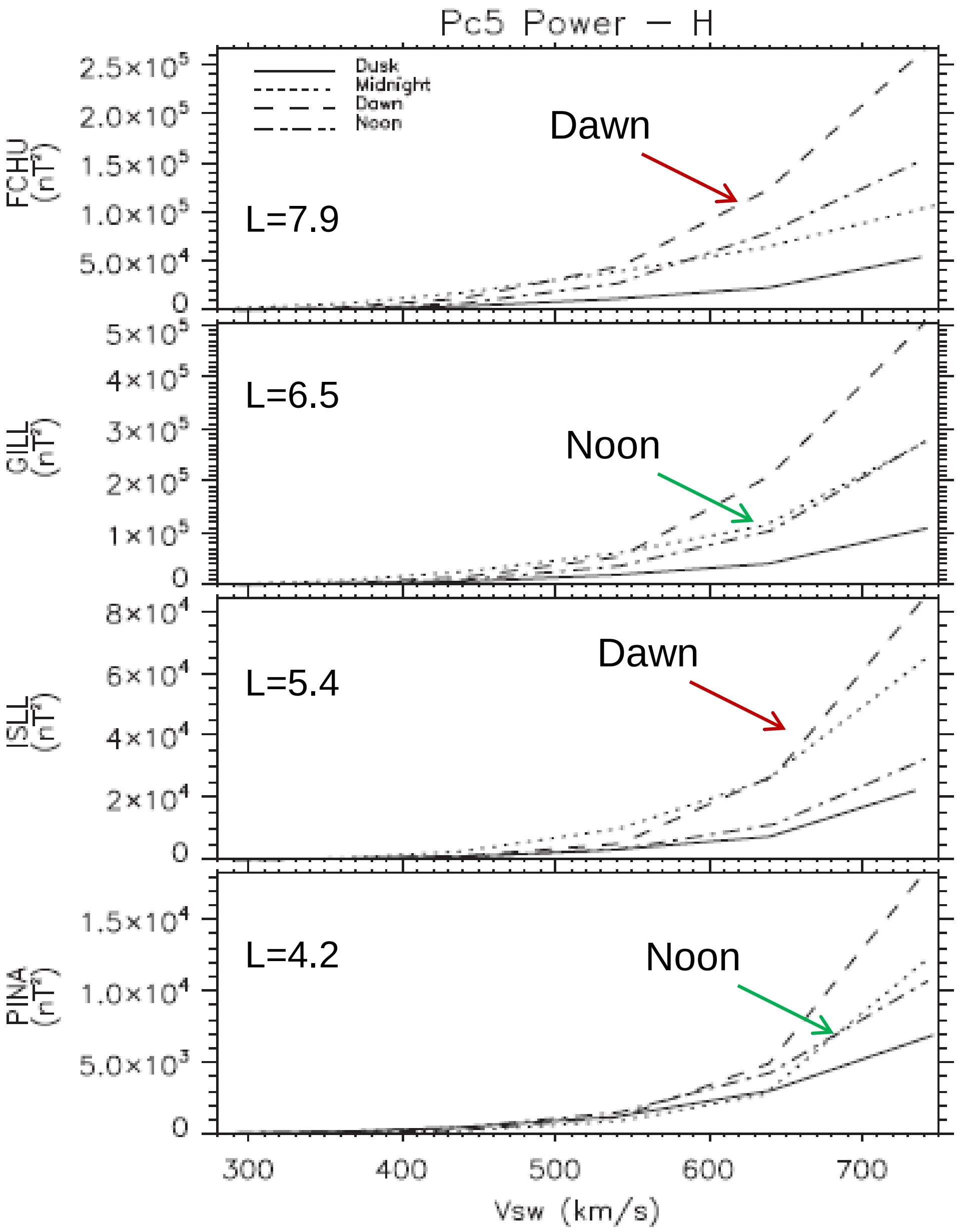

Pc5 wave power (measured here over 20 years) is strongly related to solar wind velocity over a range of L and LT [Pahud et al., JASTP 2009].

Wave Sources – Solar Wind

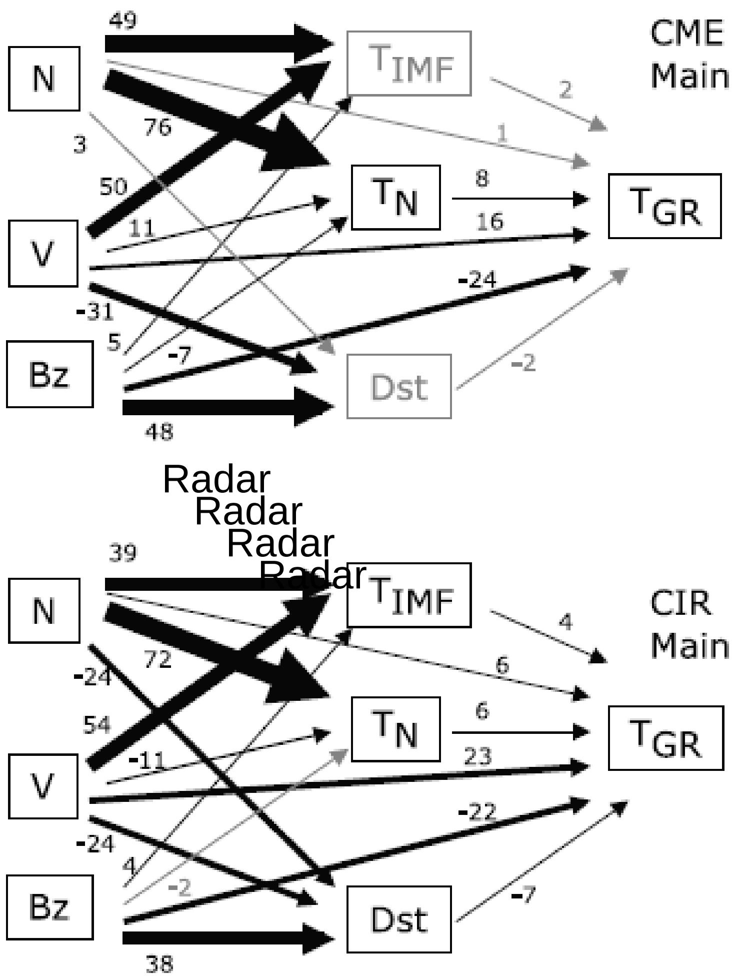

Path diagrams showing correlation between hourly ground level 2-7 mHz wave index T_{GR} and solar wind parameters for main phases of 169 CME storms and 208 CIR storms [Simms et al., JGR 2010]. T_N and T_{IMF} are satellite-based ULF variability indices. Line thickness relates to partial regression coefficients.

A multiple regression model combining all these dependencies gives

$\log_{10} T_{GR} \approx 0.80$ for CME storms
$\log_{10} T_{GR} \approx 0.71\text{-}0.77$ for CIR storms.

Wave Sources – Solar Wind

$$\mathrm{Pc3ind} = C \cdot p_1^{\alpha 1} \cdot p_2^{\alpha 2} \cdot \ldots \cdot p_n^{\alpha_n} + D,$$

4-D MLRs for different years ($\mathrm{Pc3ind} = C v_{\mathrm{sw}}^{\alpha 1} N_{\mathrm{p}}^{\alpha 2} (\cos\vartheta_{Bx} + 2)^{\alpha 3} \cos^{\alpha 4}\chi + D$).

THY	2001	2002	2003	2004	2005	2006	2007
v_{sw}	2.88	3.20	3.26	3.23	2.48	3.53	3.50
N_{p}	0.57	0.62	0.63	0.60	0.47	0.56	0.56
$\cos\vartheta_{Bx}+2$	2.99	2.93	3.07	3.21	2.31	2.98	2.66
$\cos\chi$	0.23	0.23	0.21	0.17	0.16	0.15	0.14
$\log_{10} C$	−7.34	−8.17	−8.37	−8.41	−5.85	−9.12	−8.92
D	1	5	4	6	7	1	−2
R	0.71	0.74	0.76	0.75	0.69	0.76	0.80

4-D MLRs, 2003, MM100 stations ($\mathrm{Pc3ind} = C v_{\mathrm{sw}}^{\alpha 1} N_{\mathrm{p}}^{\alpha 2} (\cos\vartheta_{Bx} + 2)^{\alpha 3} \cos^{\alpha 4}\chi + D$).

2003	THY	BEL	TAR	NUR	HAN	SOD	KIL
v_{sw}	3.26	2.08	2.66	2.85	2.86	2.49	2.70
N_{p}	0.63	0.27	0.48	0.54	0.54	0.46	0.50
$\cos\vartheta_{Bx}+2$	3.07	2.29	2.27	2.35	2.32	1.66	1.56
$\cos\chi$	0.21	0.22	0.18	0.14	0.11	0.06	0.04
$\log_{10} C$	−8.38	−4.22	−6.16	−6.68	−6.73	−5.34	−5.94
D	4	−31	−6	1	2	59	93
R	0.76	0.75	0.65	0.65	0.65	0.46	0.45

Multiple regression analysis of Pc3 activity and solar wind parameters [Heilig et al., AG 2010] at L=1.84 (top), and stations from L=1.8 to L=6.1 (bottom).

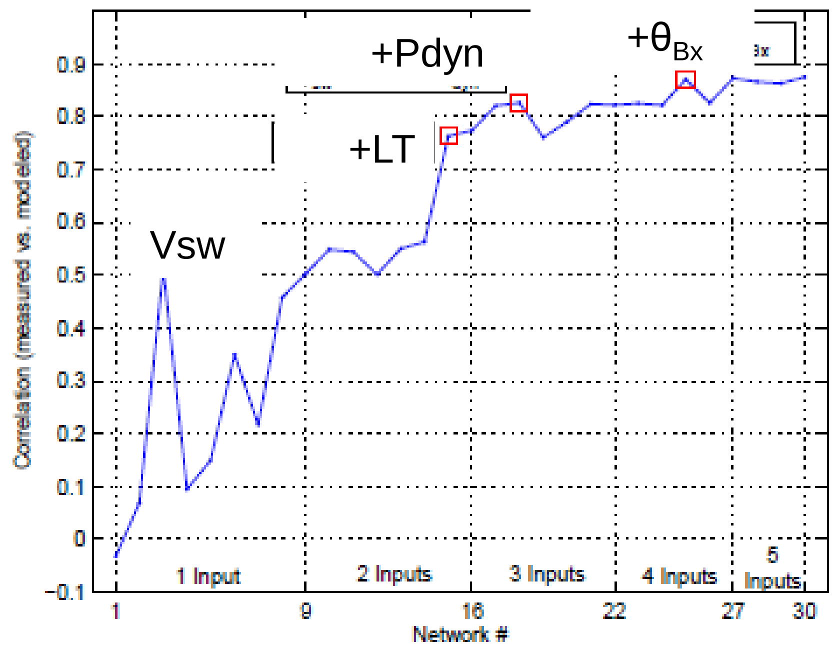

Outcome of neural network wrapper training and evaluation for a range of parameters.

1.2 Wave Sources – Boundary Instabilities

Summary

Global 3-D MHD simulations show that at constant solar wind speed two coupled modes of KHI surface waves may be generated near the magnetopause flanks [Claudepierre et al., JGR 2008]. Multipoint spacecraft observations reveal standing surface waves at the magnetopause, especially at ‘magic’ Pc5 frequencies [Plaschke et al., GRL 2009] and highlight the role of the KHI near the flanks at solar minimum [Liu et al., JGR 2009].

Directional discontinuities (accompanying shocks) may cause changes in azimuthal flow direction in the solar wind which can excite KH waves at the magnetopause [Farrugia et al., JGR 2008; Farrugia & Gratton, JASTP 2011].

- How important are boundary instabilities as sources of ‘everyday’ ULF wave activity?
- How important are solar wind discontinuities in this regard?

Wave Sources – Boundary Instabilities

Claudepierre et al. [JGR 2008]. Global MHD simulations in the GSM equatorial plane for different solar wind speeds (right); resultant radial power profiles (bottom right); and wavenumber profiles.

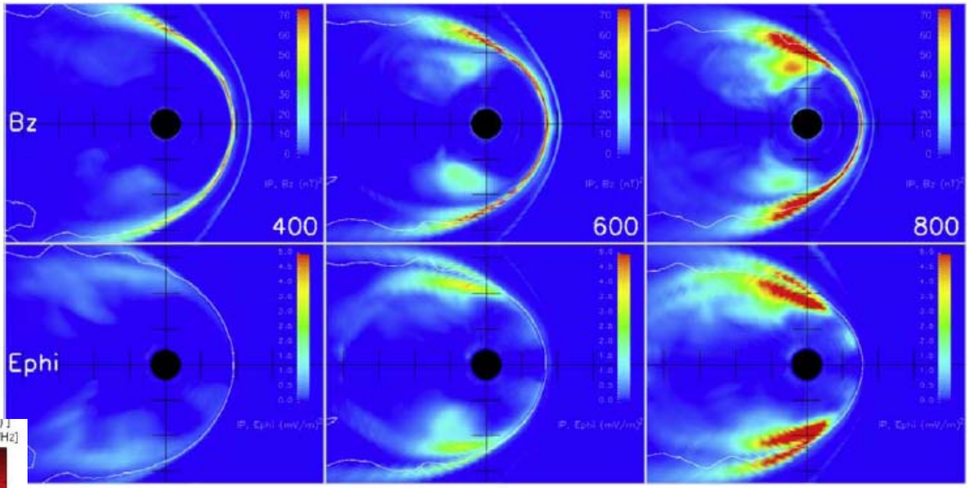

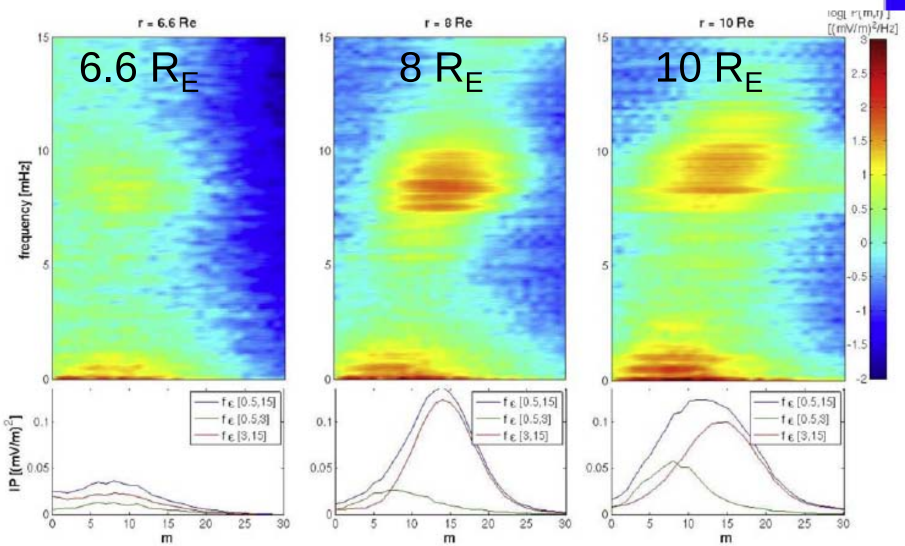

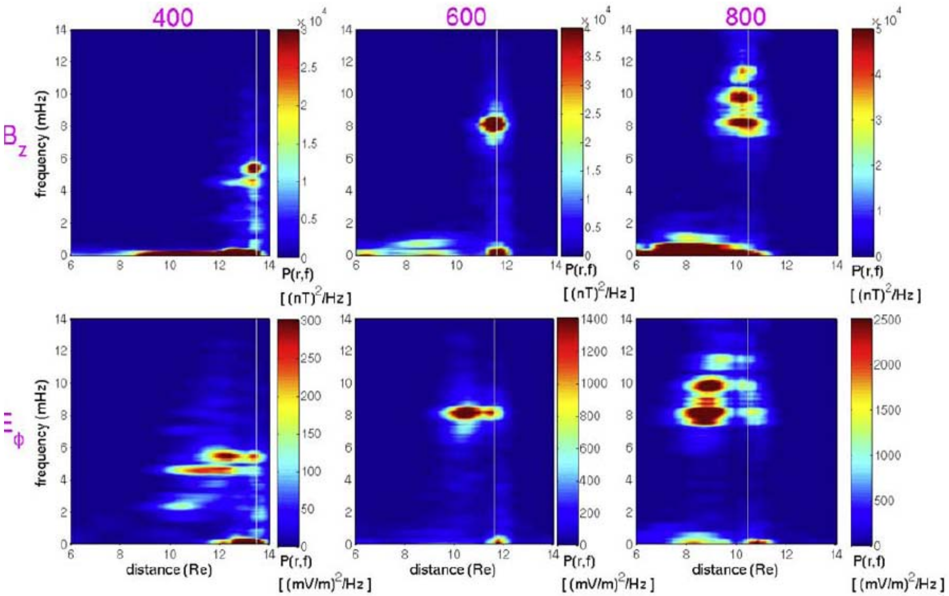

PSD (top) and integrated power vs. m number at Vsw = 800 km/s for 0.5-3 mHz MS (left) and 3-15 mHz KHI (right).

Wave Sources – Boundary Instabilities

Plaschke et al. [GRL 2009] did a statistical analysis of 452 THEMIS observations of magnetopause oscillations over 8 months. These were at discrete frequencies, which may be due to eigenoscillations of MP surface mode-field line-ionosphere system.

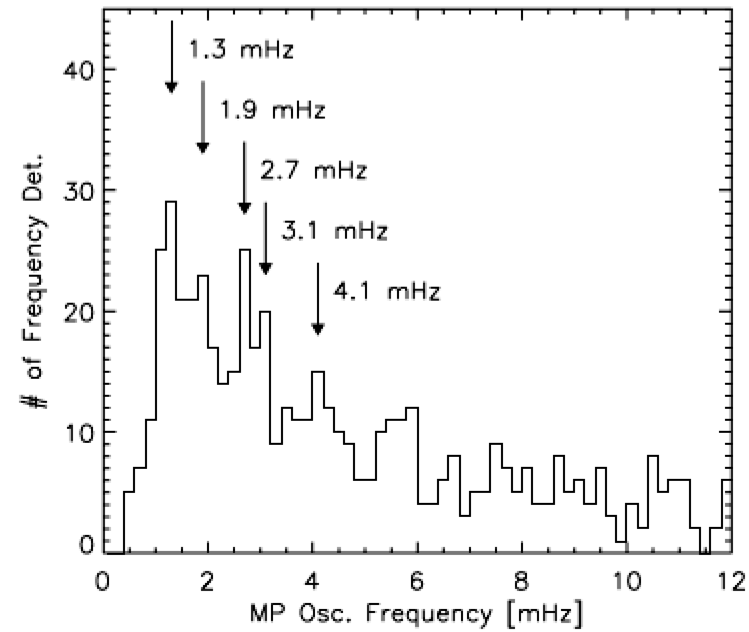

Figure 2. Distribution of oscillation frequencies obtained from the estimation of the MP motion by spline interpolation. Binsize used: 0.2 mHz. Maxima of the distribution are marked with arrows.

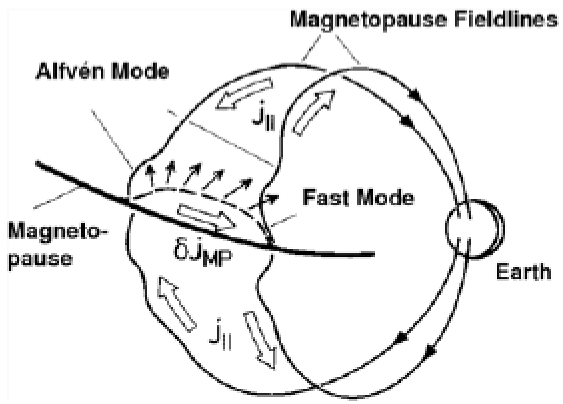

Figure 3. A pressure pulse acting locally on the MP leads to a local disturbance $\delta \mathbf{j}_{CF}$ of the Chapman-Ferraro current system. The additional current is closed via field aligned currents associated with an Alfvén wave propagating along the boundary. Figure modified after *Glassmeier and Heppner* [1992].

Wave Sources – Boundary Instabilities

Pc5 wave power and occurrence in 13 months of THEMIS data [Liu et al., JGR 2009].

Toroidal modes near the flanks (arrowed) suggest KHIs are an important source of Pc5, compared to solar wind pressure variations.

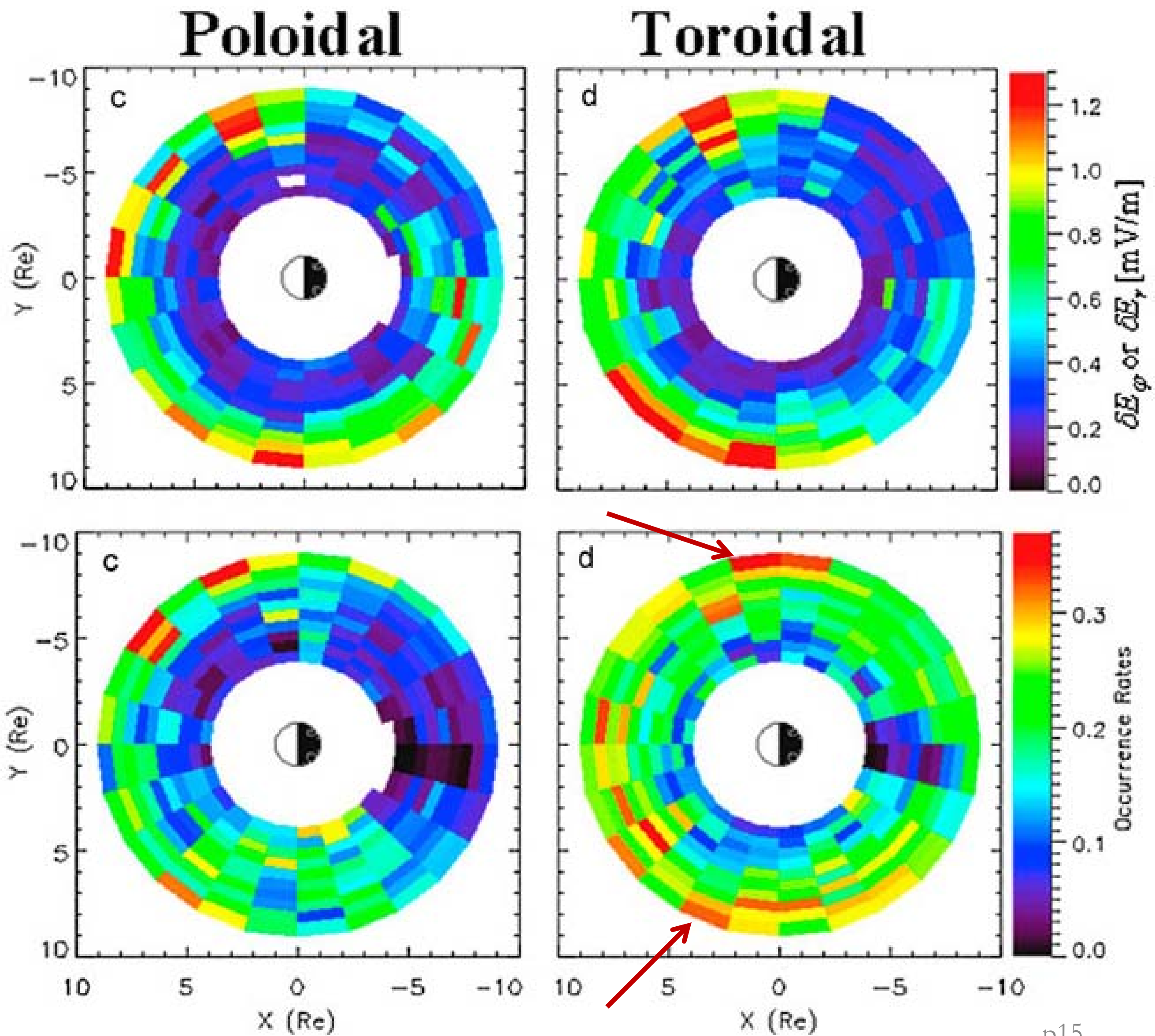

Wave Sources – Boundary Instabilities

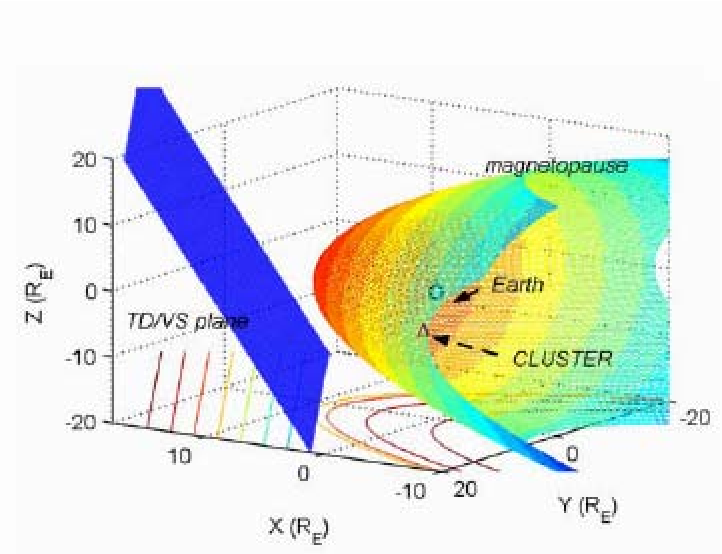

Figure 7. Schematic showing the TD/VS approaching the magnetopause. The position of Cluster is indicated.

Arrival of tangential discontinuity/vortex sheet triggered global 3 mHz oscillations followed by 13 mHz KHI waves [Farrugia et al., JGR 2008]. Non-linear large eddy simulations show the buildup of large KH vortices from the TD/VS. Large changes of the boundary layer due to the KHI occur on time scales comparable to the growth rate after the action of a strong trigger [Farrugia & Gratton, JASTP 2011].

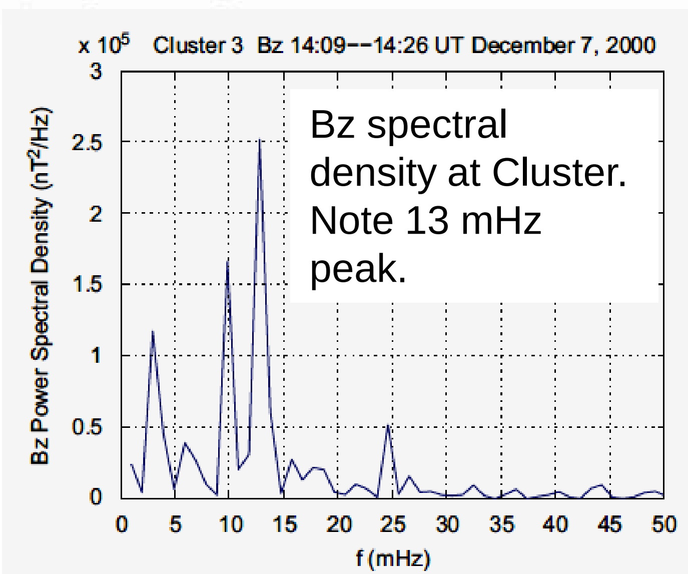

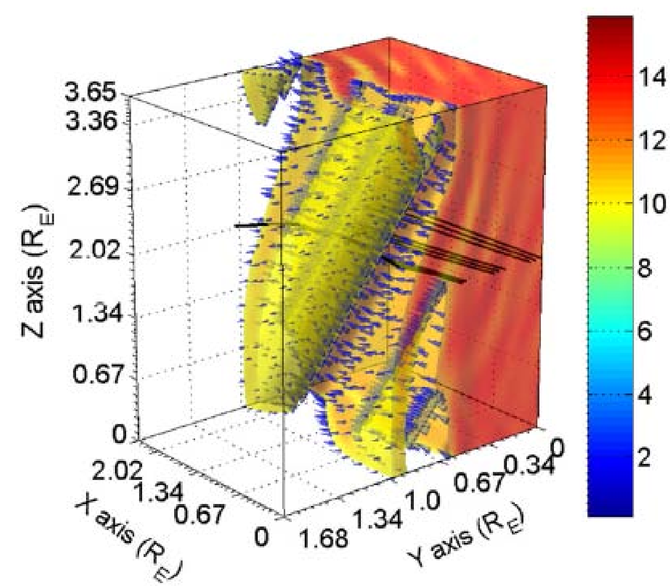

9 p/cm^3 isodensity surface

1.3 Wave Sources – Nightside

Summary

Observations and modelling reveal harmonically-related Pc1 waves in the PSBL [Engebretson et al., JGR 2010; Denton et al., JGR 2010]. Substorm-related current disruption events may simultaneously produce quasi-perp ICWs with $\omega \leq \Omega_i$ (gyrofreq) and quasi-parallel waves with $\omega \sim \Omega_i$ [Yoon et al., JGR 2009; Mok et al., JGR 2010].

Cusp-latitude ground observations suggest that nighttime Pc3-4 waves have an upstream origin, perhaps via the tail lobes [Francia et al., AG 2009; De Lauretis et al., JGR 2010; Ponomarenko et al., GRL 2010].

- How important is the PSBL as a source of ICWs?
- There are a lot of ‘regular’ non-Pi2 low *m* waves on the nightside. Where do they come from?

1.3 Wave Sources – Nightside

Cluster observations in the PSBL show harmonically-related Pc1-2 waves with $f \approx \Omega_{cp}$ [Engebretson et al., JGR 2010].

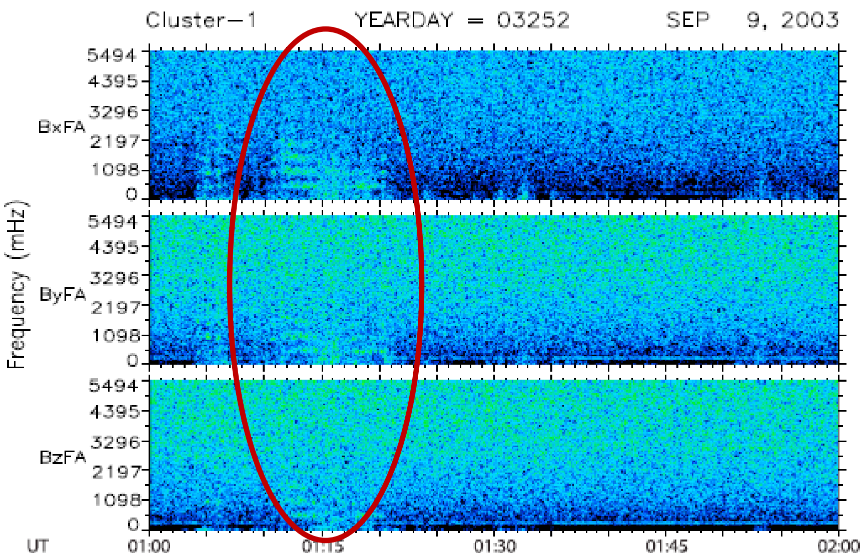

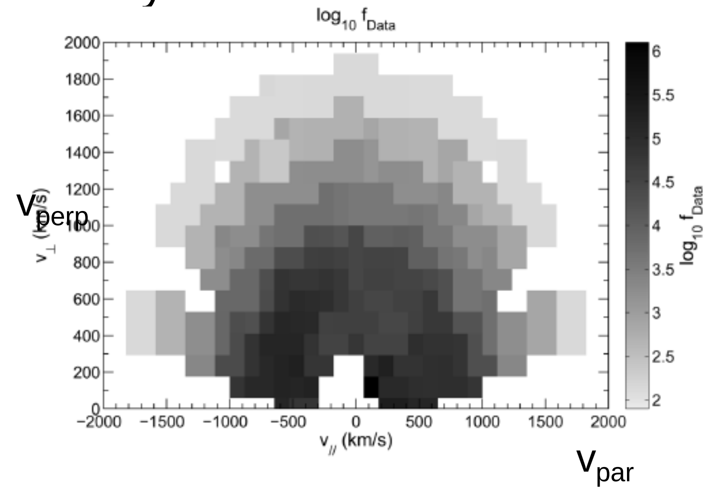

Ring-like feature in IDF leads to instability growth [Denton et al., JGR 2010].

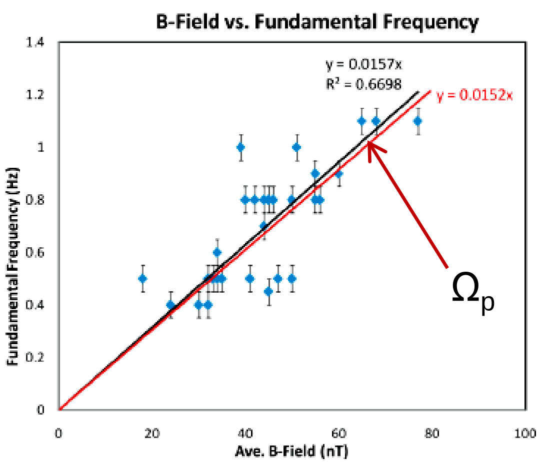

Wave fundamental freq. vs B field

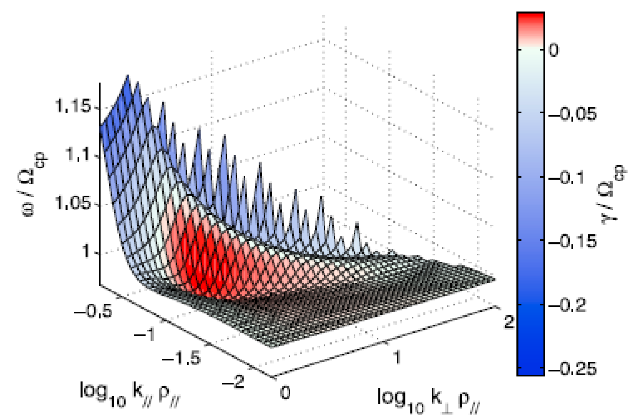

Figure 8. Surface showing the normalized real frequency ω/Ω_{cp} (vertical level) versus $k_\| \rho_\|$ and $k_\perp \rho_\|$ (horizontal scales), with the normalized growth rate γ/Ω_{cp} indicated by the color using the color bar at right.

1.3 Wave Sources – Nightside

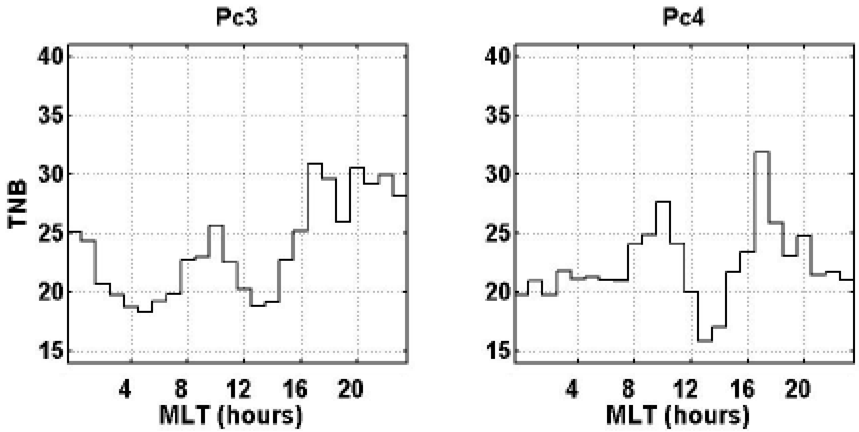

Diurnal % distribution of polarized Pc3, 4 power at a cusp station shows significant nightside activity [Francia et al., AG 2009].

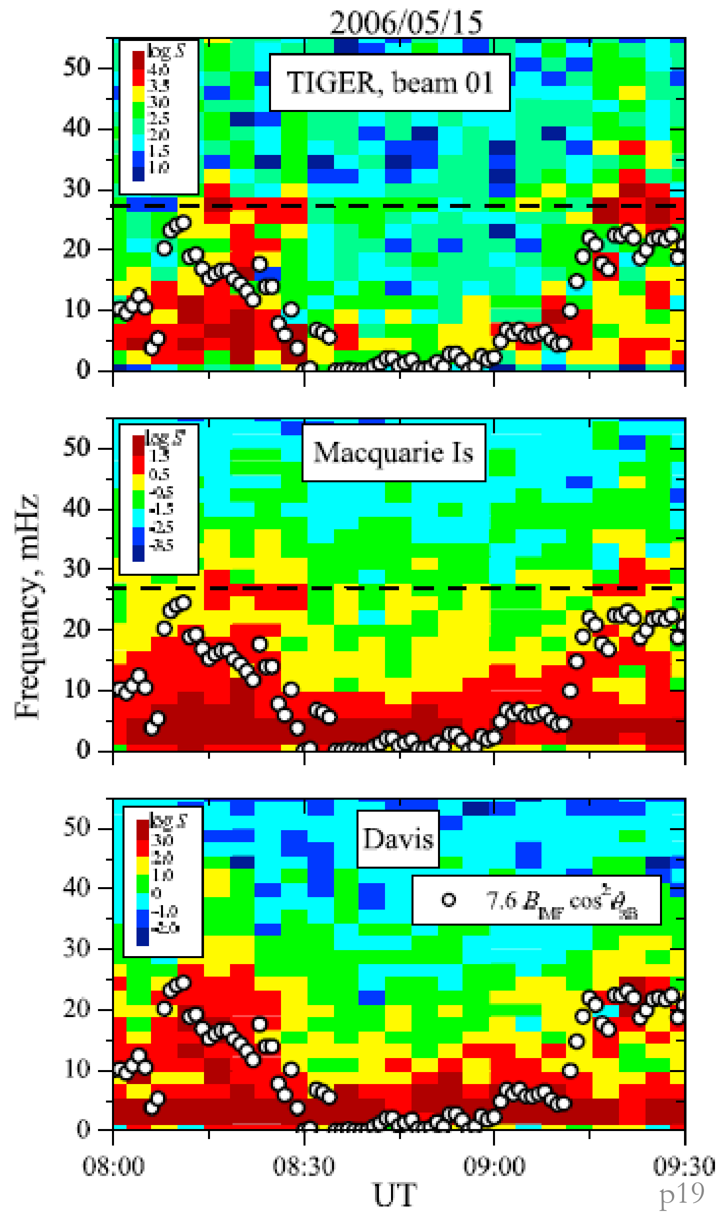

Similarity between dynamic spectra of Pc3 seen on nightside by HF radar (top), at nearby magnetometer (middle), and by dayside cusp magnetometer (bottom) suggests common source in upstream waves (circles) [Ponomarenko et al., GRL 2010].

2.1 Wave Generation & Propagation – Global Modes

Summary

Negative and positive solar wind impulses excite mHz waves [Zhang et al, JGR 2010; Børve et al., AG 2011] at discrete frequencies. Waves at these frequencies may occur throughout the magnetosphere [Liou et al., GRL 2008; Claudepierre et al., GRL 2009; Clausen & Yeoman, AG 2009] and plasmasphere [Ndiitwani & Sutcliffe, AG 2009].

Multipoint observations provide new evidence of plasmasphere eigenmodes (virtual resonances) [Turkaken et al., JGR 2008; Takahashi et al., JGR 2009, 2010]. However, Pc5 power is significantly lower in the plasmasphere than the trough [Hartinger et al., GRL 2010].

- Are global modes restricted to extreme conditions?
- How common are plasmaspheric resonances?

Wave Generation & Propagation – Global Modes

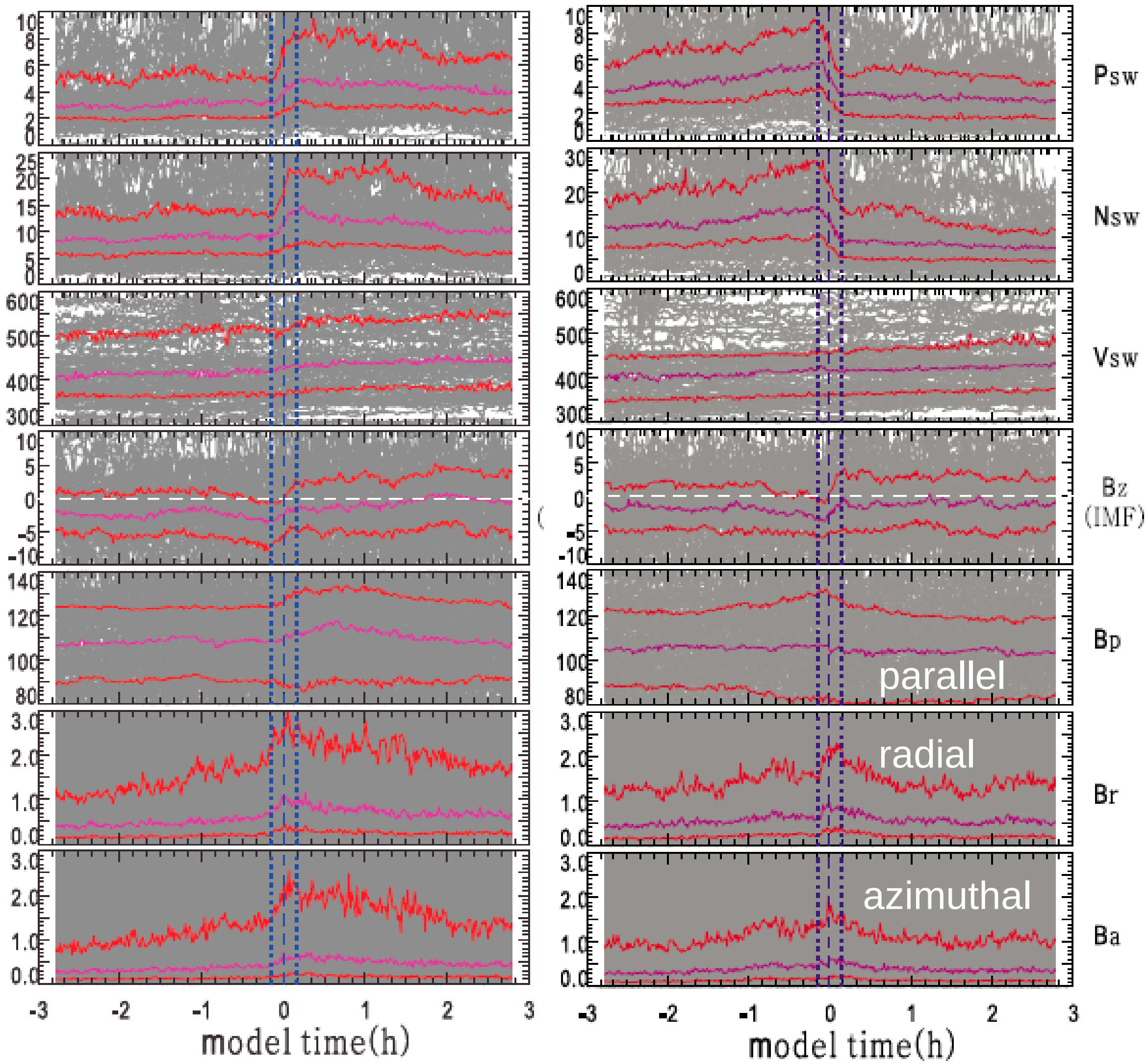

Solar wind, IMF and GEO magfield parameters for southward IMF events (purple = median)

Superposed epoch analysis of Pc5-range ULF events at GEO for 270 positive (left) and 254 negative (right) solar wind pressure pulses [Zhang et al., JGR 2010].

Both types of impulses excite poloidal and toroidal waves, but these are weaker for negative events. The oscillations are stronger near noon than dawn and dusk.

Wave Generation & Propagation – Global Modes

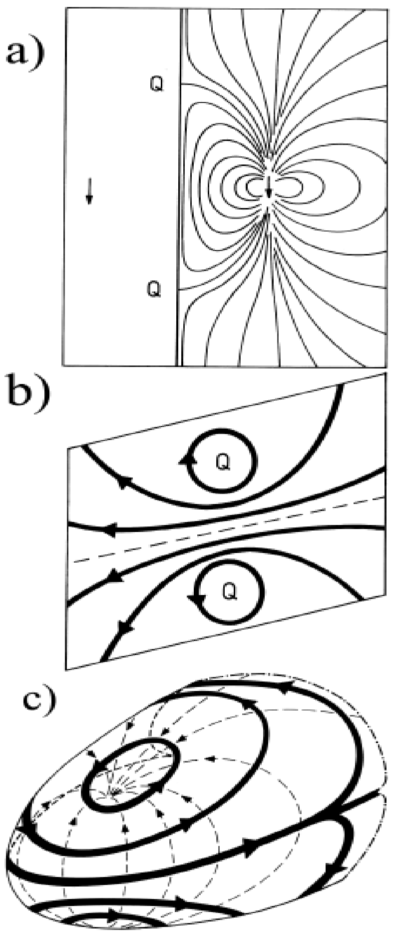

A conceptually simple model of the solar wind-magnetosphere interaction (left) allows characterisation of magnetopause oscillations due to solar wind density changes [Børve et al., AG 2011].

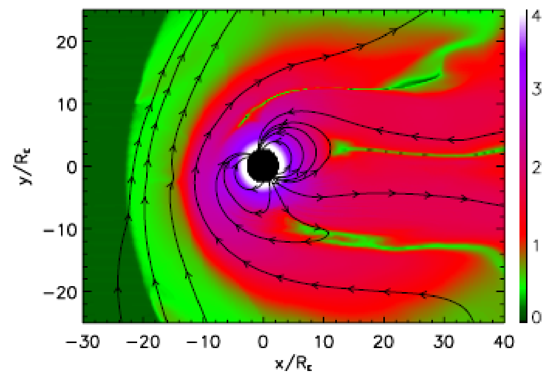

Fig. 11. Magnetic field variations, corresponding to Fig. 6. The present case has a tilt of $\pi/6$ for the magnetic dipole axis.

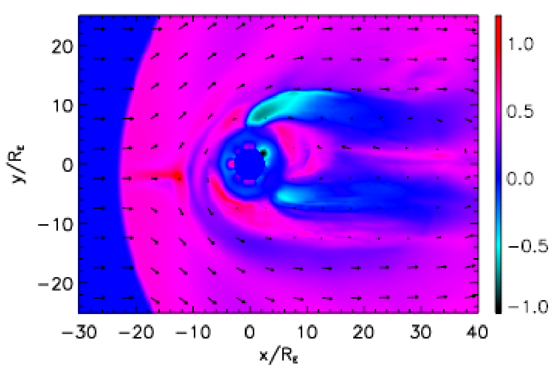

Magnetic field and density for the tilted dipole model.

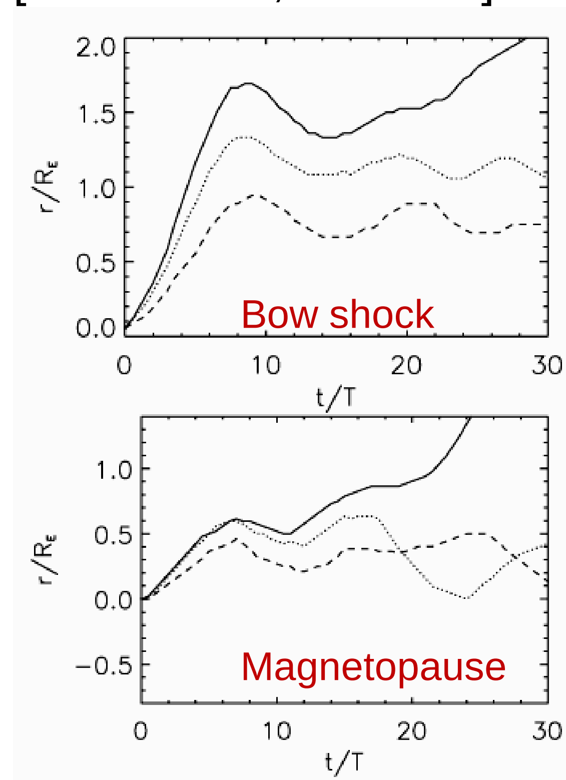

Resultant oscillations for 10%, 15% and 20% changes in solar wind density.

Wave Generation & Propagation – Global Modes

Occurrence of ‘magic’ frequencies in Cluster magnetic field data (132 orbits), using different magnetic field models. Lower 3 panels relate to different averaging lengths.

Frequencies are not consistent across all components, maybe because the spacecraft is inside the FLR turning point [Clausen and Yeoman, AG 2009].

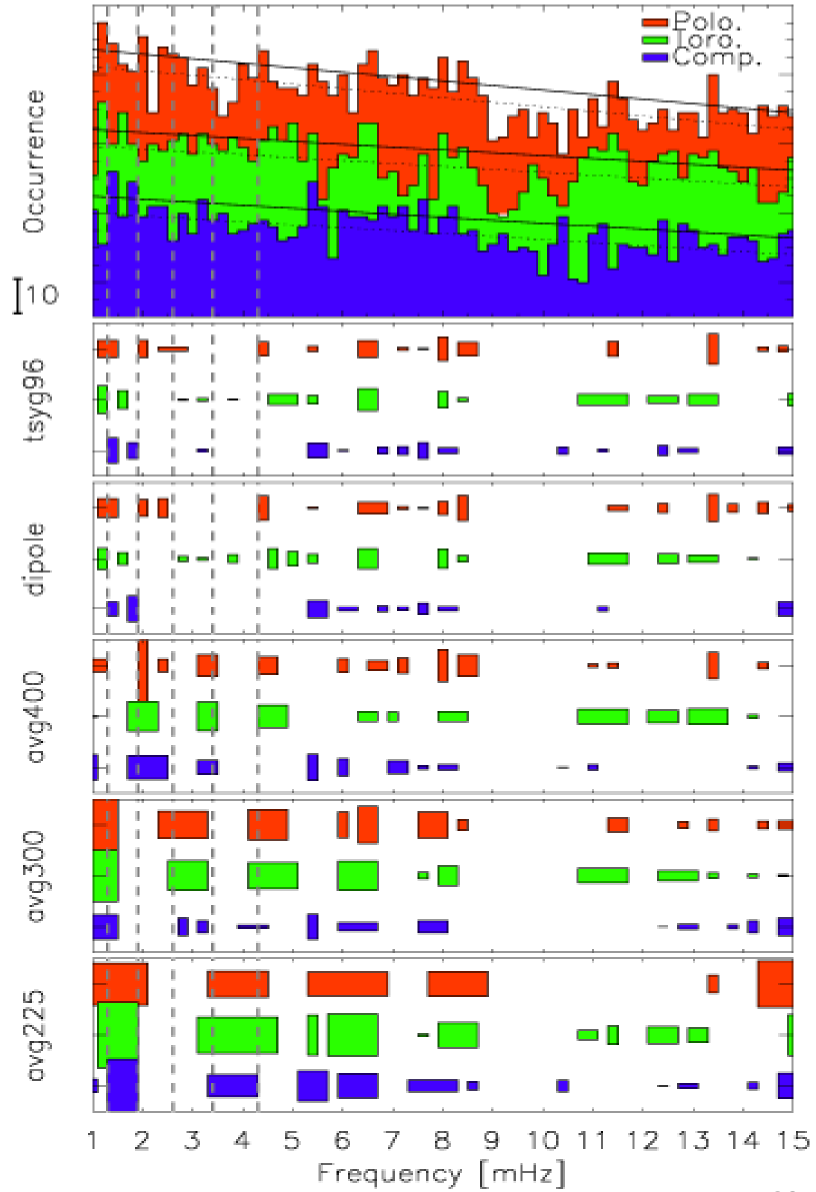

Wave Generation & Propagation – Global Modes

Evidence of plasmaspheric cavity modes: expected (below) and observed (right) radial variation of V_A, amplitude and phase of poloidal components [Takahashi et al., JGR 2010].

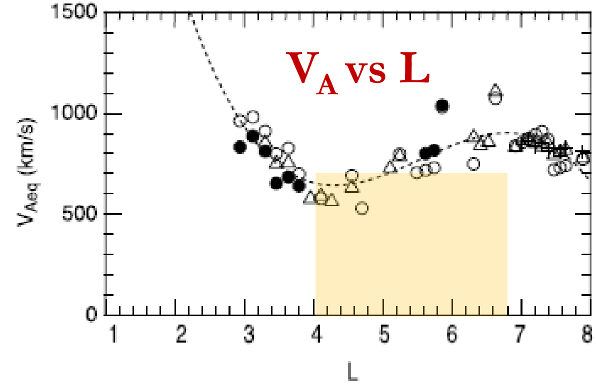

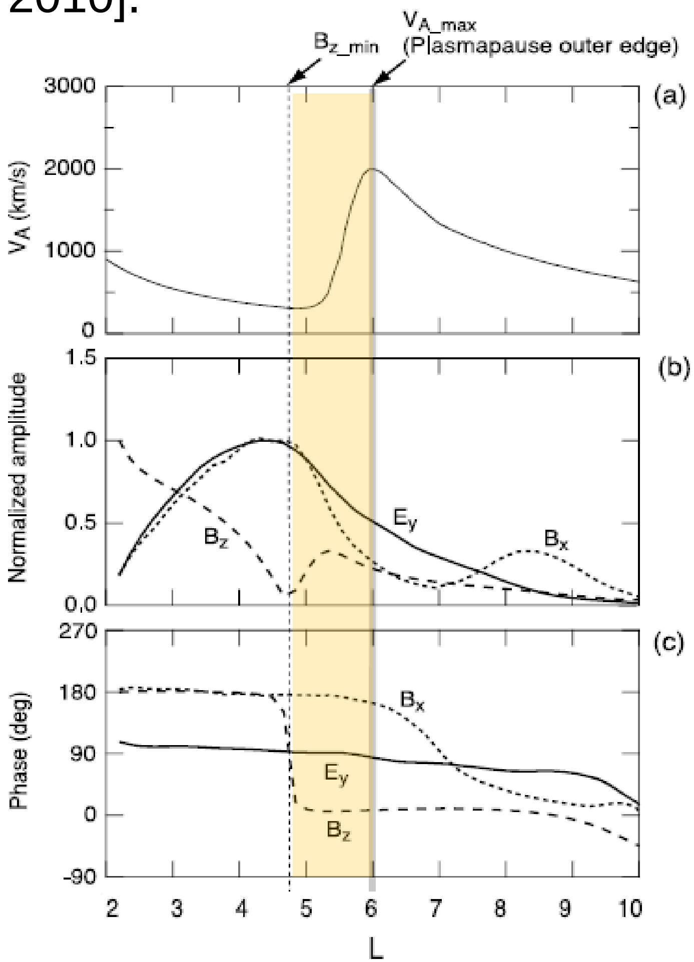

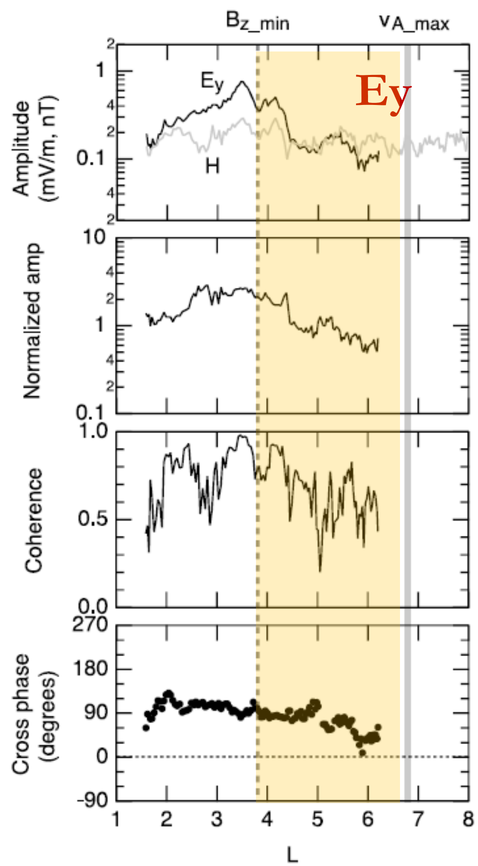

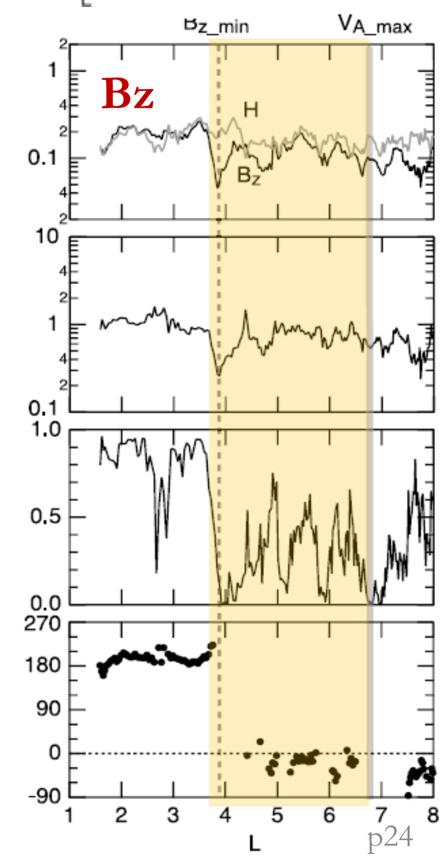

2.2 Wave Generation & Propagation – FLRs

Summary

Ground-satellite observations confirm that upstream broadband waves propagate through the magnetosphere to stimulate FLRs at high latitudes [Clausen et al., AG 2009] and at low latitudes [Ndiitwani and Sutcliffe, AG 2010]. THEMIS survey data show Pc4 are dominant ~5 – 6 R_E and Pc5 ~7 – 9 R_E, suggesting FLRs are an important component of Pc4 activity [Liu et al., JGR 2009].

Combined in situ and ground measurements show that Pc3 waves just inside the cusp have transverse scale size of ~0.14 R_E and are shear mode Alfven waves guided along closed field lines to the ground with high coherency and 90^o ionospheric rotation [Liu et al., JGR 2008, 2009]. The waves occurred globally across the ground.

Simulations show that a continuous spectrum of FLRs results from broadband pressure fluctuations [Claudepierre et al., JGR 2010].

Wave Generation & Propagation – FLRs

Summary (cont.)

Improved theoretical treatments of FLRs include effects of azimuthal plasma motion in the magnetosphere [Kozlov and Leonovich, JGR 2008], and non-axisymmetric magnetic field topologies that modify wave polarization properties [Kabin et al., AG 2007].

A compressed dipole treatment incorporating day/night asymmetry [Degeling et al., JGR 2010] shows that spatial properties of FLRs are determined by the accessibility of MHD fast mode waves to different locations of the magnetosphere. This is demonstrated observationally by Degeling et al and Sarris et al. [JGR 2009; GRL 2009].

- How does such a more realistic consideration of FLR source location affect ideas on radiation belt electron transport?

Wave Generation & Propagation – FLRs

Comparison of Pc3 on the ground at L=1.8 and wave properties seen by CHAMP as it passed nearby [Ndiitwani & Sutcliffe, AG 2010]. Note *L*-dependent toroidal mode frequency.

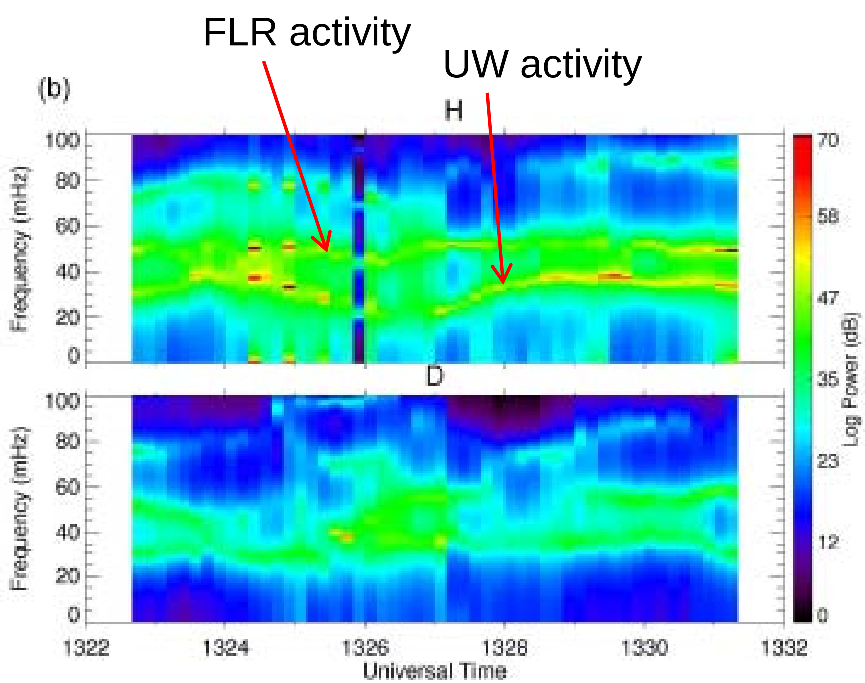

Ground magnetometer

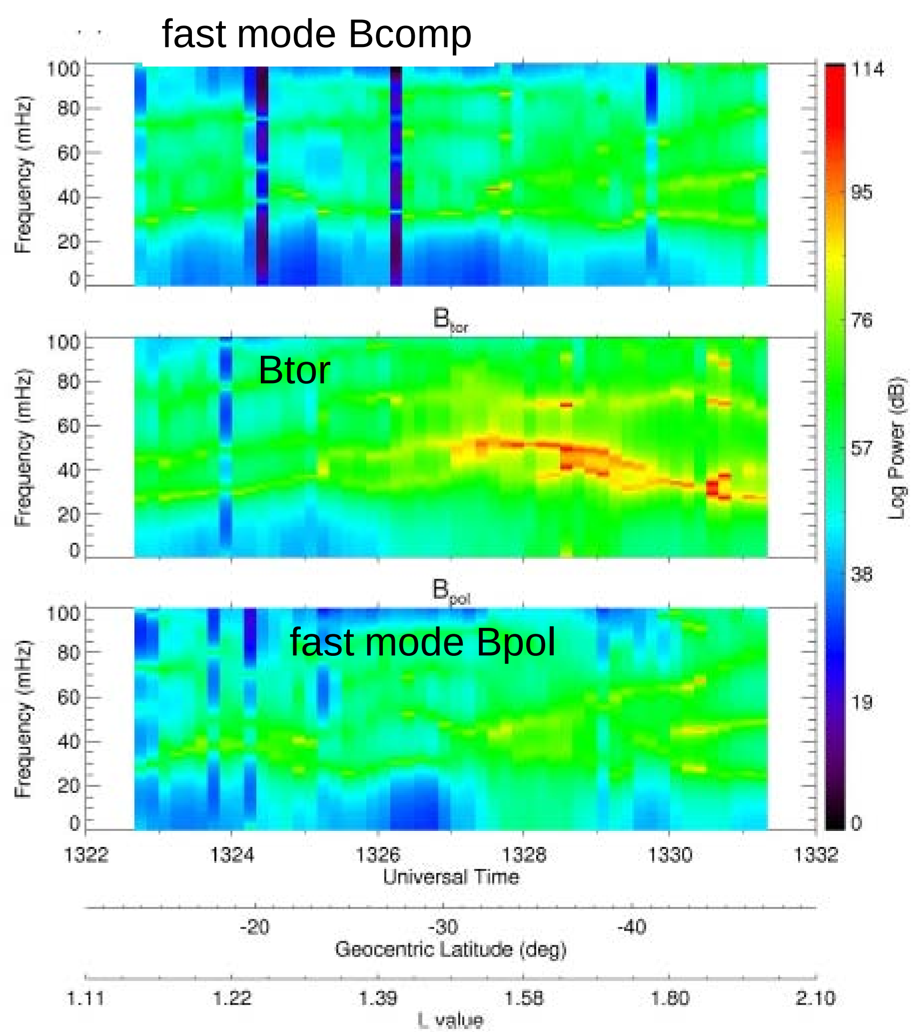

CHAMP spacecraft

Wave Generation & Propagation – FLRs

Satellite-ground coherency analysis of Pc3 waves propagating on the last closed field lines from the exterior cusp to the ground confirms 90º rotation and gives a transverse scale size ~0.14 R_E [Liu et al., JGR 2009].

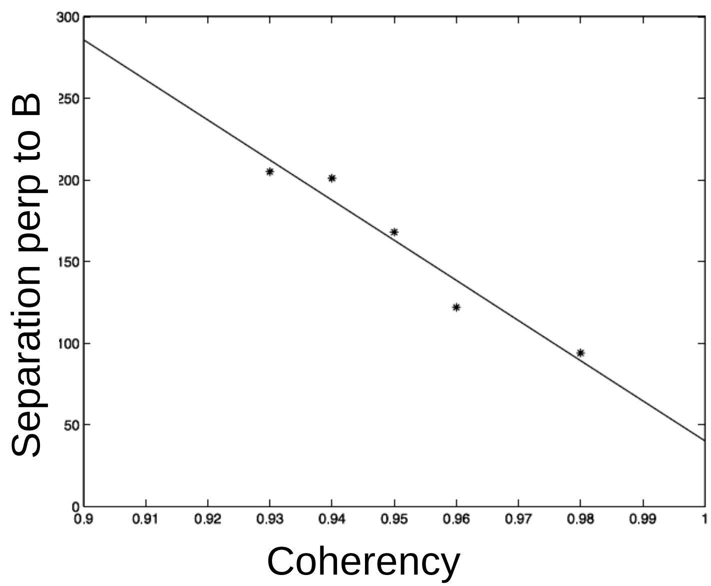

Correlation of coherency with spatial separation.

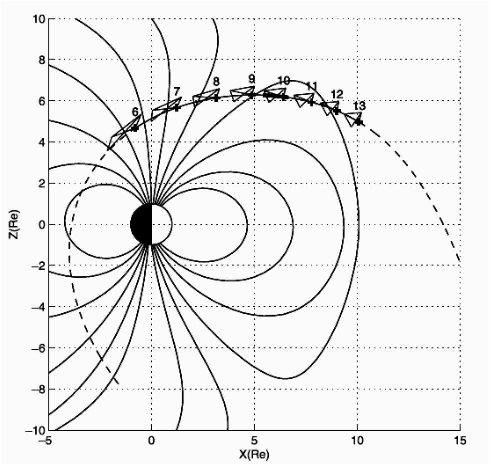

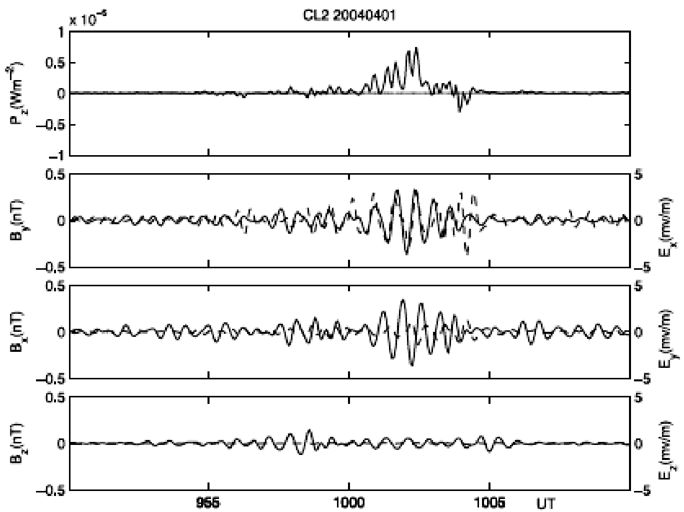

Poynting vector z cpt, wave E (dashed) and B fields (solid line). Other cpts were x and y [Liu et al., JGR 2008]

Wave Generation & Propagation – FLRs

Global 3D MHD simulation of FLR power excited by monochromatic 10 mHz solar wind pressure variations [Claudepierre et al., JGR 2010]. The simulations also show that a continuum of fluctuations drives a spectrum of toroidal mode FLRs.

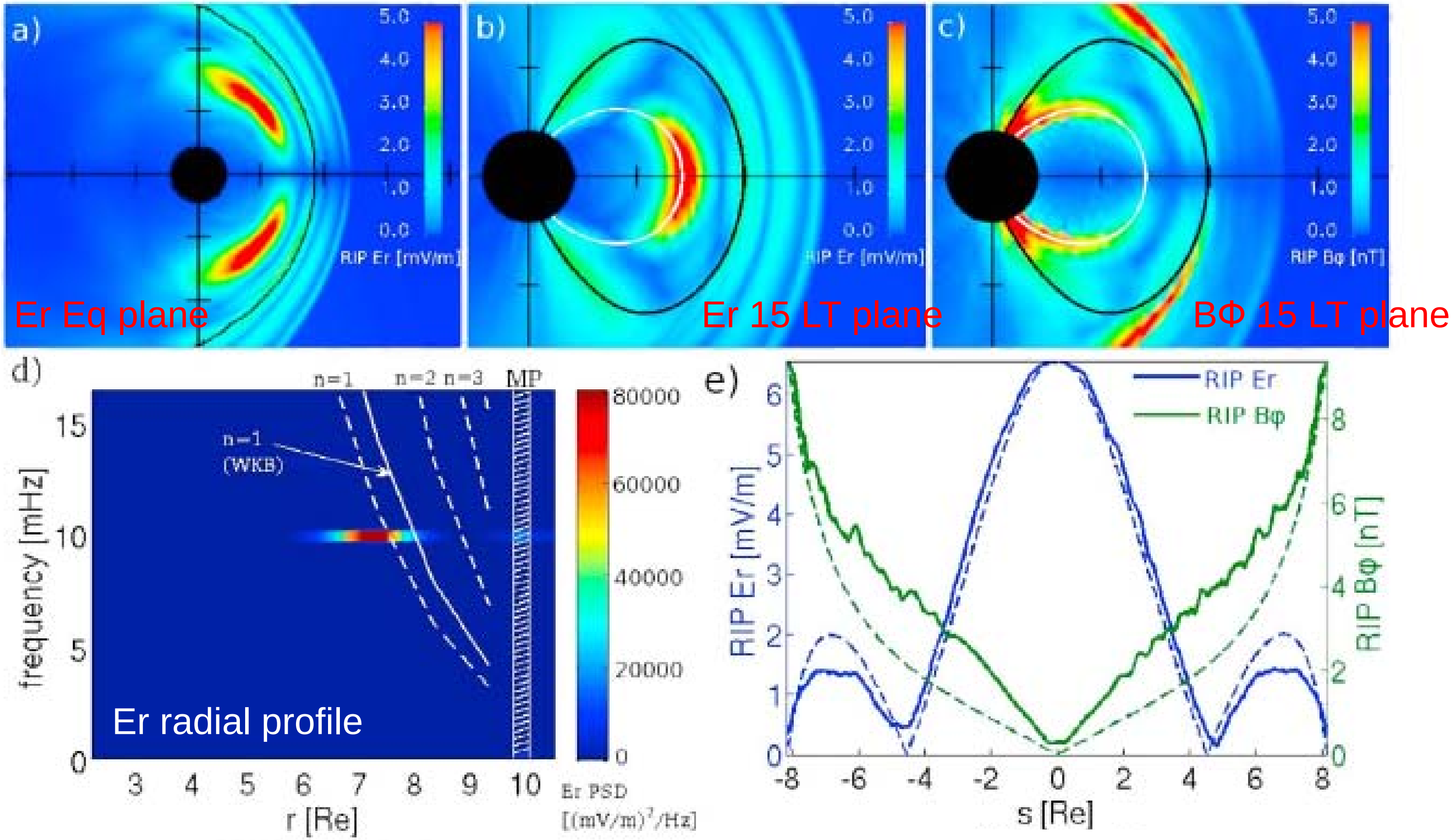

Field line E & B field mode structure

Wave Generation & Propagation – FLRs

Right and below: Compressed dipole geometry distorts period and polarization of standing shear Alfven waves with MLT [Kabin et al., AG 2007].

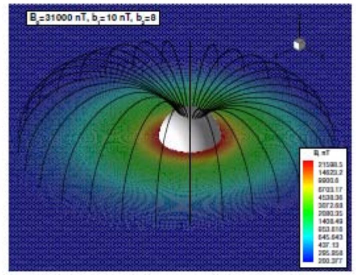

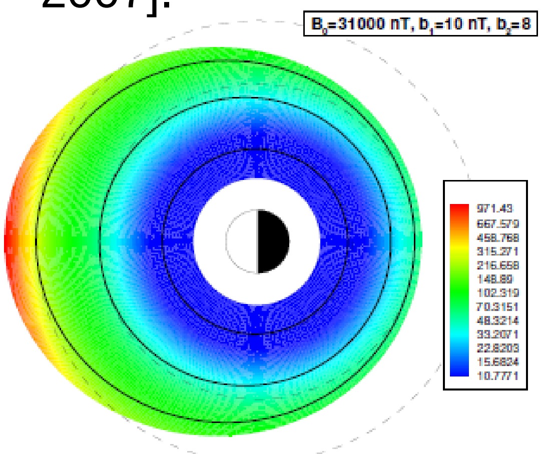

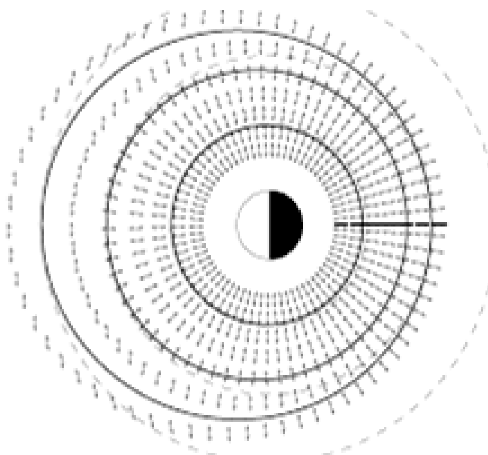

RADIAL *E* ("TOROIDAL") at MIDNIGHT

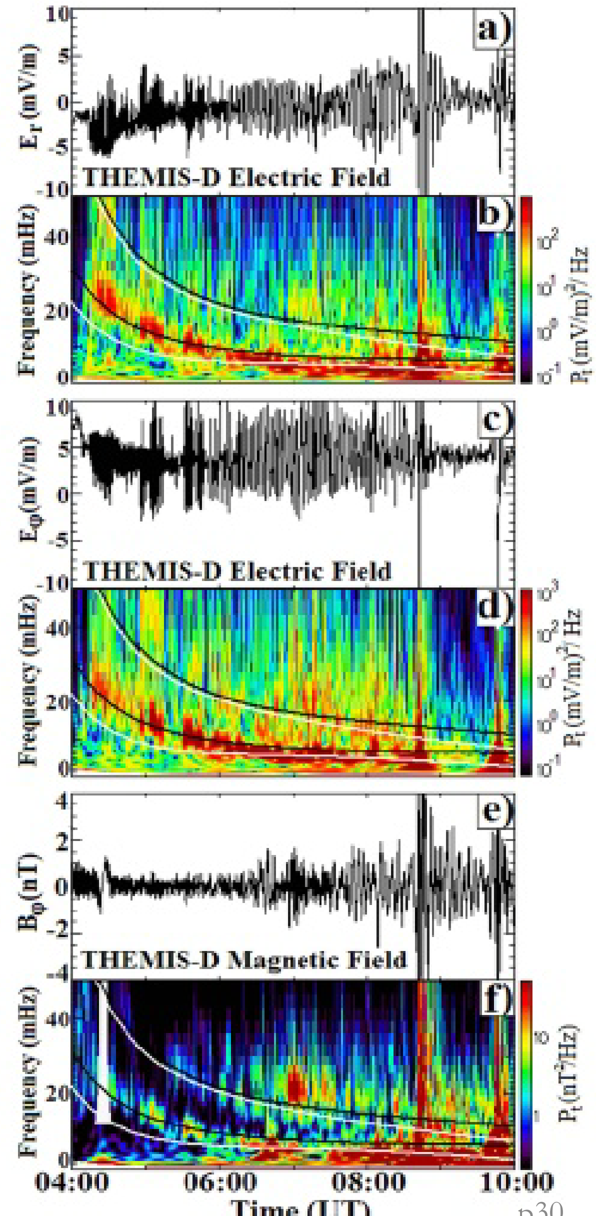

Right: ULF waves seen by THEMIS from ~4-10R_E. Lines show Rankin et al./Kabin et al. model mode 1 ("poloidal" – white) and mode 2 ("toroidal" – black) frequencies [Sarris et al., GRL 2009].

Wave Generation & Propagation – FLRs

FLR E_α ("toroidal" mode) and E_β ("fast" mode) amplitude and phase (columns) given a 5 mHz driver at 12, 15, 18 and 21 MLT (rows)[Degeling et al., JGR 2010]. This suggests that penetration of energy from a source at the magnetopause to lower *L* shells requires the source to be close to local noon – i.e. not a KHI.

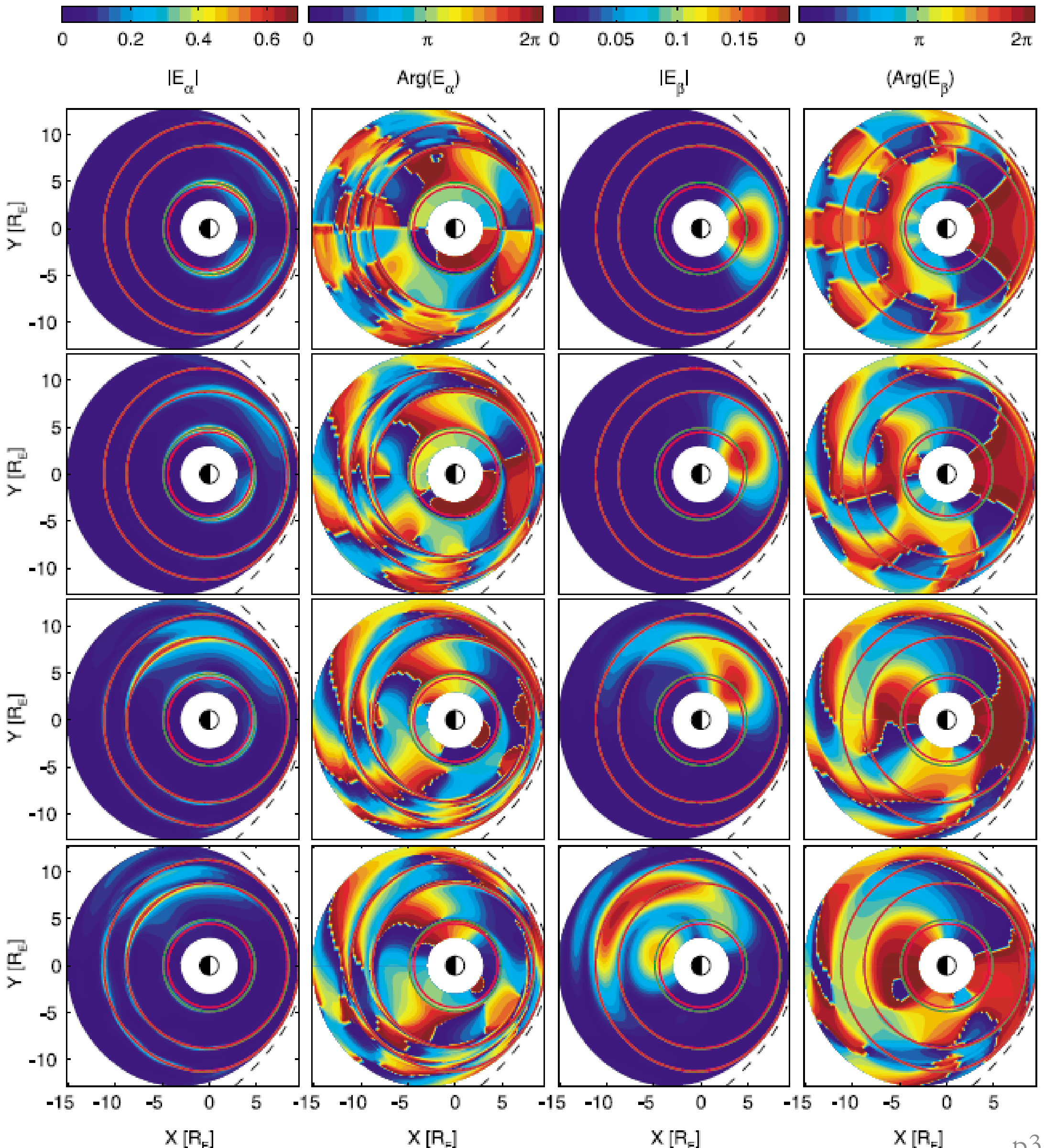

2.3 Wave Generation & Propagation – Poloidal Modes

Summary

Multipoint spacecraft observations are providing new information on poloidal modes. During recovery phase these waves may persist in the outer magnetosphere for days and exhibit polarization rotation to toroidal waves [Sarris et al., JGR 2009a, b]. They also may occur at the plasmapause [Schäfer et al., AG 2008].

Poloidal Alfven modes are sensitive to finite plasma pressure and field curvature. These affect the field-aligned wave structure, resulting in an opaque region forming near the equatorial plane where partial reflection of the waves occurs [Mager et al., AG 2009].

- How do these results affect models of particle energization by poloidal modes?

Wave Generation & Propagation – Poloidal Modes

5-day GOES-8 observations of a Pc5 event in storm recovery phase [Sarris et al., JGR, 2009a]. The wave was radially localized and ground data showed azimuthal wavenumber *m*~20-60.

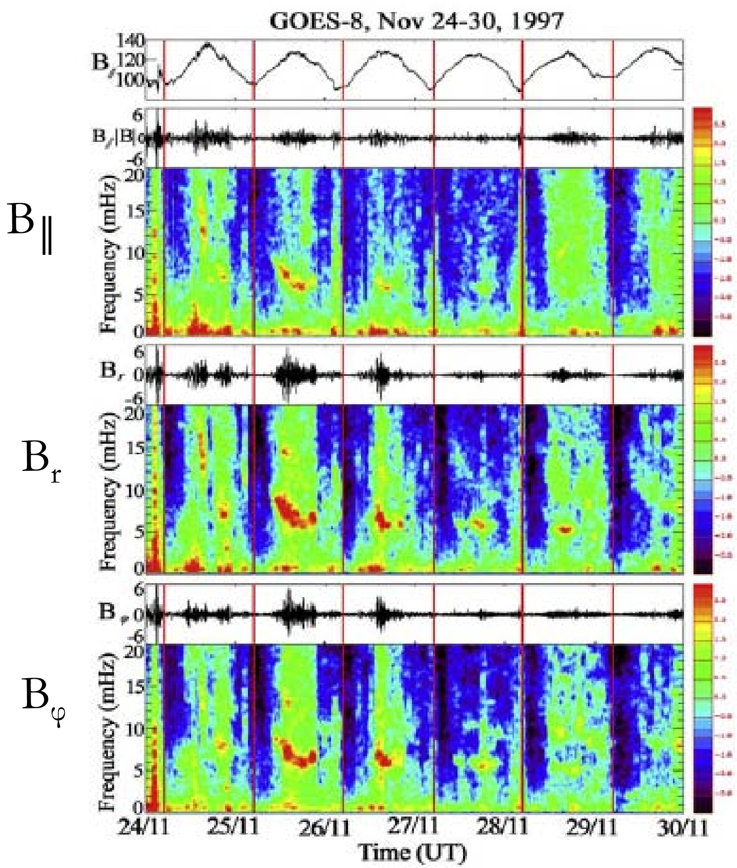

Change in polarization from poloidal to toroidal [Sarris et al., JGR, 2009b].

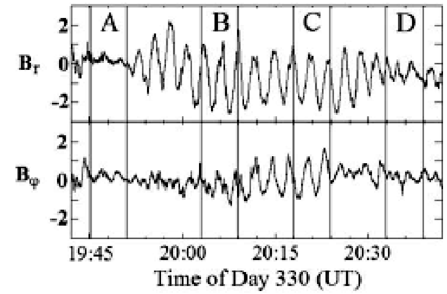

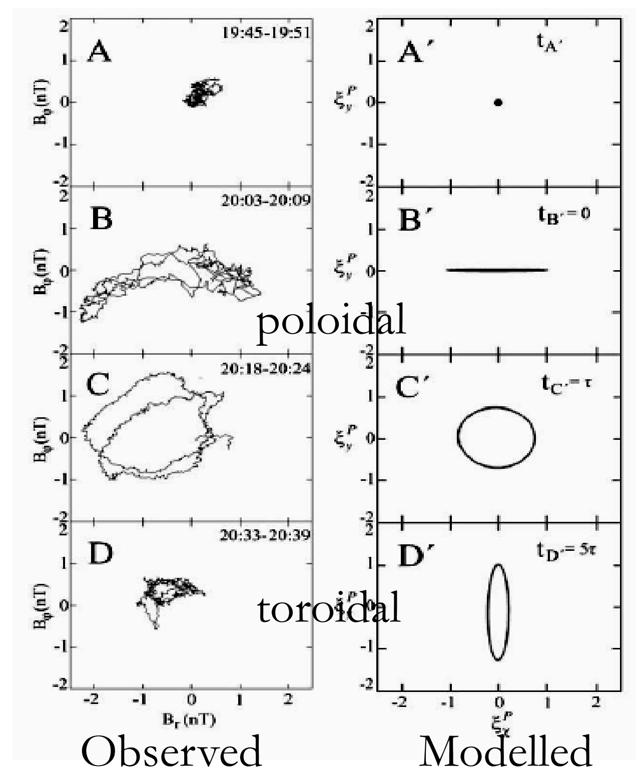

Wave Generation & Propagation – Poloidal Modes

Cluster measurement of 2nd harmonic standing poloidal mode wave with *m*=155 just outside the plasmapause [Schäfer et al., AG 2008]. The two wavepackets show evidence of evolution from purely toroidal to mixed toroidal and poloidal modes.

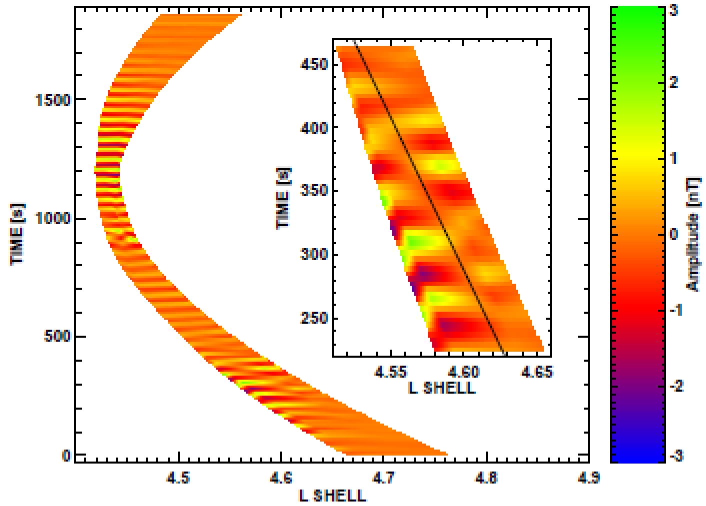

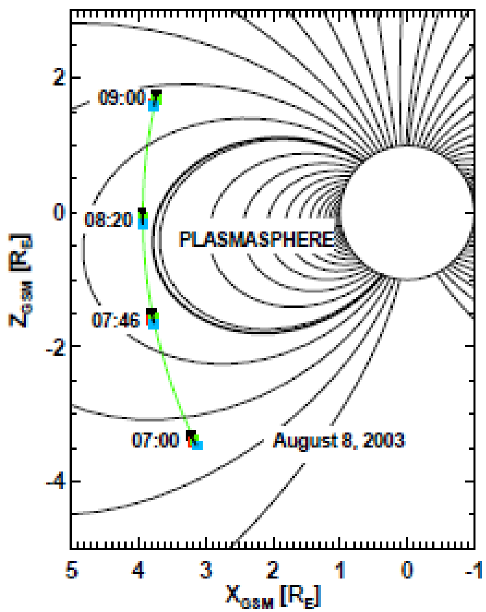

Fig. 1. The Cluster orbits in the dayside magnetosphere on 8 August 2003, 07:00 and 09:00 UT. The ULF pulsation investigated is detected between 07:46 and 08:20 UT. The thick black line marks the plasmapause at L=4.23 R_E.

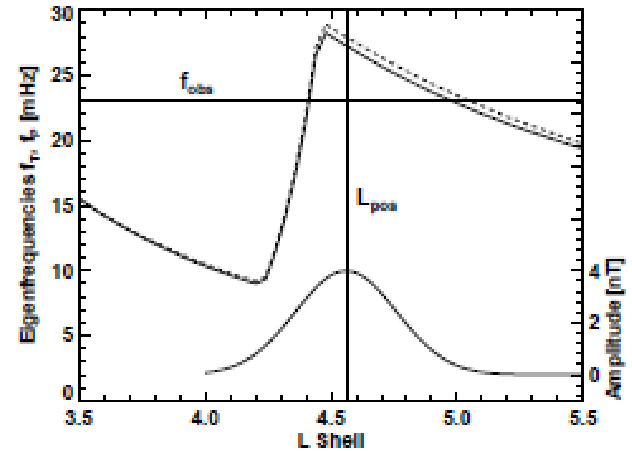

Wave amplitude and toroidal (solid line) and poloidal (dashed) mode eigenfrequencies. Vertical line denotes L shell of max amplitude and phase jump.

Wave Generation & Propagation – Poloidal Modes

Formation of opaque regions for poloidal modes in a finite pressure plasma and dipole field may cause hemispheric decoupling of field lines [Mager et al., AG 2009].

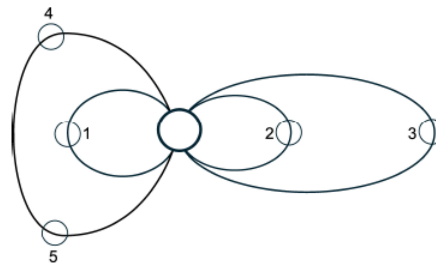

Fig. 2. Cartoon showing possible locations of opaque regions f poloidal Alfvén waves in the magnetosphere.

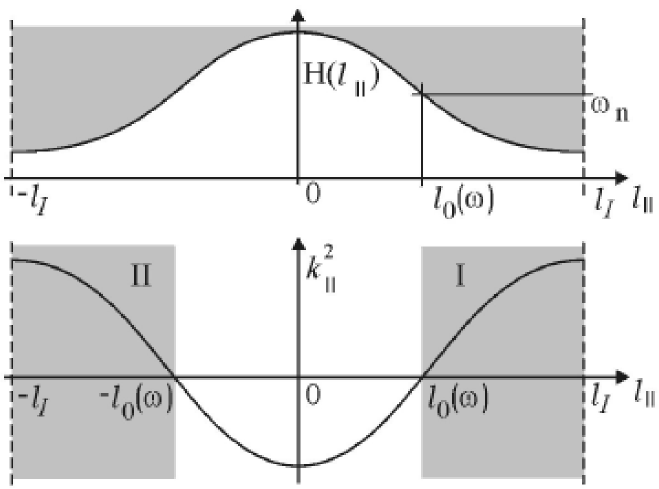

Fig. 1. Sketch demonstrating the dependence of H (top) and $k_{\parallel}^2$ (bottom) on $l_{\parallel}$ and showing probable locations of the transparent and opaque regions. Here $\pm l_0$ are the turning points for a harmonic with eigenfrequency ω_n, $\pm l_I$ are the intersection points of a field line with the ionosphere. The shaded areas I and II correspond to the transparent regions.

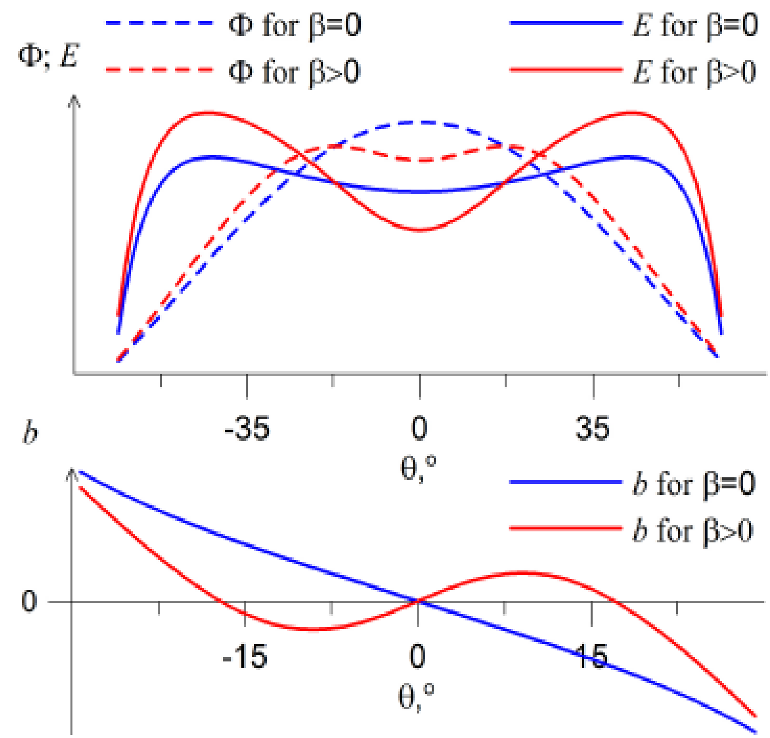

Fig. 7. The field-aligned structure of the fundamental harmonic at $L=6$ shell in plasma with $\beta=0$ and $\beta>0$. Here Φ is the "potential", E and b are the wave electric and magnetic fields, accordingly, and θ is the geomagnetic latitude.

2.4 Wave Generation & Propagation – Other Modes

Summary

Narrow-band Pc3,4 waves occur on open field lines but are not just a poleward extension of mid-latitude activity [Pilipenko et al., JASTP 2008]. The pulsations may be due to the interaction of propagating magnetosonic and Alfven waves such that when the phases match energy is converted into the Alfven wave [Pilipenko et al., JGR 2008].

Cluster and ground observations for large *L* show coherent, low *m*, low frequency waves that propagate sunward [Santarelli et al., AG 2007; Eriksson et al., AG 2008]. THEMIS has found many compressional Pc5 waves which propagate sunward and outward and are likely caused by the drift mirror instability [Constantinescu et al., JGR 2009].

- Is the source of the sunward propagating waves in the tail?
- How common are such features?

Wave Generation & Propagation – Other Modes

Locations and phase velocities of compressional Pc5 was recorded at THEMIS [Constantinescu et al., JGR 2009]. Velocities are ~30 km/s and the waves occur beyond 8 R_E.

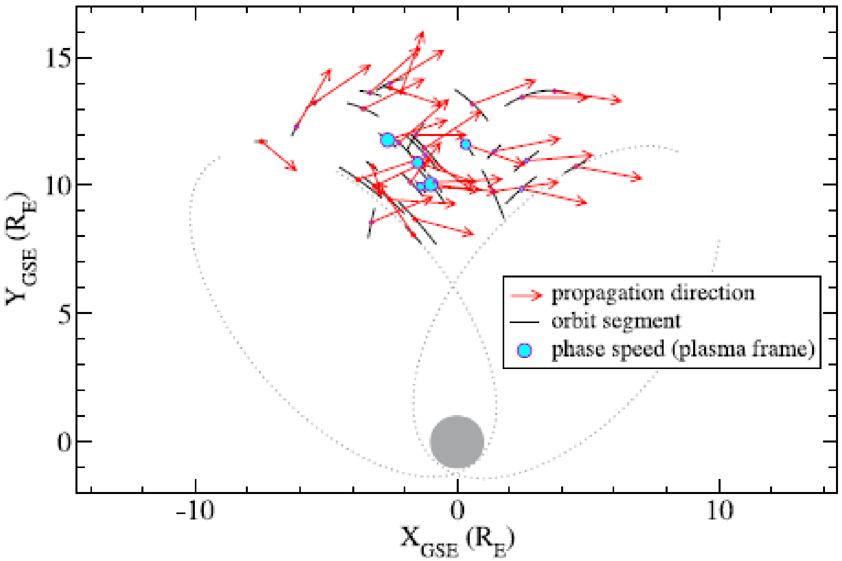

Cluster observations of 1-2 mHz *m*=3 toroidal waves at *L*=16 post midnight [Eriksson et al., AG 2008]. Propagation and Poynting flux are sunward and frequency changes with B.

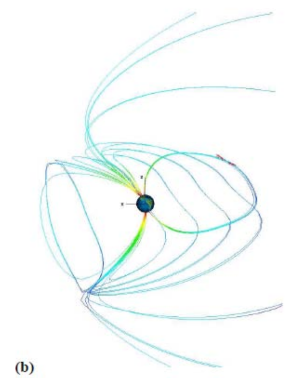

Left: xz orbit projection. Bottom left: power spectrum; bottom right: Poynting flux.

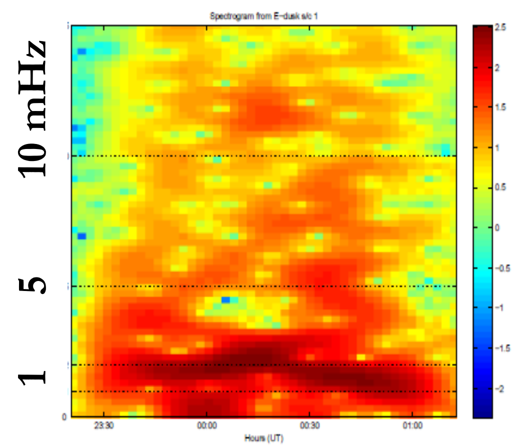

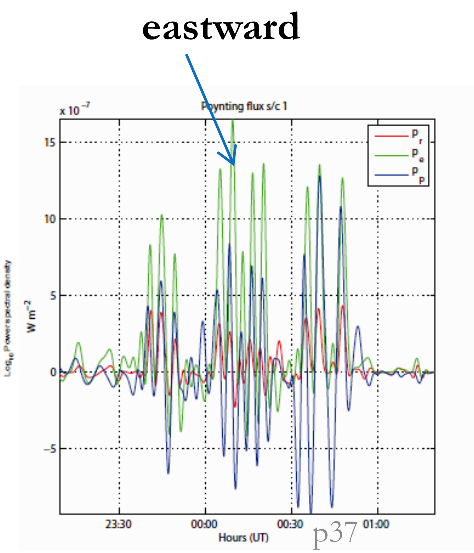

2.5 Wave Generation & Propagation – Pi2

Summary

Ground-based statistical studies have characterized the spatial distribution and evolution of Pi1 and Pi2 power and polarization with respect to substorm onset times and locations [Murphy et al., JGR 2011; Rae, JGR 2011]. There is little difference between wave behaviour across the Pi1 and Pi2 bands, and the wave spectrum near the auroral onset is a power law of slope -3.7.

Multipoint observations now provide precise information on the timing of periodic ion injections, Pi2 in space and on the ground, and modulated auroral luminosity. While Pi2 waveforms and BBFs seem related, a timing case study suggests the BBFs do not directly drive the Pi2 [Murphy et al., AG 2011].

The timing of Pi2 across high and low latitudes shows MLT dependent travel times to high compared to low latitudes for the H (but not D) component [Uozumi et al., JGR 2009].

2.5 Wave Generation & Propagation – Pi2

Summary (cont.)

Evidence that low latitude Pi2 are due to plasmaspheric cavity modes grows. It includes: THEMIS observations of radial standing fast mode Pi2 waves on the dawn and night (but not day) sides [Kim et al., JGR 2010]; observations of night (but not daytime) Pi2 with cavity mode properties in the ionosphere and on the ground [Sutcliffe & Lühr, JGR 2010]; statistical results that Pi2 period is negatively correlated with ∑Kp and positively correlated with mass density [Nosé, JGR 2010]; and comparisons of wave fields and phases in the ionosphere and on the ground [Ikeda et al., JGR 2010].

- The origin of low latitude Pi2 on the night side seems clear. How about on the dayside?

Wave Generation & Propagation – Pi2

Schematic Pi2 model by Keiling et al. [GRL 2008] and Murphy et al. [AG 2011].

(g)

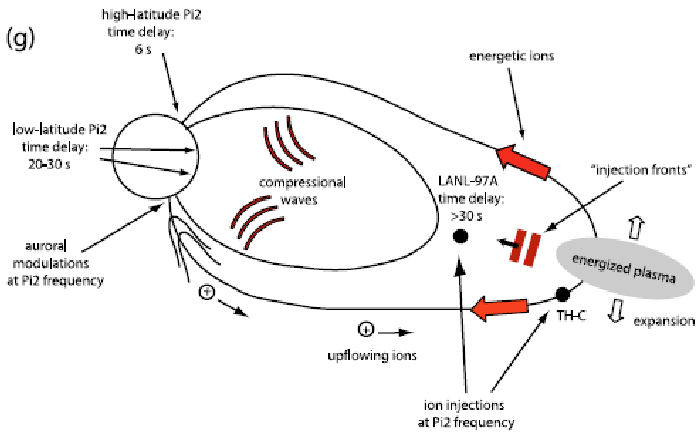

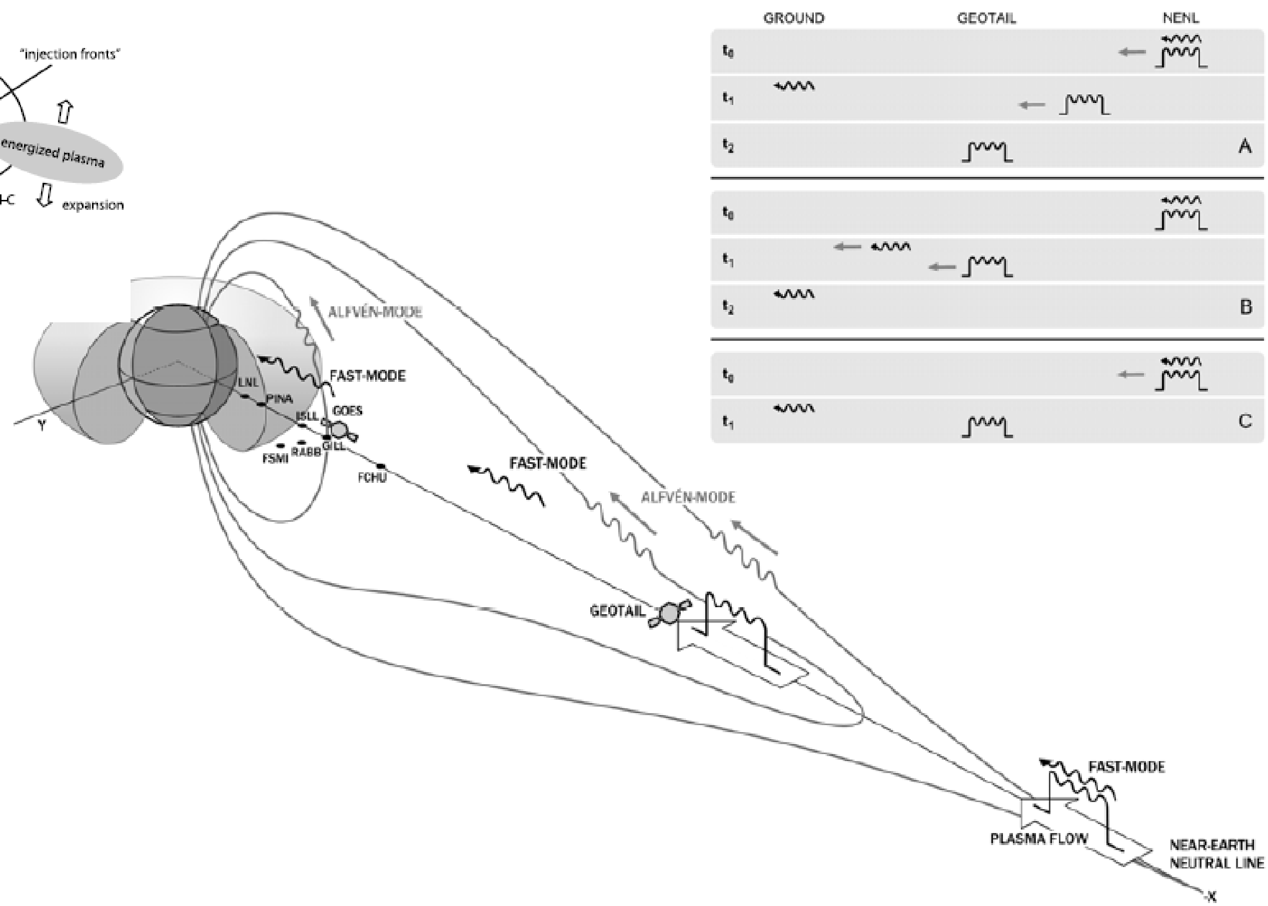

Fig. 8. An illustration depicting a potential sequence of events subsequent to reconnection at the NENL. Reconnection at the NENL results in the release of a BBF, and the production of an earthward propagating fast-mode which couples to the background field generating Pi2 pulsations observed on the ground. The inset panels (a)–(c) show three possible time lines, for $t_0 \rightarrow t_1 \rightarrow t_2$ of the relative times of observing a Pi2 pulsation on the ground and the in-situ observation of a BBF in the CPS. See text for details.

Wave Generation & Propagation – Pi2

Observed time delays and resultant Pi2 model [Uozumi et al., JGR 2009].

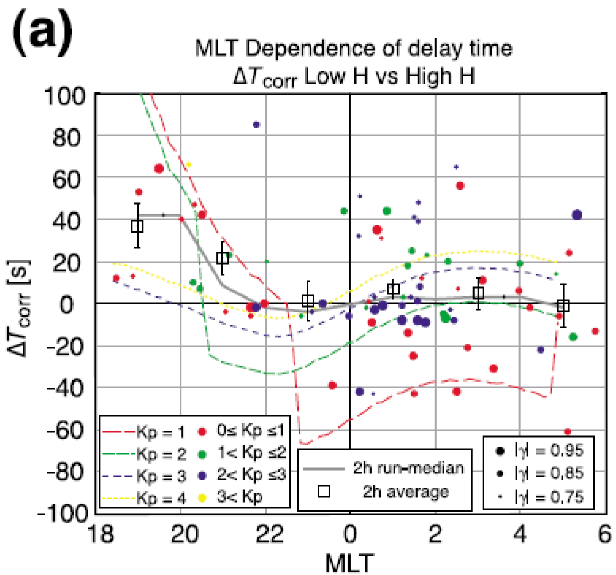

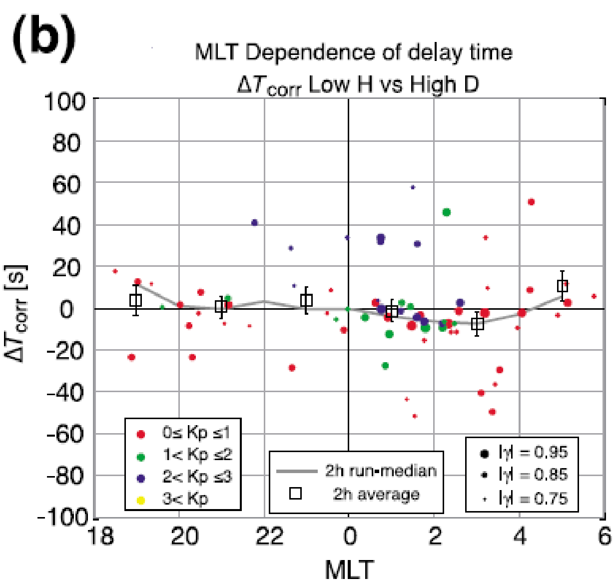

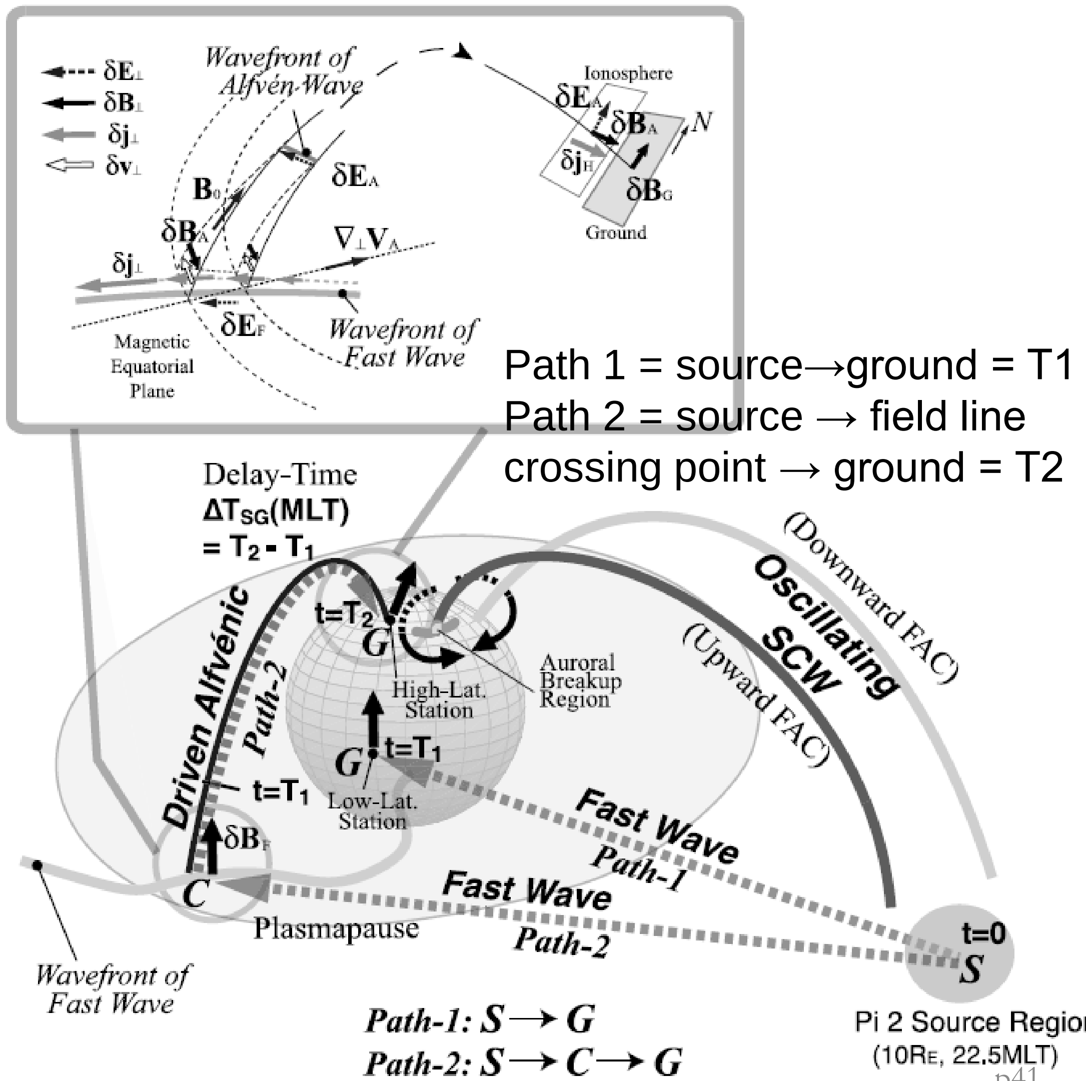

Path 1 = source→ground = T1
Path 2 = source → field line crossing point → ground = T2

Wave Generation & Propagation – Pi2

Spectral properties between THEMIS (L~2.6) poloidal components and ground H (L=1.35)[Kim et al., JGR 2010], and CHAMP (solid lines), HER (dashed; L=1.8), THY (dotted; L=1.8)[Sutcliffe & Lühr, JGR 2010].

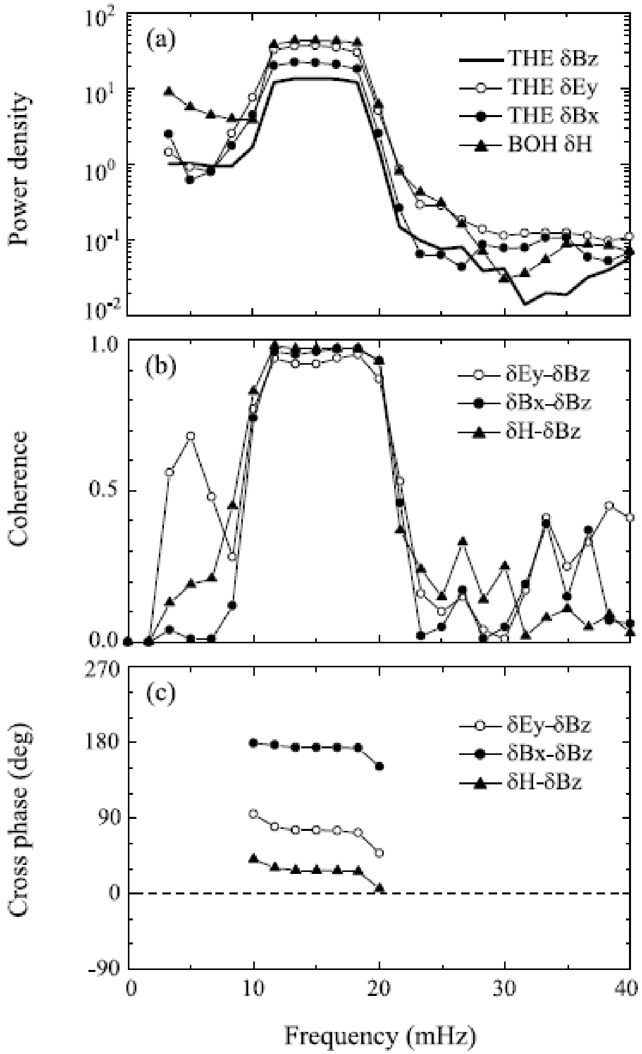

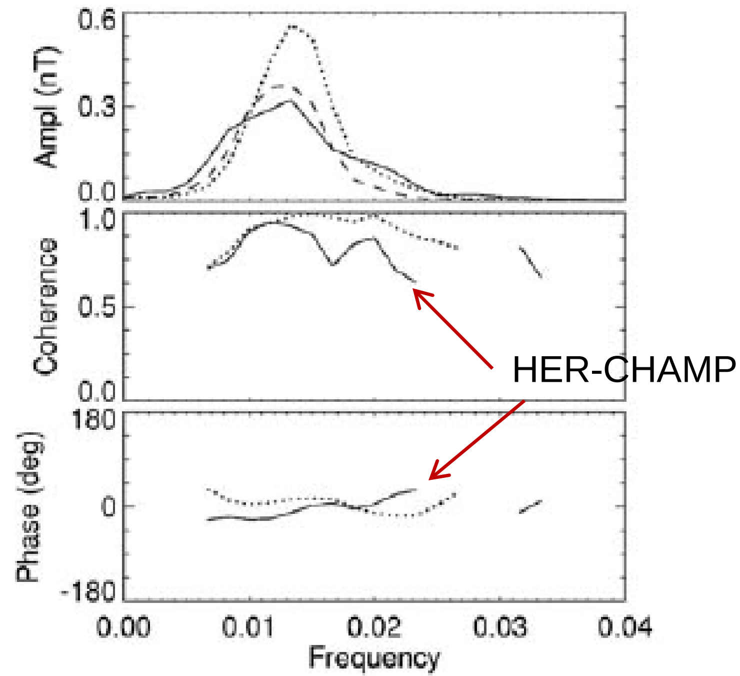

Wave Generation & Propagation – Pi2

Sutcliffe & Lühr did not see evidence for dayside Pi2 at CHAMP, and supported the Kikuchi & Araki [JASTP 1979] model. Electric fields due to FACs penetrate directly to low latitudes in an atmospheric waveguide. Toroidal currents flowing between the ionosphere and ground generate local magnetic fields.

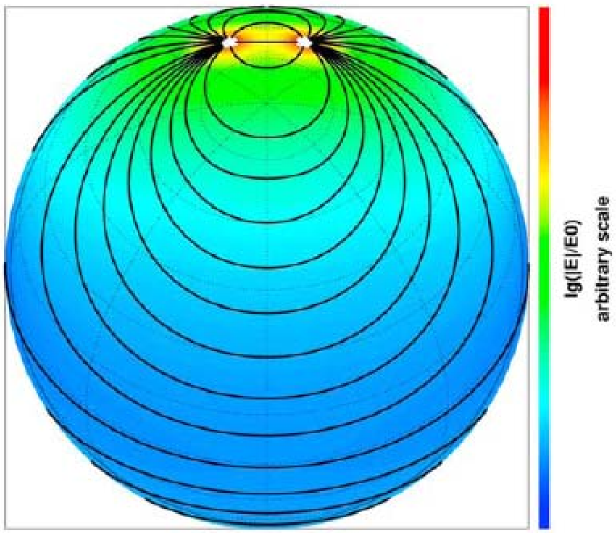

(b)

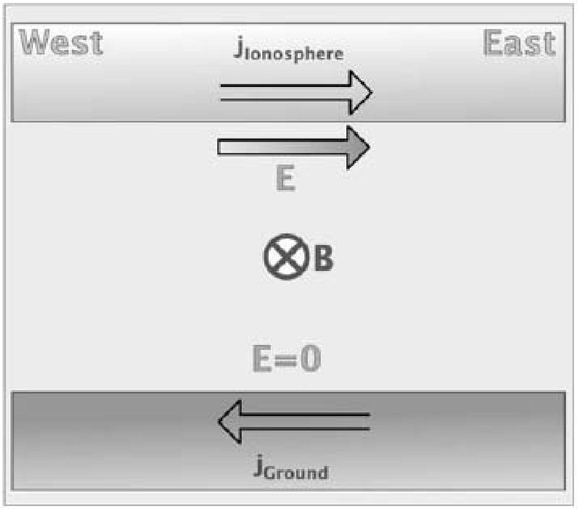

3.1 EMIC Waves – Modelling

Summary

Progress continues on modelling EMIC wave growth and propagation.

McCollough et al. [GRL 2009, JGR 2010] used a global 3-D MHD simulation to determine the temperature anisotropies and hot particle densities affecting the convective EMICW growth rate, with cold plasma densities derived from ground cross-phase measurements.

Ray tracing simulations of EMIC growth with bi- and non-Maxwellian ion distributions show strong wave gain near the plasmapause and at and within plumes [Chen et al., JGR 2009, 2010].

2-D hybrid simulations for a single and multi-ion plasmas in a dipole field [Hu & Denton, JGR 2009, 2010] show waves are generated near the equator and change from LH to linear as they propagate to the ionosphere, encountering resonances and stop bands.

EMIC Waves – Modelling

Summary (cont.)

Hybrid simulations using particle-in-cell methods in a uniform magnetic field describe the long-term nonlinear evolution of EMICWs, which may persist for some hours [Omidi et al., JGR 2010], and the scattering of hot and cool protons [Bortnik et al., JGR 2010].

Omura et al. [JGR 2010] developed a nonlinear wavegrowth theory for bursty LH EMIC triggered chorus emissions which emerge from nearly constant frequency EMICWs, describing the nonlinear interaction of protons with the seed EMICW and the time variation of the wave spectrum. Tsintsadze et al. [JGR 2010] described nonlinear excitation of magnetosonic waves through amplitude modulation of EMICWs.

Klimushkin et al. [JASTP 2010] showed that in a multi-ion plasma an equatorial resonator has closely spaced eigenfrequencies for quasi-perp propagation, and the harmonics may lead to pearl-like beating.

EMIC Waves – Modelling

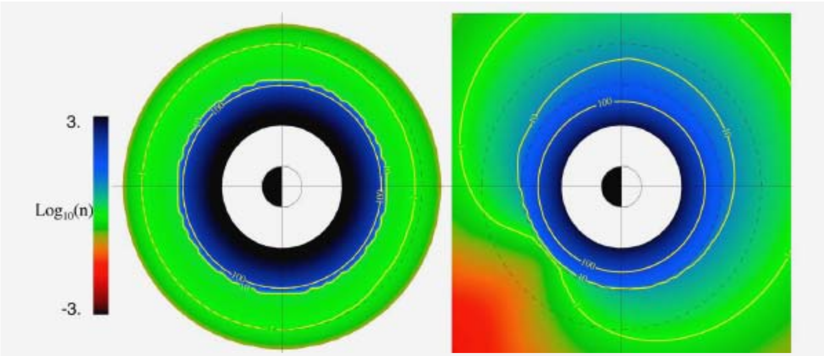

Cold H^+ density based on ground magnetometer cross-phase measurements (left) and GCPM plasma density distribution [McCollough et al., JGR 2010].

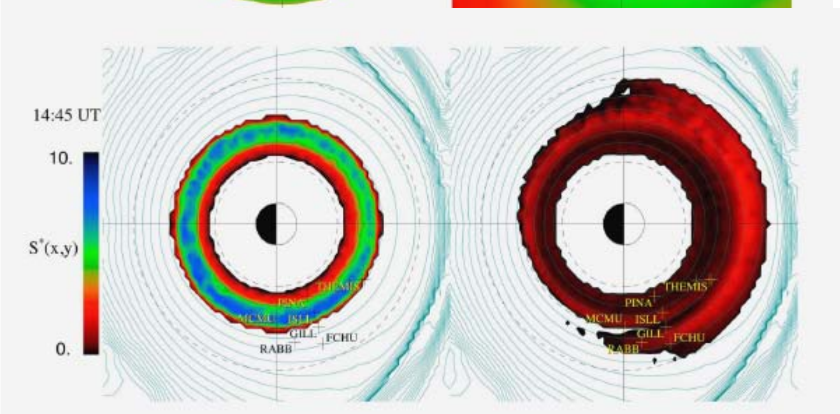

Resultant EMIC growth rates.

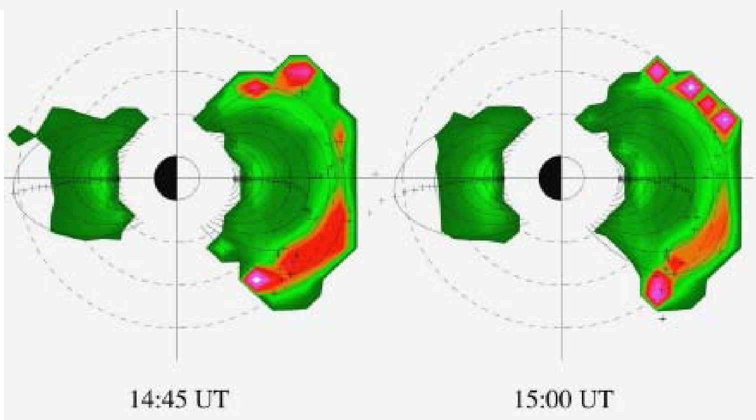

Temp anisotropy for warm H^+ in noon-midnight plane. Off equatorial field aligned nature suggests importance of Shabansky orbits.

EMIC Waves – Modelling

Cold plasma density distribution and resultant EMIC wave gain for a bi-Maxwellian hot proton distribution [Chen et al., JGR 2009]. Note waves in He^{+} band in trough and in plume density structures. A non-uniform ring current density profile and different plume densities were also evaluated.

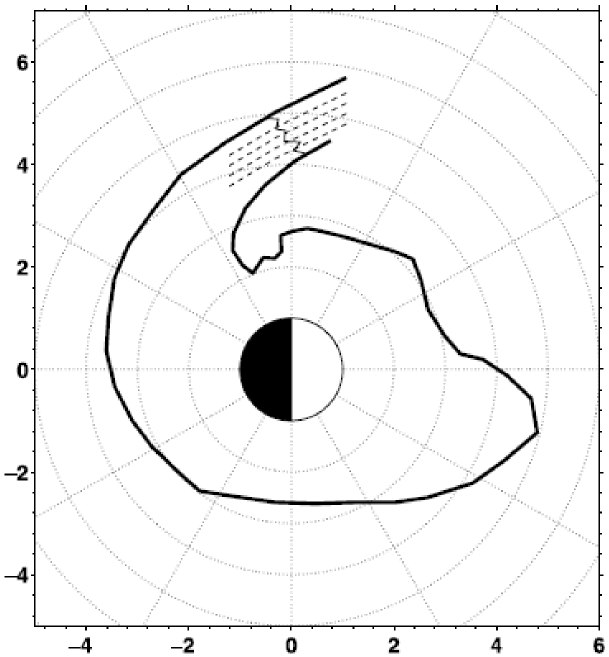

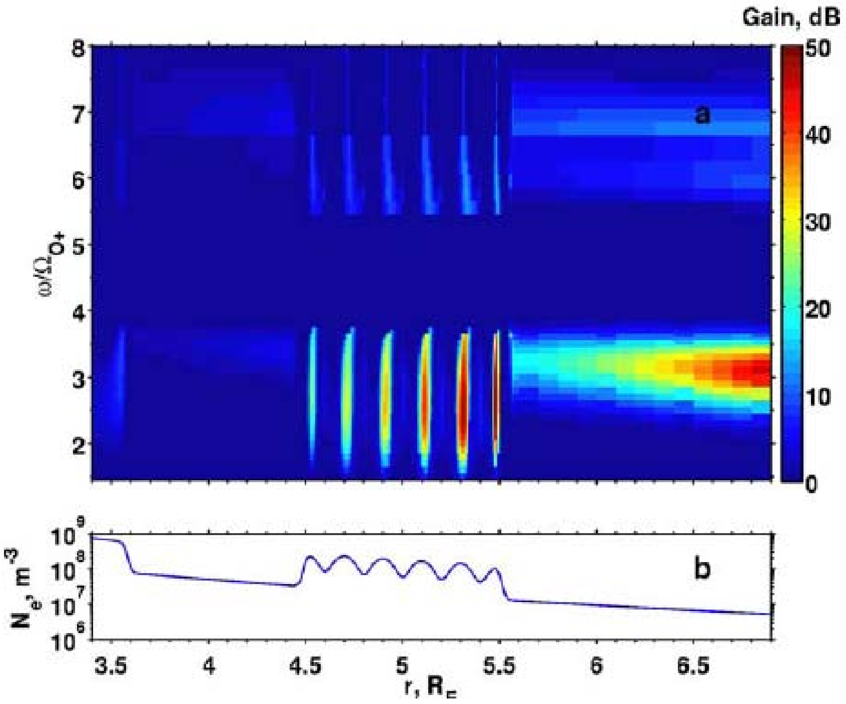

EMIC Waves – Modelling

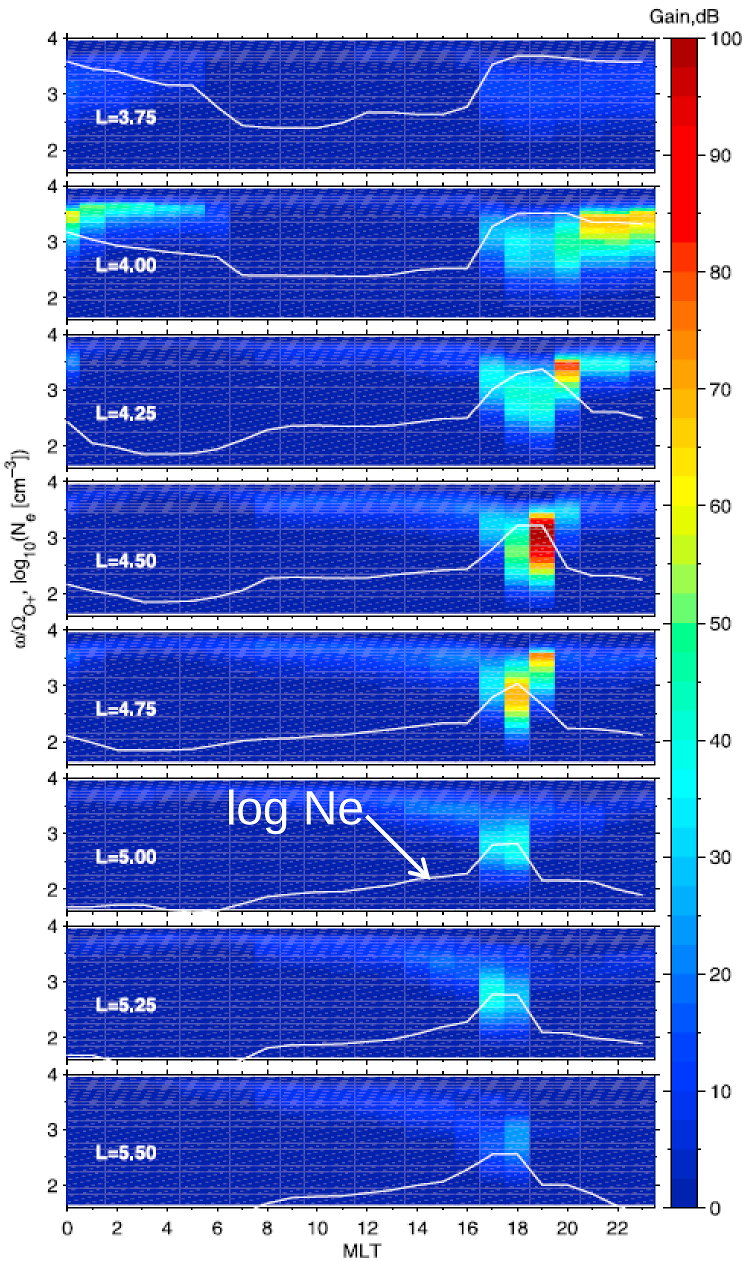

Global simulation of EMIC wave excitation during 21 April 2001 storm, using RCM/RAM simulation of ring current ion PSD and HOTRAY ray tracing code [Chen et al., JGR 2010]. He^+ band waves are preferentially excited inside and at the eastern edge of the plume, in the recovery phase, and may resonate with ≥3 MeV electrons.

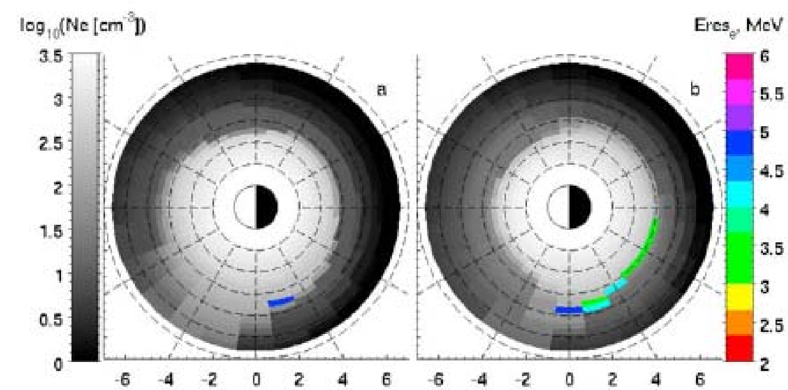

Figure 8. The region of EMIC wave excitation (with equatorial gain >30 dB) in the He^+ band is shown by the colored area for (a) $t = 40$ h and (b) $t = 48$ h. Color coding represents the minimum resonant energy of electron interacting with the excited EMIC waves. The equatorial density is also shown in gray scale on the background.

EMIC Waves – Modelling

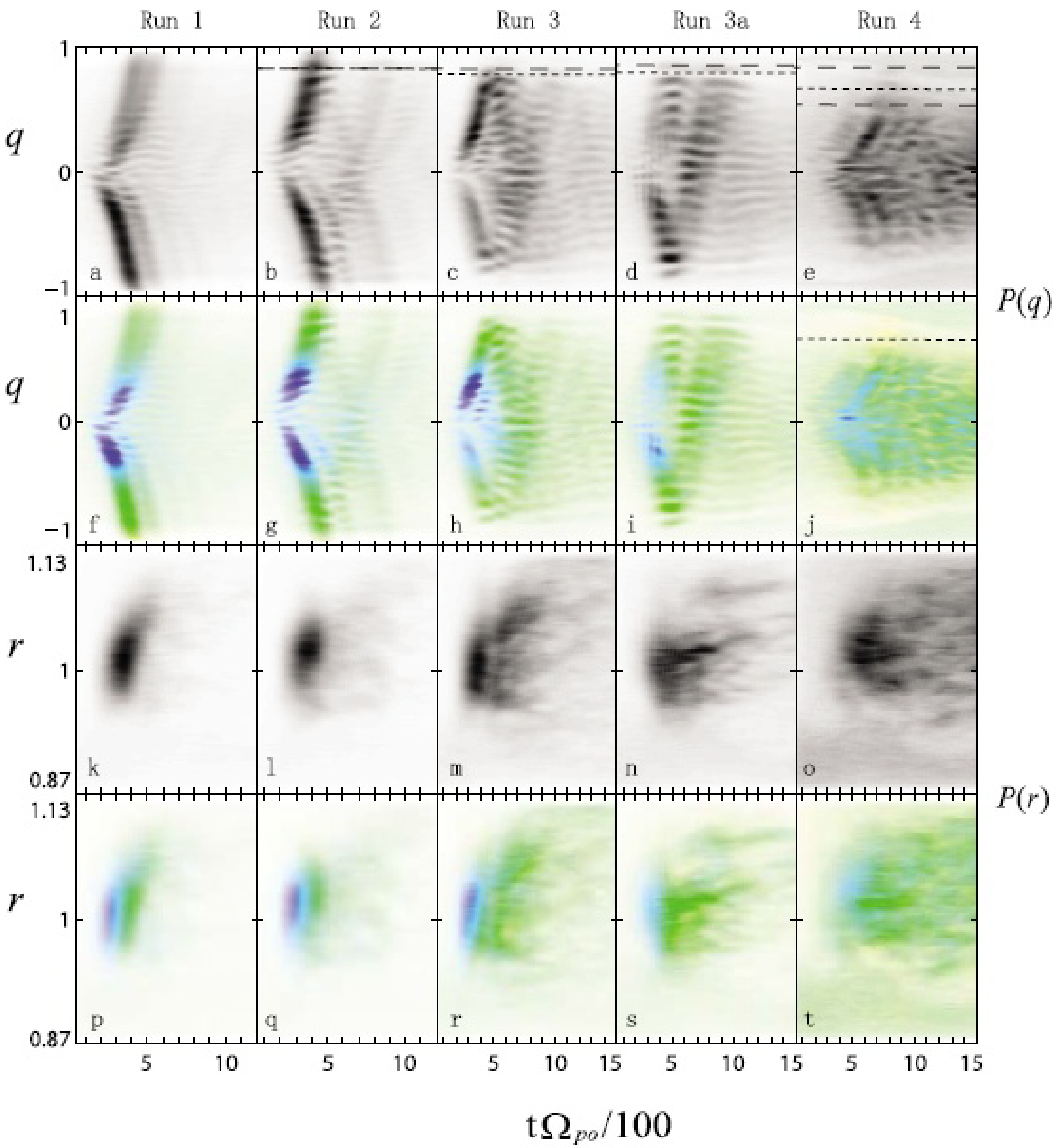

2-D hybrid simulations showing evolution of wave power in q (field-aligned), r (across flux tube) directions. O^+ density increases between runs. Colour represents ellipticity; dotted and dashed lines indicate bi-ion and cyclotron frequencies [Hu & Denton, JGR 2010].

Reflection occurs at the He^+-O^+ bi-ion frequency when O^+ density is high. Away from the source region the Poynting vector is mostly away from the equator.

EMIC Waves – Modelling

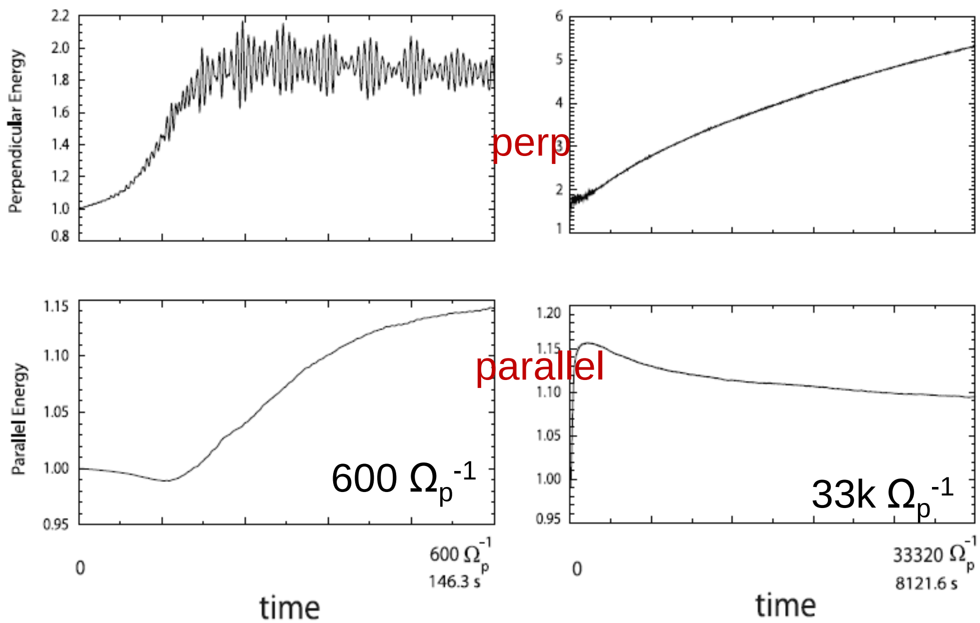

Time evolution of perp (top) and parallel cold proton energies, which grow at the expense of the hot protons [Omidi et al., JGR 2010]. The cool particles experience strong phase bunching and energy scatter in v_{perp} consistent with observations of cool heavy ion heating in space [Bortnik et al., JGR 2010].

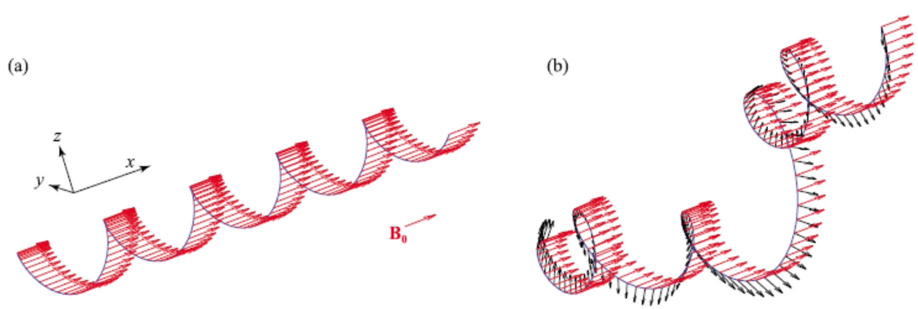

Figure 1. Trajectory of a proton test particle shown as the blue line, with superimposed local magnetic field vectors (red arrows) and local electric field vectors (black arrows), for (a) a uniform **B** field only and (b) a uniform **B** field, with simulated EMIC wavefield. The coordinate system is shown in Figure 1a, where $\mathbf{B_0}$ is aligned with the x axis.

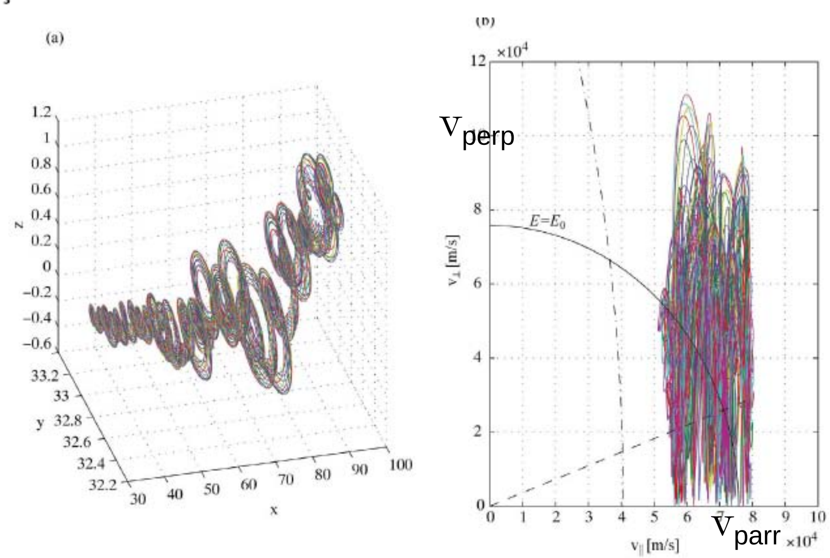

Figure 5. Trajectories of 12 proton test particles color-coded according to their initial Larmor phase, shown in (a) configuration space and (b) velocity space, in the same format as Figure 2.

3.2 EMIC Waves – Observations

Summary

Multipoint ground observations show seasonal, diurnal and frequency-dependent Pc1 polarization properties consistent with propagation from higher latitude sources [Nomura et al., JGR 2011], such as localised *L* shells near the plasmapause [Engebretson et al., JGR 2008; Usanova et al., GRL 2008, JGR 2010]. First in situ observations reported of LH dispersive rising tone chorus type EMICWs triggered during Pc1 activity [Pickett et al., GRL 2010].

In the polar regions, there is no Pc1-2 signature of the cusp, but bandlimited Pc1-2 waves originate from the plasma mantle, at the poleward edge of the cusp [Engebretson et al., JGR 2009].

Satellite surveys of EMICW occurrence [Halford et al., JGR 2010; Fraser et al., JGR 2010] show occurrence mostly in the main phase and near L=5.8 and 15 MLT.

3.2 EMIC Waves – Observations

Summary (cont.)

A survey using ground and GEO data found peak Pc1 activity before and in storm recovery phase, and only weakly related to plumes [Posch et al., JGR 2010], pointing to the role of compressions.

However, in situ observations confirm EMICW association with plumes [Morley et al., JGR 2009; Yuan et al., GRL 2010]. Morley et al also showed an association with 6 – 30 keV ion precipitation. Usanova et al. [JGR 2010] noted >30 keV ion precipitation with EMICWs.

In a 2 year morphological study, Yahnin et al. [JGR 2009] showed that proton aurora are likely connected with IPDP EMIC waves.

- How important are plumes as a source of EMICWs?
- How important are compressions as a trigger of EMICWs?

EMIC Waves – Observations

Below: EMICWs near the plasmapause associated with solar wind density enhancements but not Pc5 FLRs [Usanova et al., JGR 2010].

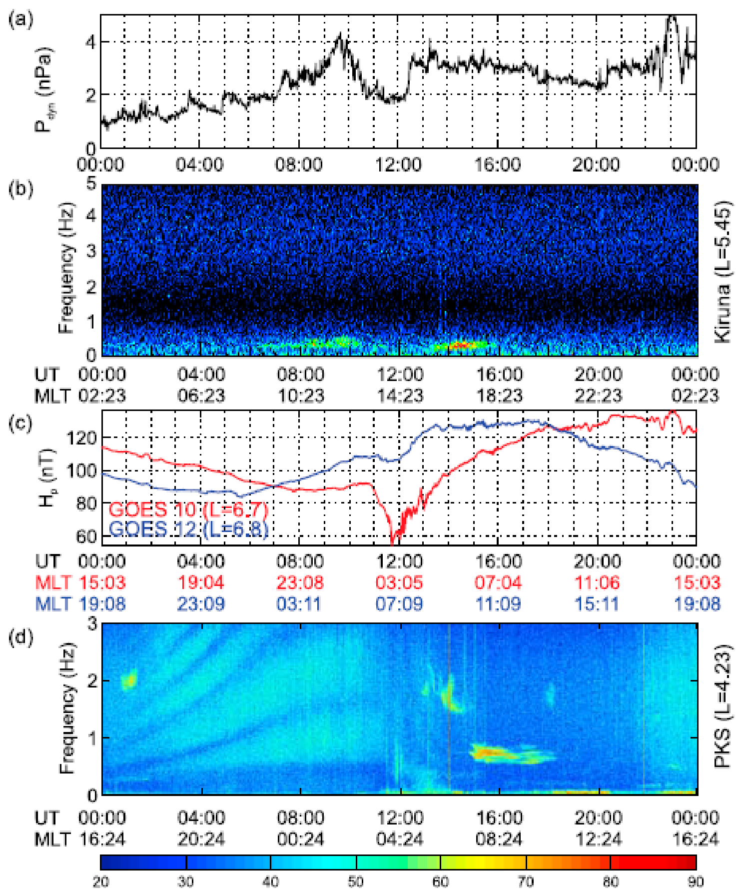

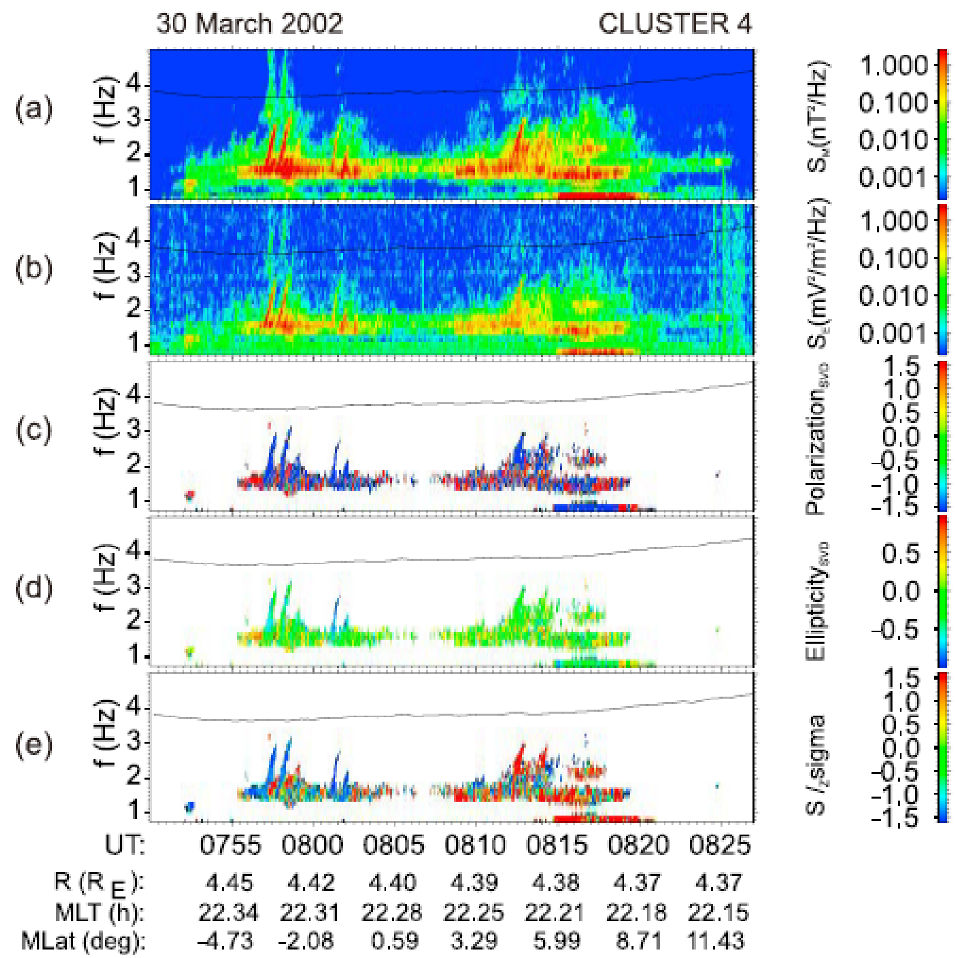

Pc1 waves ~1.5 Hz and triggered LH rising tone chorus emissions near the plasmapause [Pickett et al., GRL 2010].

EMIC Waves – Observations

Ground Pc1 occurrence and plumes for 133 storms relative to beginning of storm onset [Posch et al., JGR 2010]. Time resolution is 1 day or 2 hours.

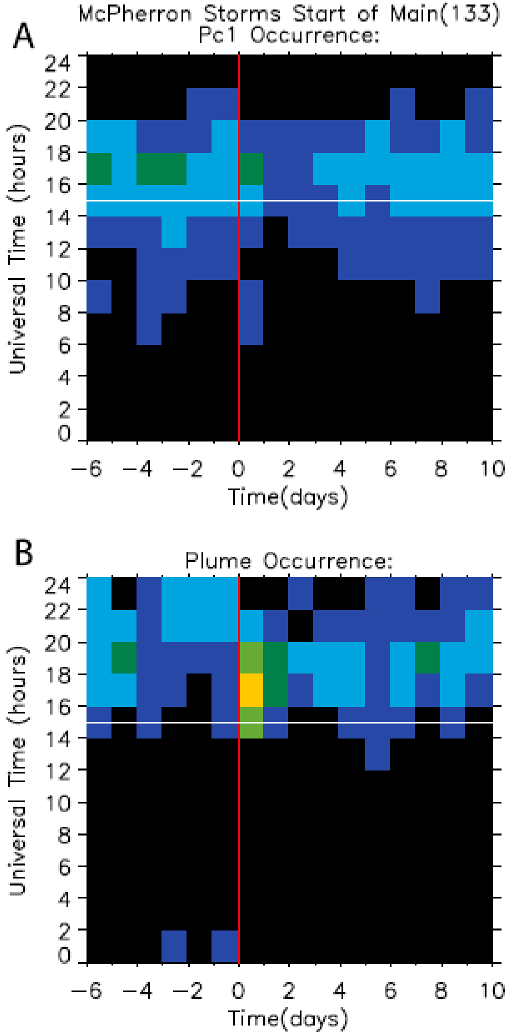

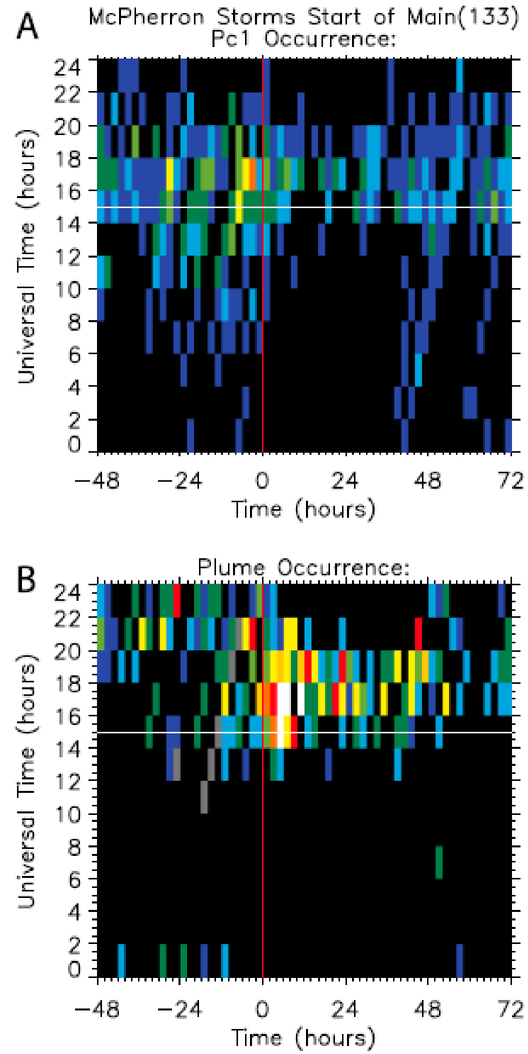

EMIC Waves – Observations

EMICW occurrence with a plume: at Cluster [Yuan et al., GRL 2010] and at GOES 9, DMSP and on the ground [Morley et al., JGR 2009].

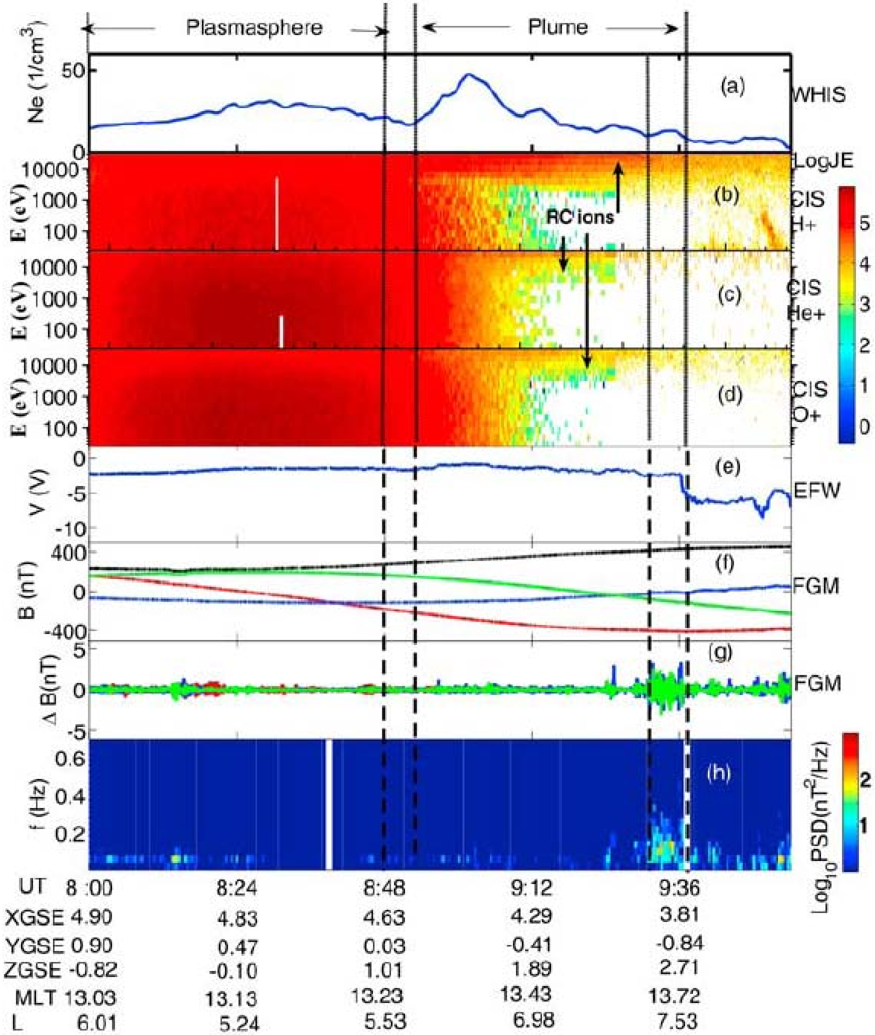

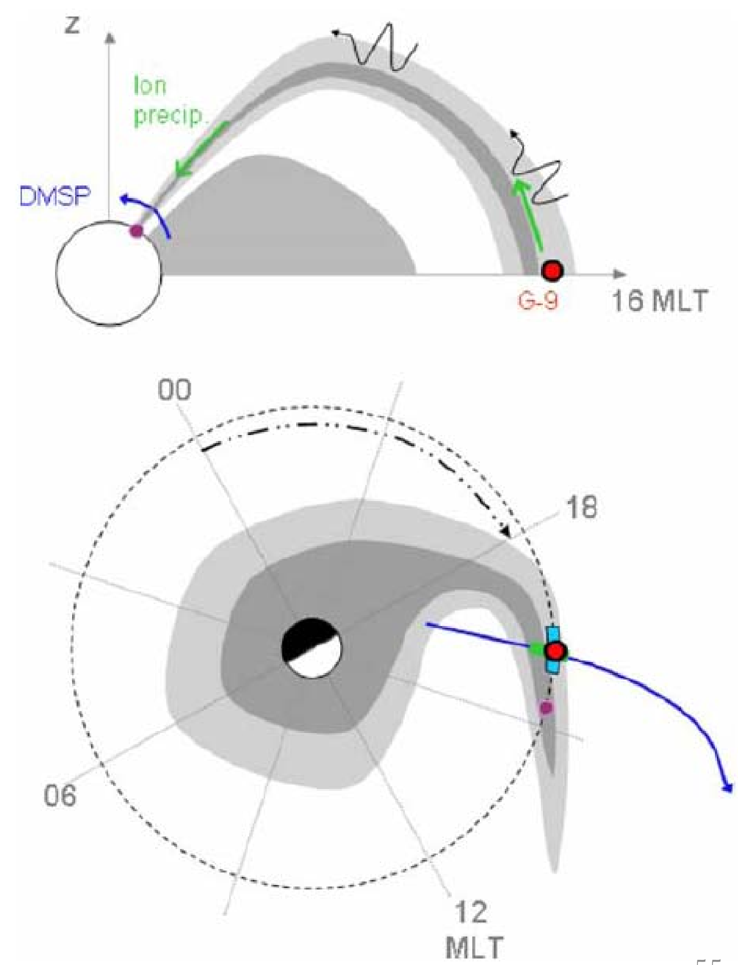

4.1 The Ionospheric Boundary – Effects on waves

Summary

MHD models with realistic ionospheric boundaries describe the effects of ionospheric conductivity on FLRs [Waters and Sciffer, JGR 2008], the mix (shear Alfvenic/fast mode) of wave modes incident on the ionosphere [Borderick et al., AG 2010], the ratio of equatorial electric field to ground magnetic field [Sciffer and Waters, JGR 2011], and FLR-induced phase changes in radio signals [Waters and Cox, AG 2009].

Observations and modelling confirm the existence of quarter-mode FLRs near the dawn terminator, mostly in winter or summer in the US sector [Obana et al., JGR 2009]. These arise due to the asymmetry in ionospheric conductivity at conjugate points.

Ionospheric heaters are being used to excite ULF waves on local magnetic field lines [Badman et al., AG 2009; Streltsov & Pedersen, GRL 2010; Kuo et al., GRL 2010].

The Ionospheric Boundary – Effects on ULF Waves

The F region vertical electron velocity V_z due to a downgoing 3 mHz wave with varying mode mix [Borderick et al., AG 2010].

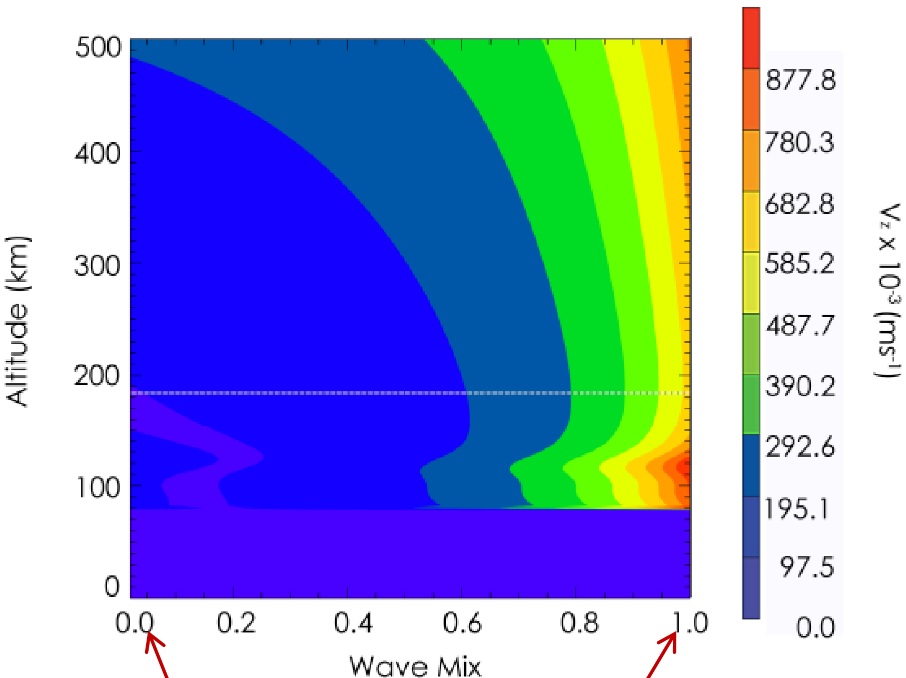

Purely fast mode

Purely shear Alfvenic

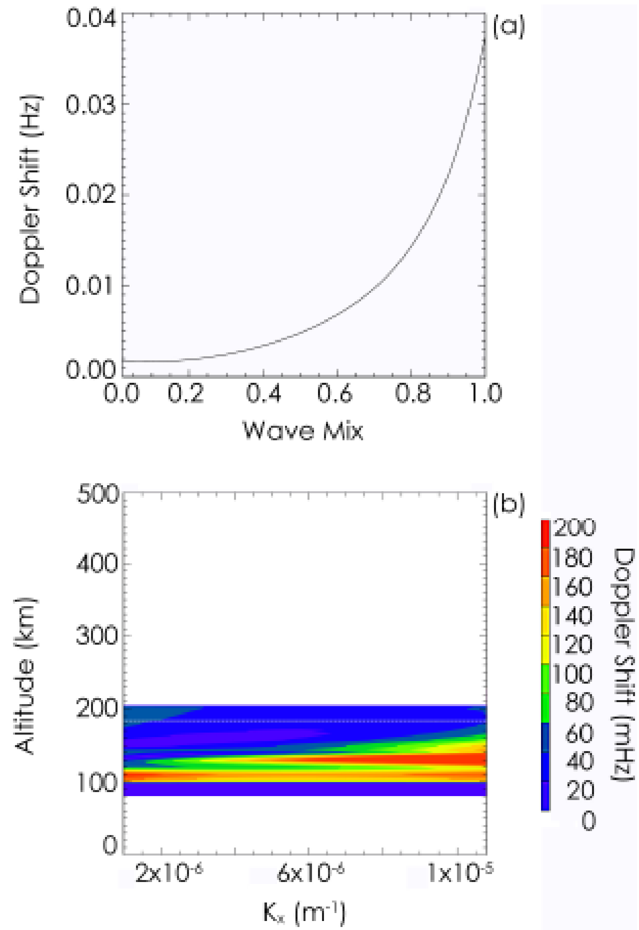

Variation of ionospheric Doppler shift with downgoing wave mode mix.

The Ionospheric Boundary – Effects on ULF Waves

Modelled variation in differential phase for a 70 MHz signal due to changes in TEC from a 50 mHz ULF wave with 80% shear Alfven mode at 1000 km altitude [Waters & Cox, AG 2009]

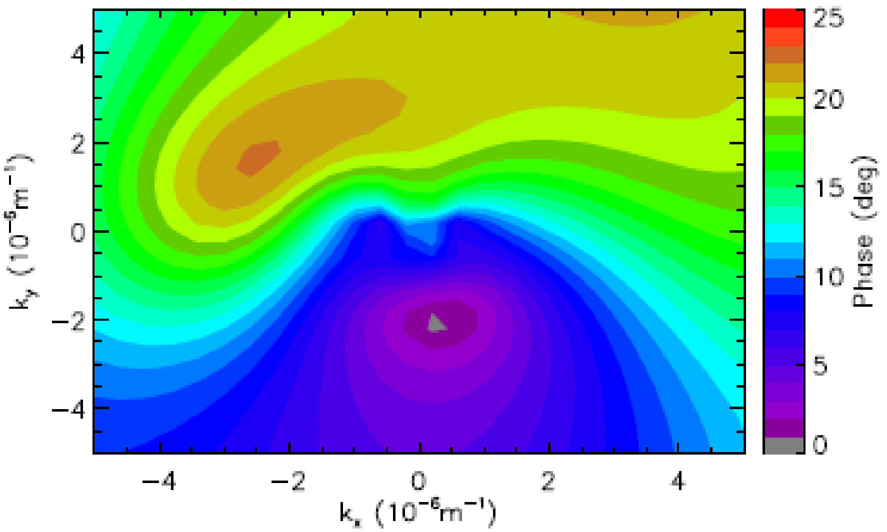

Fig. 4. The differential phases for noon and summer at L=1.6 (South Hemisphere) for a 70 MHz signal due to changes in TEC from a 50 mHz ULF wave as a function of the ULF wave spatial scale size. The ionosphere and neutral atmosphere parameters are the same as those used for Fig. 1. The upper boundary wave mode mix is 80% shear Alfvén mode.

The Ionospheric Boundary – Effects on ULF Waves

Quarter wave mode FLRs in the American summer sector [Obana et., JGR 2009].

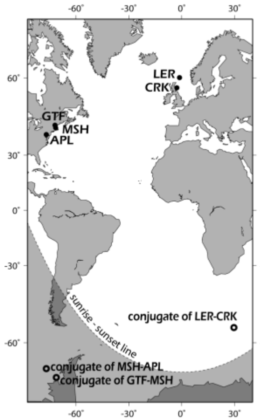

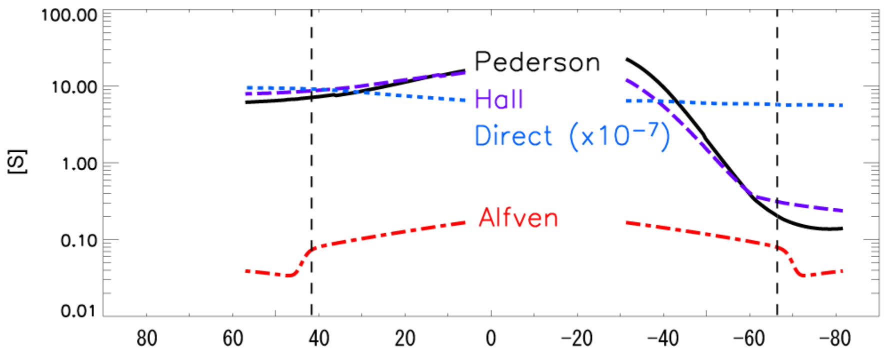

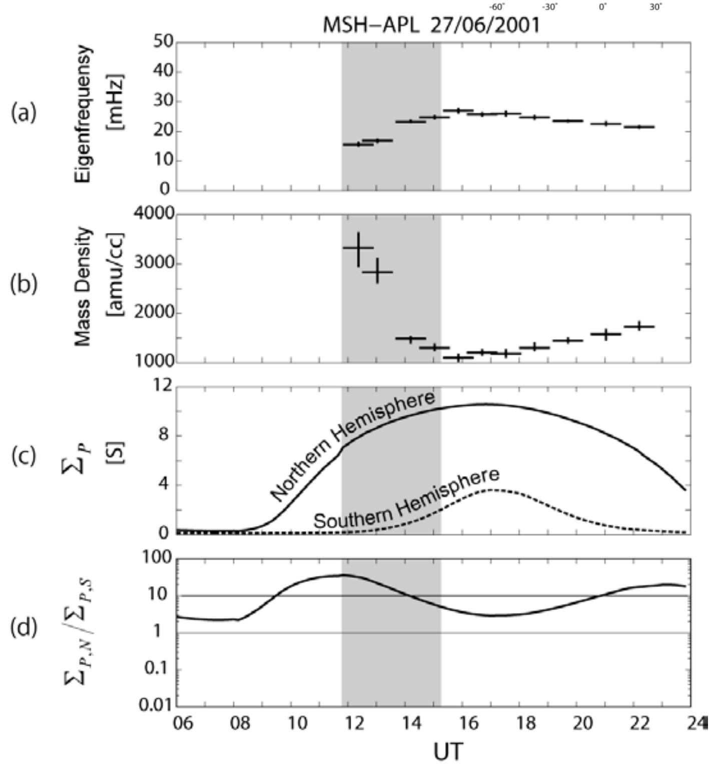

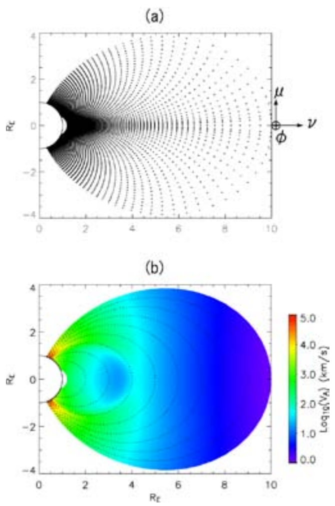

Model wave structure for 07 and 11 LT.

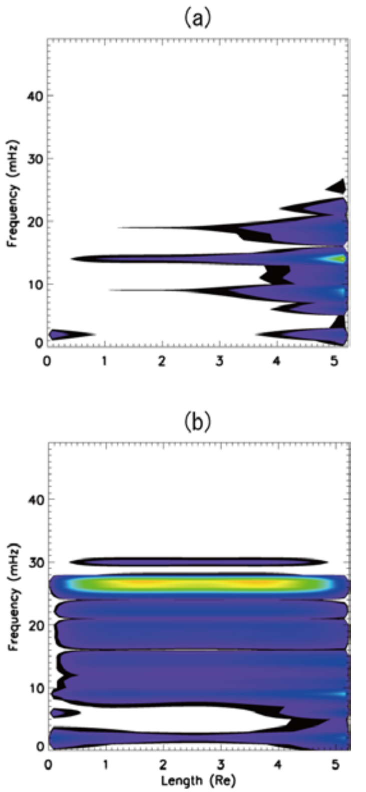

The Ionospheric Boundary – Effects on ULF Waves

Cluster observation of 1.67 mHz FLRs stimulated by ionospheric heating [Badman et al., AG 2009].

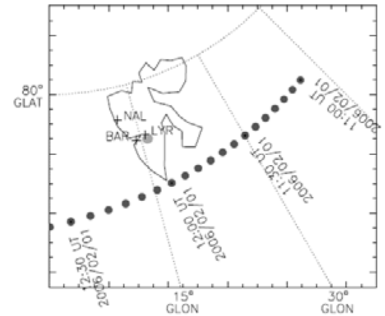

Cluster 2 track over ground stations.

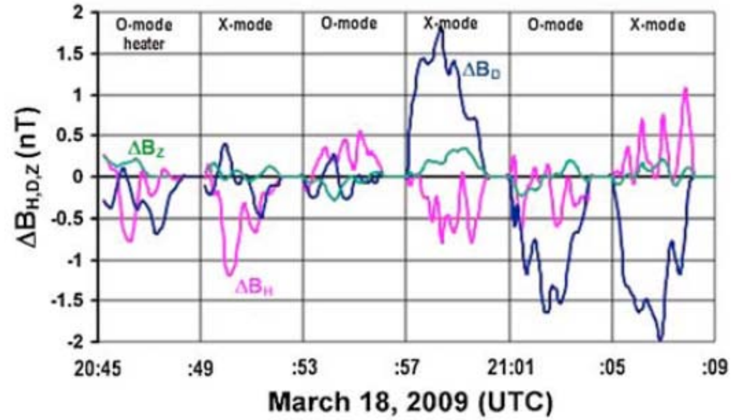

ULF pulsations produced by HAARP O- and X-mode pumping, 3:1 min on:off [Luo et al., GRL 2010]

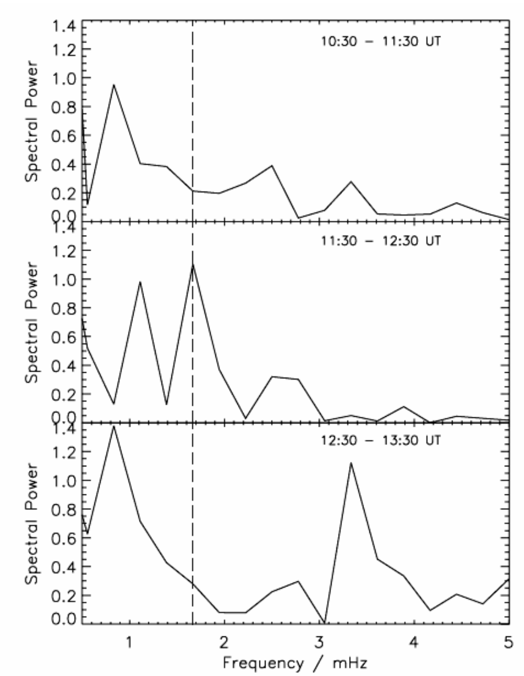

Cluster 2 spectrum before, during and after heating.

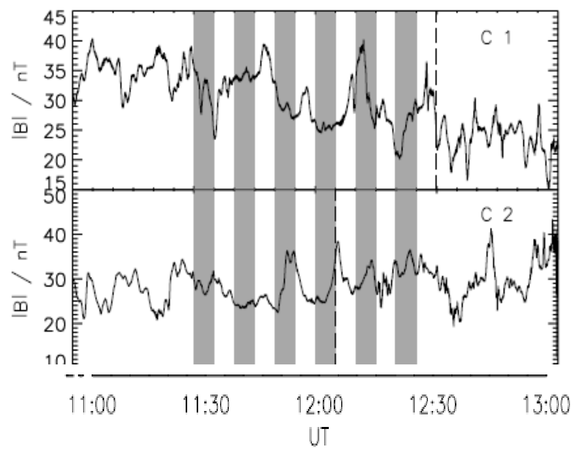

B field at Cluster 1 and 2 during heating intervals.

4.2 The Ionospheric Boundary – IAR

Summary

Numerical modelling has mapped the IAR spectral resonance structure (harmonic modulation in spectral density) in the Pc1 range for realistic ionosphere and magnetic inclination [Bösinger et al., AG 2009]. The IAR may be excited by worldwide lightning activity [Shalimov & Bösinger, JGR 2008].

Diurnal variations in IAR spectral resonance structure are disrupted by substorm precipitation effects [Parent et al., JGR 2010]. Hence F region density changes may dominate IAR variations.

Pc1 pulsations seen from -62° to -87° latitude and on CHAMP propagate poleward in the ionospheric duct at ~90 km/s and with ~8 – 20 dB/1000 km attenuation [Kim et al., JGR 2010].

The Ionospheric Boundary – IAR

Diurnal variation in IAR signatures (LH, RH polarized power, ellipticity, azimuth) disrupted by substorm onset (arrowed) [Parent et al., JGR 2010].

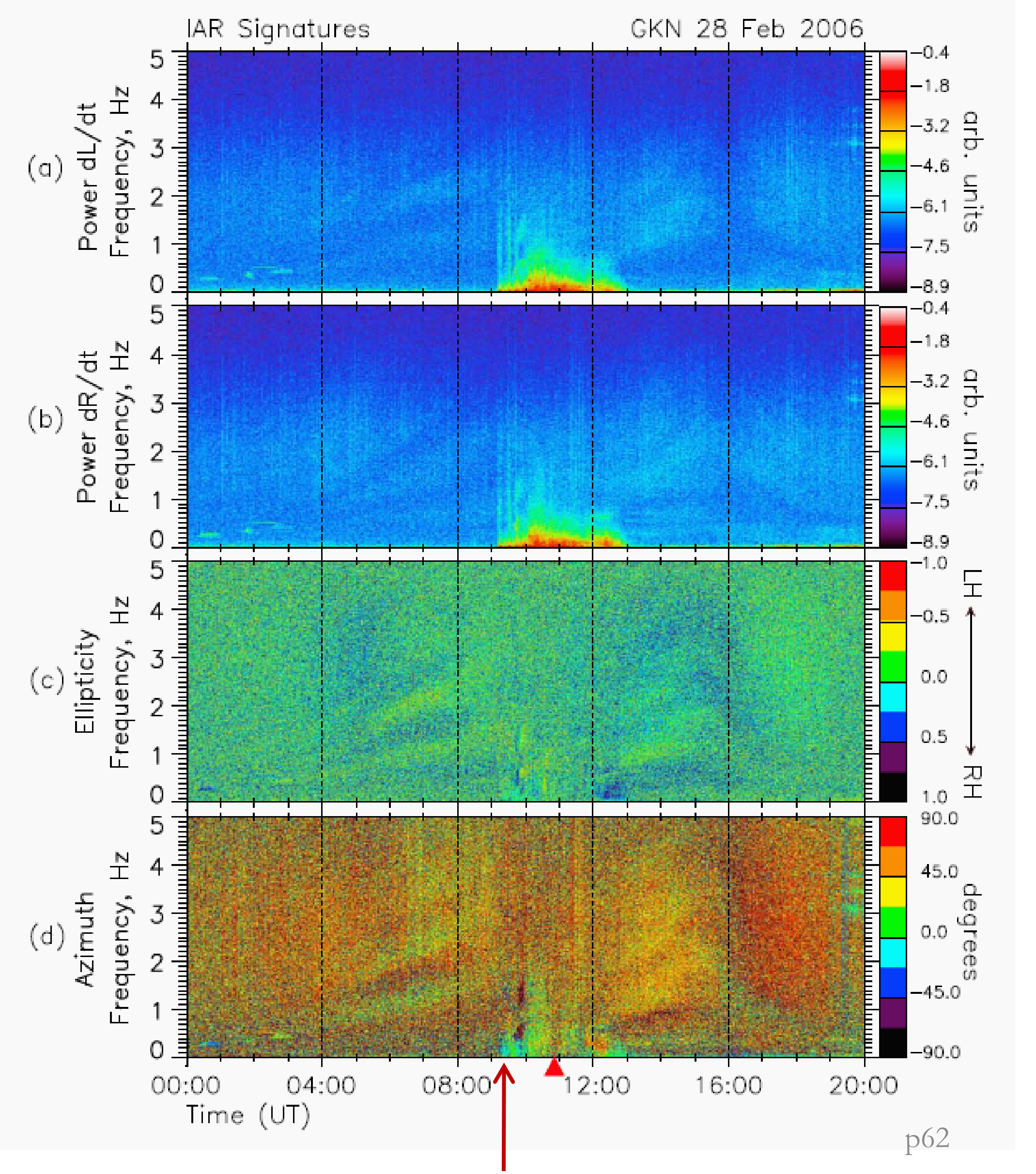

The Ionospheric Boundary – Wave Effects

Summary

ULF wave fields drive perturbations in the ionosphere. These are seen with radio sounders for FLRs at low [Menk et al., GRL 2007; Dyrud et al., GRL 2008] and high latitudes [Mthembu et al., AG 2009; Borderick et al., AG 2010], and for Pi2 [Gjerloev et al., GRL 2007; Ikeda et al., JGR 2010]. Models can explain the observations.

Many radar studies suggest that high-*m* waves are due to drift or drift-bounce resonance with azimuthally drifting protons [e.g. Baddeley et al., AG 2005a, b]. However, substorm injected electron clouds may produce intermediate-*m* poloidal waves with equatorward phase propagation [Mager et al., JASTP 2009; Yeoman et al, AG 2010].

Electric field oscillations associated with pulsation auroras are also seen with radars [Cosgrove et al., AG 2010], and ULF waves may modulate GPS TEC measurements [Skone, Radio Sci., 2009].

The Ionospheric Boundary – Wave Effects

Field of view and velocity variations for Hankasalmi radar of substorm associated intermediate-*m* waves with equatorward phase propagation [Yeoman et al., AG 2010].

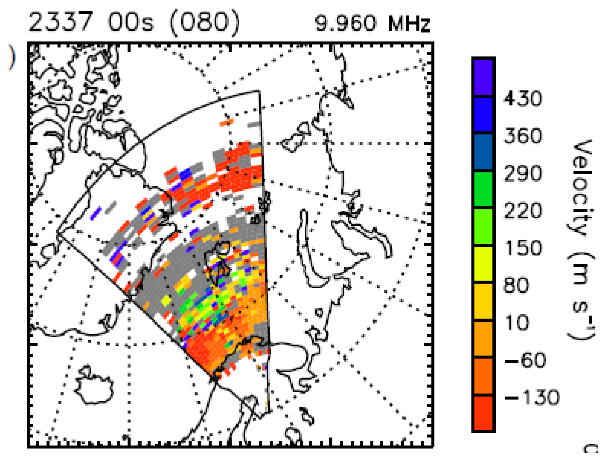

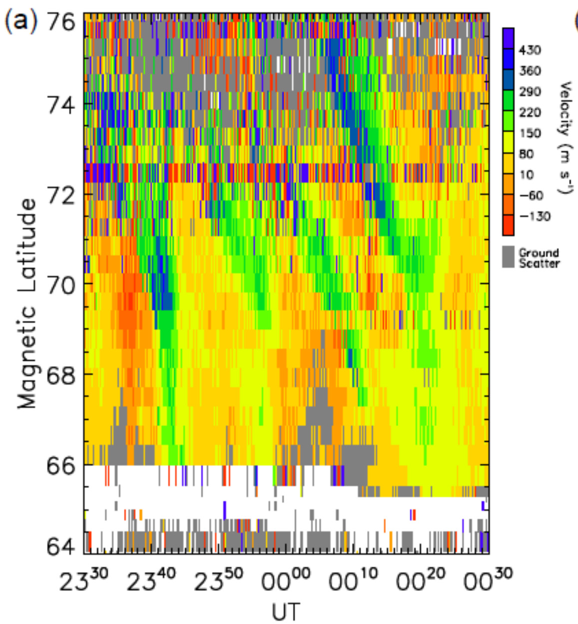

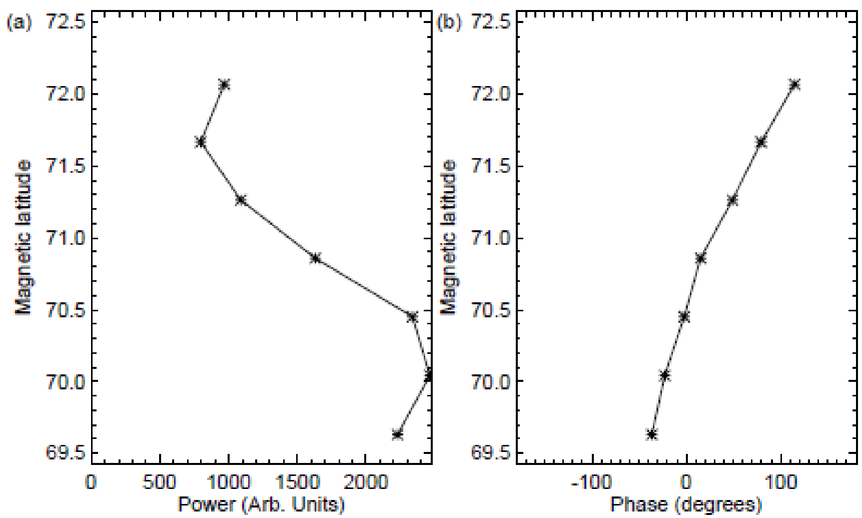

Phase variation is equatorward and exceeds that associated with FLRs.

The Ionospheric Boundary – Wave Effects

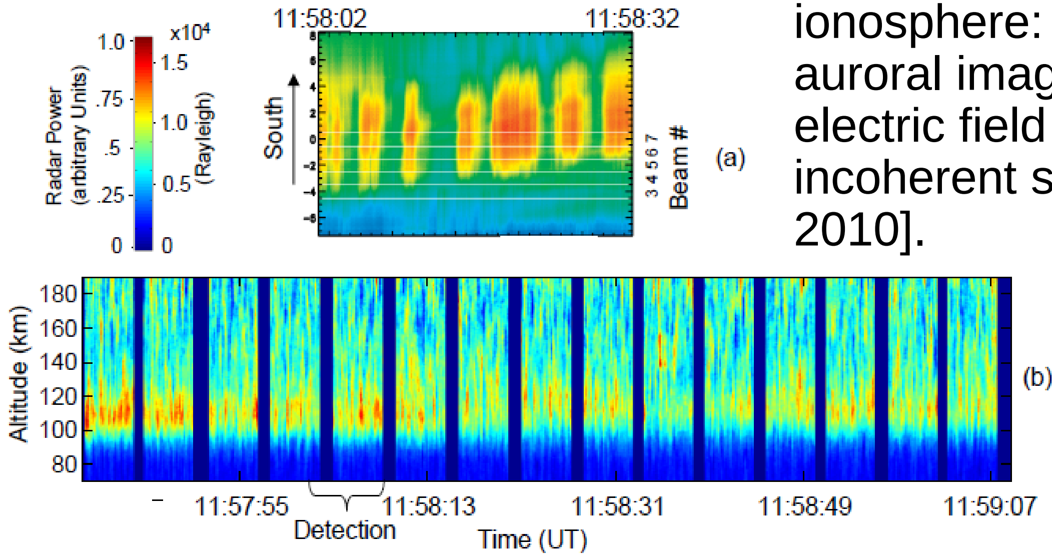

Signatures of kilometer scale waves in the ionosphere: 0.2 Hz and 1.4 Hz pulsations in auroral images (keogram, top) and 1.4 Hz electric field oscillations in Poker Flat incoherent scatter radar [Cosgrove et al., AG 2010].

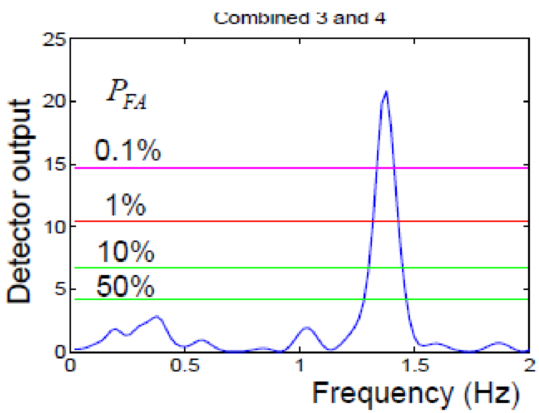

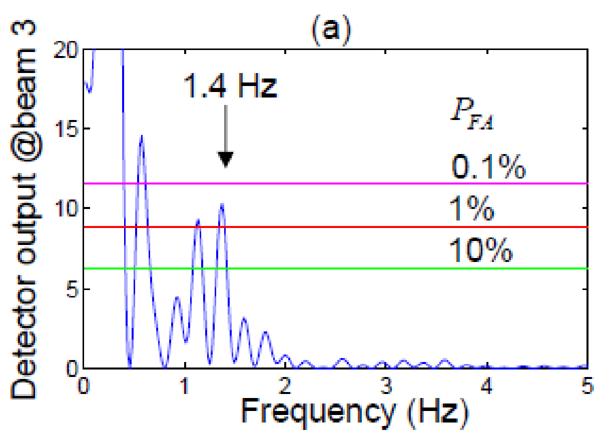

Radar (left) and keogram (right) spectra for time indicated above.

5.1 Applications – Remote Sensing

Summary

The use of ground ULF wave observations to monitor field line eigenefrequencies and hence magnetospheric density variations (“magnetoseismology”) is well established and includes plasmaspheric dynamics [Kale et al., JGR 2009], plasmaspheric plumes and biteouts [Takahashi et al., JGR 2008], and refilling [Dent et al., JGR 2006; Obana et al., JGR 2010a]. Comparison of mass with electron densities allows the plasma composition to be determined [Grew et al. GRL 2007].

Ground cross-phase determinations of plasmapause location generally agree with EUV He^+ determinations at solar maximum (IMAGE) and minimum (Kaguya) within 0.4 R_E [Obana et al., JGR 2010b].

Surveys using FLR data from low latitude ground stations [Vellante et al., JGR 2007] and geostationary orbit [Takahashi et al., JGR 2010; Denton et al,. JGR 2011] have provided empirical models of the solar cycle variation in FLR frequency and bulk ion mass loading.

Applications – Remote Sensing

Summary (cont)

The field-aligned density distribution may be enhanced in the afternoon sector at GEO [Takahashi and Denton, JGR 2007] and ~4.8 R_E [Denton et al., AG 2009] but power law models usually suffice for FLR density determinations [Maeda et al., ASR 2008].

Radial field line motions due to poloidal mode ULF waves cause Doppler shifts in VLF signals [Menk et al., JGR 2006] and modulate kHz range nonthermal continuum radiation near the plasmpause [Grimald et al., JGR 2009].

- Are plasma plumes readily detected by ground-based methods, and do they contain a significant heavy ion population?
- Further calibration studies are required to compare ground-based density inferences with in situ measurements and improve the precision of composition estimates.
- How does plasma composition vary with magnetic activity and *L*?

Applications – Remote Sensing

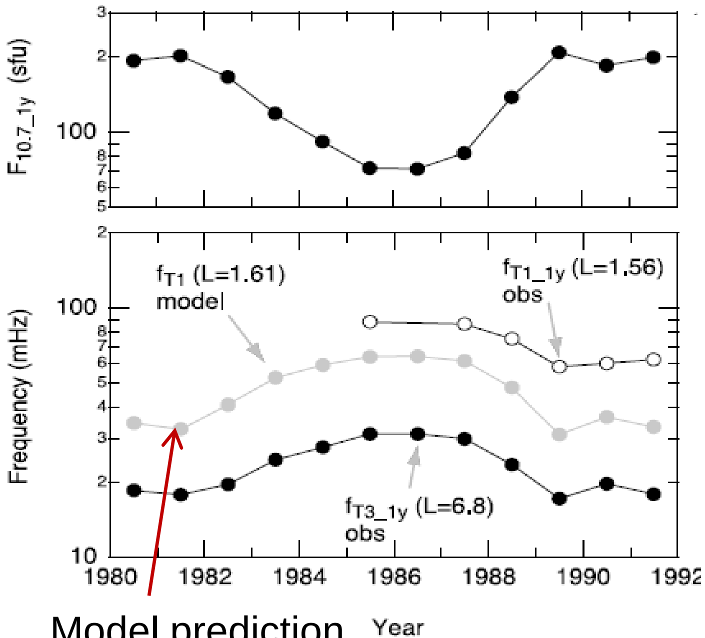

Model prediction

Correlation between $F_{10.7}$ flux and FLR frequency at GEO [Takahashi et al., 2010], density at GEO [Denton et al., JGR 2011] and at L=1.6 [Vellante et al., 2007].

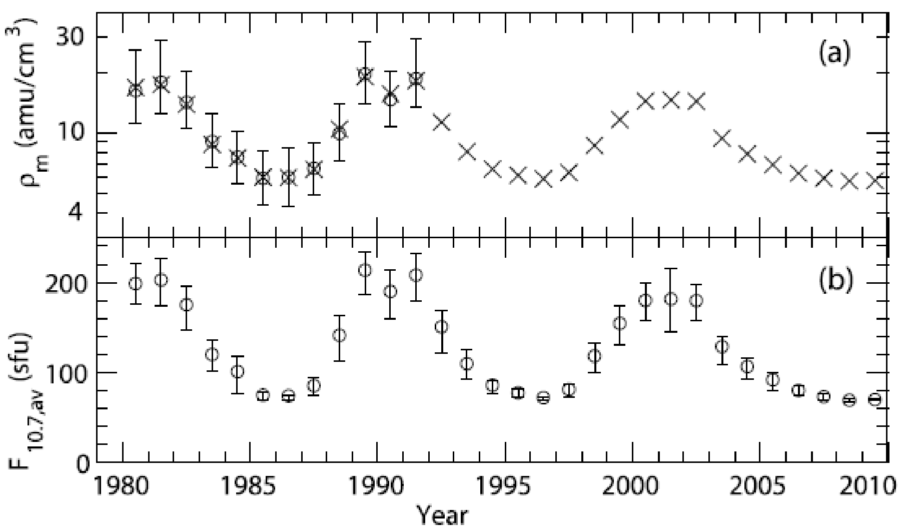

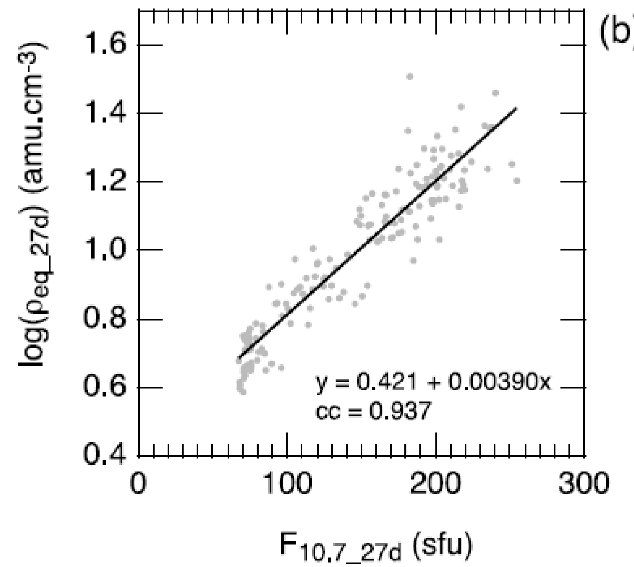

Correlation between 27 day averages of log mass density at L=6.8 and $F_{10.7}$ flux.

Applications – Remote Sensing

Hourly post-storm mass density refilling rates [Obana et al., JGR 2010].

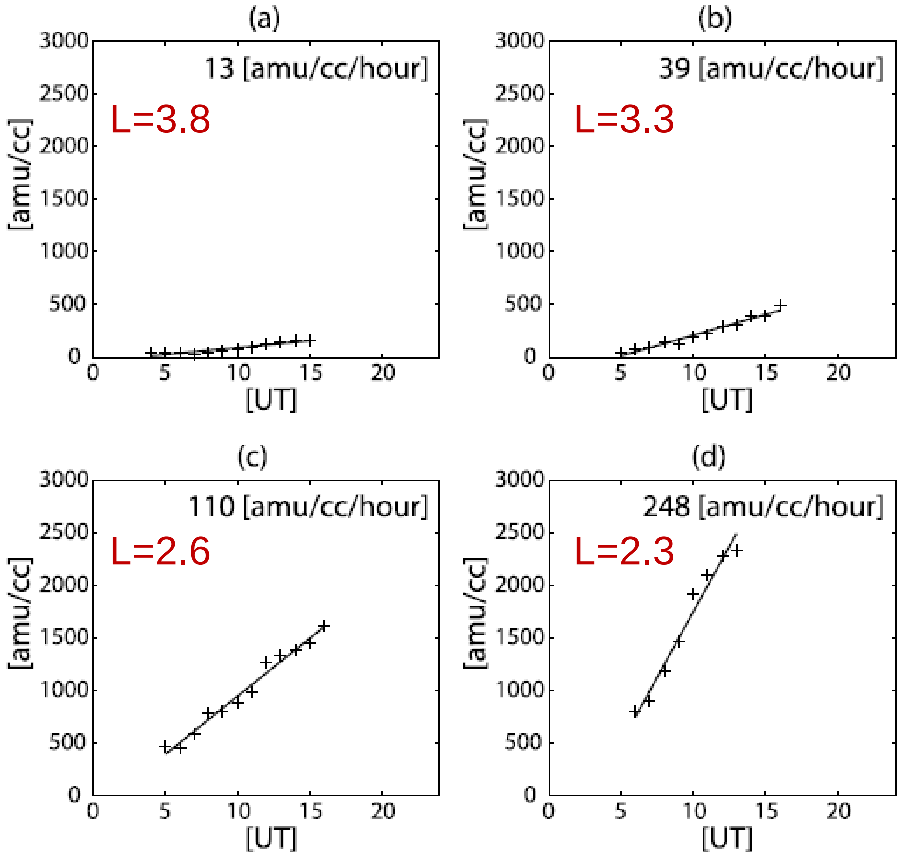

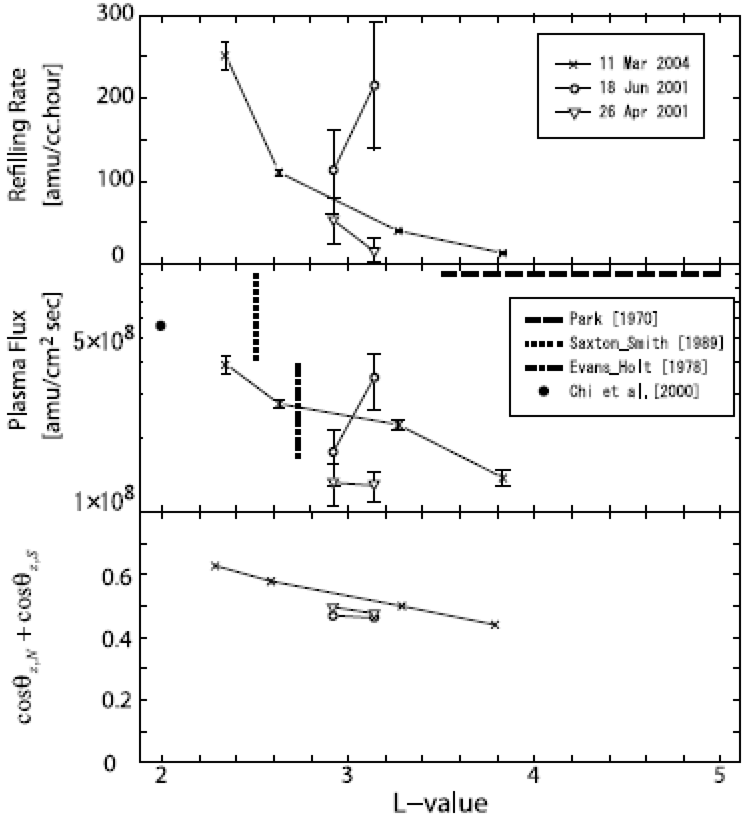

L-shell dependence in refilling rate (top) and upward flux (middle) is not explained by *L*-variation in summed solar zenith angles..

5.2 Applications – Transport of Energetic Particles

Summary

Trapped electrons may be energized by drift resonance interactions with low-*m* Pc5 waves [Degeling et al., JGR 2008; Huang et al., JGR 2010a,b] e.g. with compressions [Ukhorskiy and Sitnov, JASTP 2008; Zong et al., 2009; Loto'aniu et al., JGR 2010]. Large amplitude internally generated high-*m* storm-time Pc5 may also be important [Ozeke and Mann, JGR 2008].

Poloidal mode high-*m* standing Pc5 waves may undergo bounce-resonance interaction with energetic electrons and radiation belt O^+ ions [Yang et al., JGR 2010,2011a,b]. EMICWs may energize He^+ ions [Zhang et al., JGR 2010].

- What are the relative contributions to particle energization of broadband low *m* Pc5 waves, adiabatic transport by compressional waves, high-*m* waves in the ring current, and EMICWs?

Applications – Transport of Energetic Particles

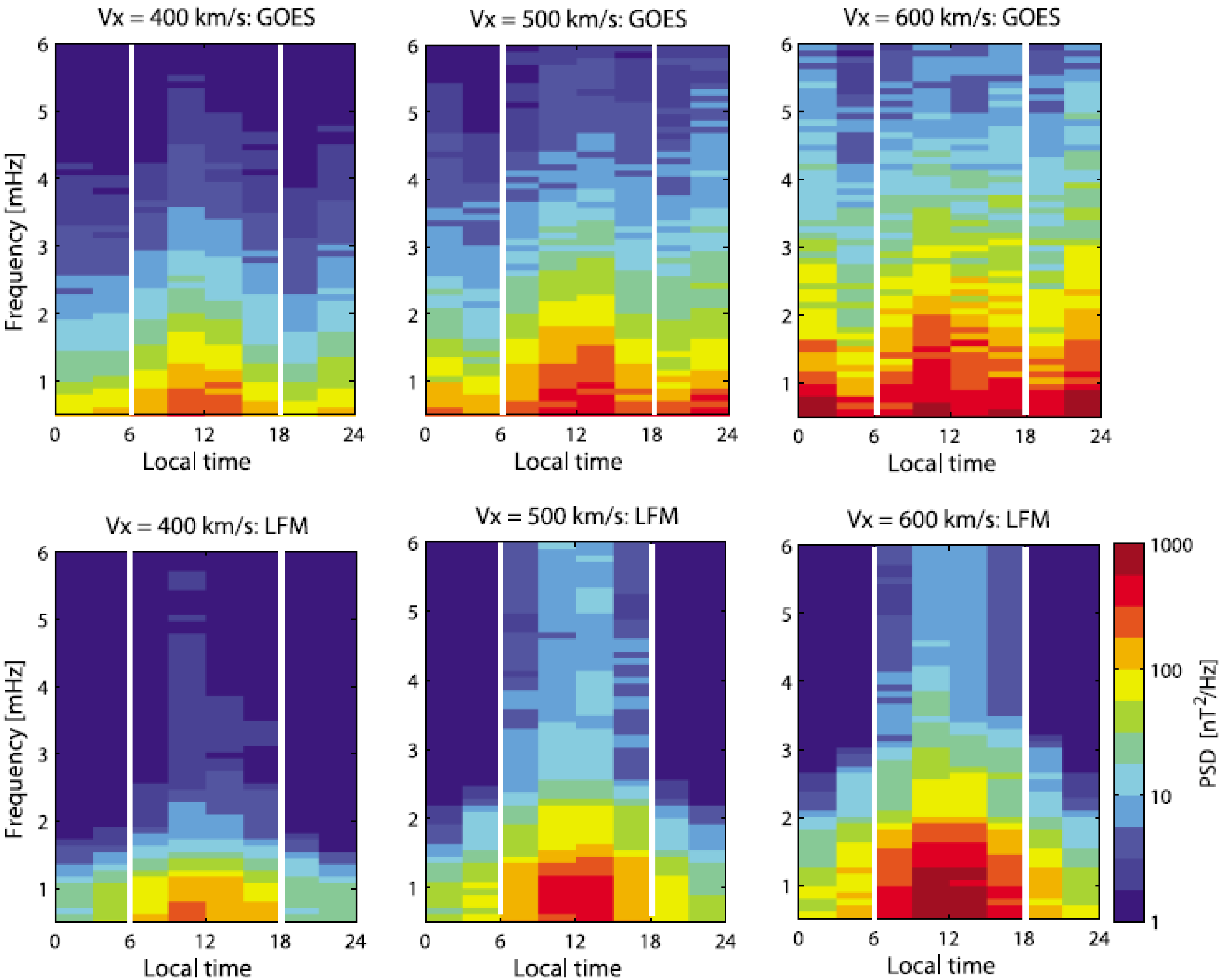

Observed GOES Pc5 PSD over 9 years (top) and LFM model predictions (bottom) which are then used to determine radial diffusion coefficients [Huang et al., JGR 2010].

5.3 Applications – Loss of Energetic Particles

Summary

Many studies confirm that EMICWs may cause pitch angle scattering and precipitation into the atmosphere of energetic electrons. These include observations of wave proxies [Sandanger et al., JASTP 2009; Blum et al., JGR 2009] and event analysis [Ukhorskiy et al., GRL 2010], and numerical simulations [Liu et al., JGR 2010; Su et al., JASTP 2011; Xiao et al., JASTP 2011].

A new global network of VLF receivers detects sub-ionospheric signatures of relativistic electron precipitation [Clilverd et al., Space Weather 2009]. This has provided evidence of relativistic precipitation over $3<L<7$ for 10 – 15 days after recurrent storms associated with enhanced power in the Pc1-2 range but not in the Pc4-5 range [Clilverd et al., JGR 2010]. Such precipitation had earlier been connected with IPDP [Rodger et al., GRL 2008].

Applications – Loss of Energetic Parcticles

Storm epoch comparison of times an EMICW growth parameter exceeds the instability threshold, for over 300 storms in which post-storm relativistic electron fluxes were or were not seen in the radiation belts [Blum et al., JGR 2009].

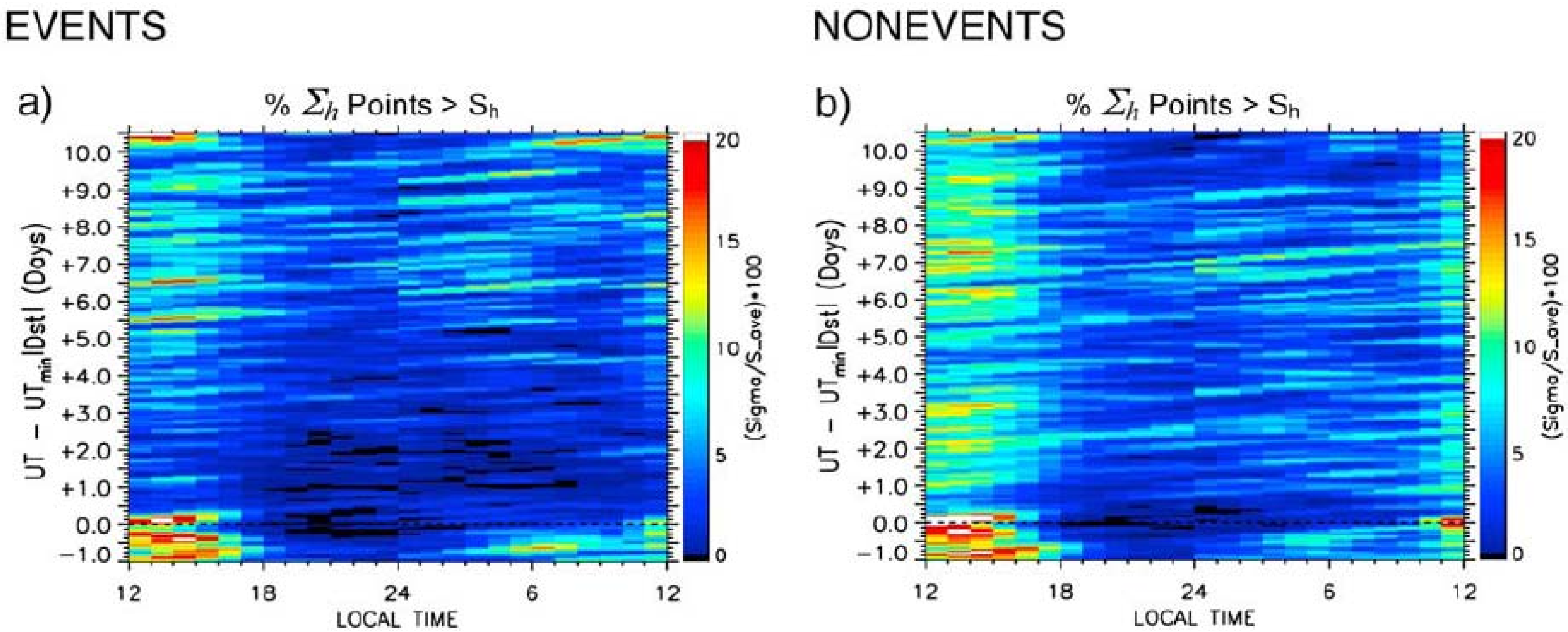

Applications – Loss of Energetic Parcticles

Subionospheric precipitation driven by IPDP EMICWs [Rodger et al., GRL 2008].

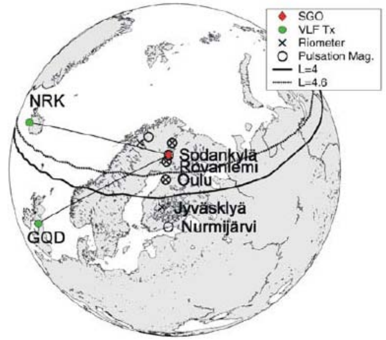

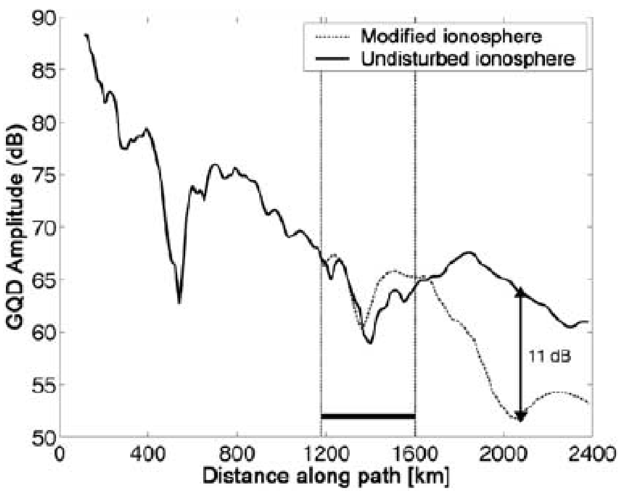

Modelled response assuming 2 MeV electron flux in region shown. Main effect is at 60 km altitude.

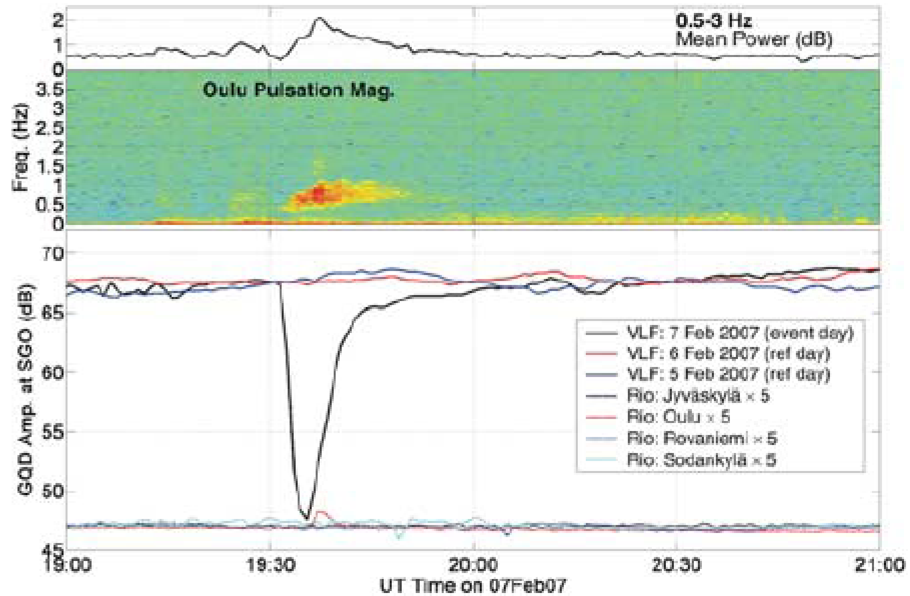

Figure 2. (top and middle) Oulu (L = 4.6) pulsation magnetometer data from 19–21 UT on 7 February 2007 indicating the presence of IPDP EMIC activity occurring during a minor geomagnetic disturbance (Kp = 3.7, D_{st} = −12 nT). (bottom) Contrast between the subionospheric precipitation monitor amplitude of GQD for 3 days centered on the event day (solid lines) and the absorption data from the Finnish riometer chain (dotted lines) on 7 February 2007. The riometer absorptions have been multiplied by 5 and shifted so as to appear on this plot.

5.4 Applications – Other

Summary

Techniques for identifing ULF wave properties include a beamformer FLR detector [Plaschke et al., AG 2009]; Wigner-Ville distributions [Chi & Russell, JGR 2008]; maximum entropy analysis [Ndiitwani & Sutcliffe, 2009]; Hilbert-Huang and S transforms [Kataoka et al., JGR 2009]; and the Meyer discrete wavelet transform [Milling et al., GRL 2008; Murphy et al., JGR 2009; Rae et al., JGR 2009a,b, JGR 2010]. The latter two are useful for decomposing and timing ULF waveforms at substorm onset. Wave-based substorm timing has been extended into space [Walsh et al., JGR 2010].

Debate continues on whether ULF waves can precede seismic events [Campbell, JGR 2009; Thomas et al., GRL 2009; Masci, JGR 2010].

Consistent amplitude and phase relationships are observed between ULF signals and induced currents in long oil and gas pipelines at low latitudes [Marshall et al., Space Weather 2010].

Applications – New Techniques

Example of Hilbert-Huang transform based empirical mode decomposition of substorm waveforms [Kataoka et al., JGR 2009].

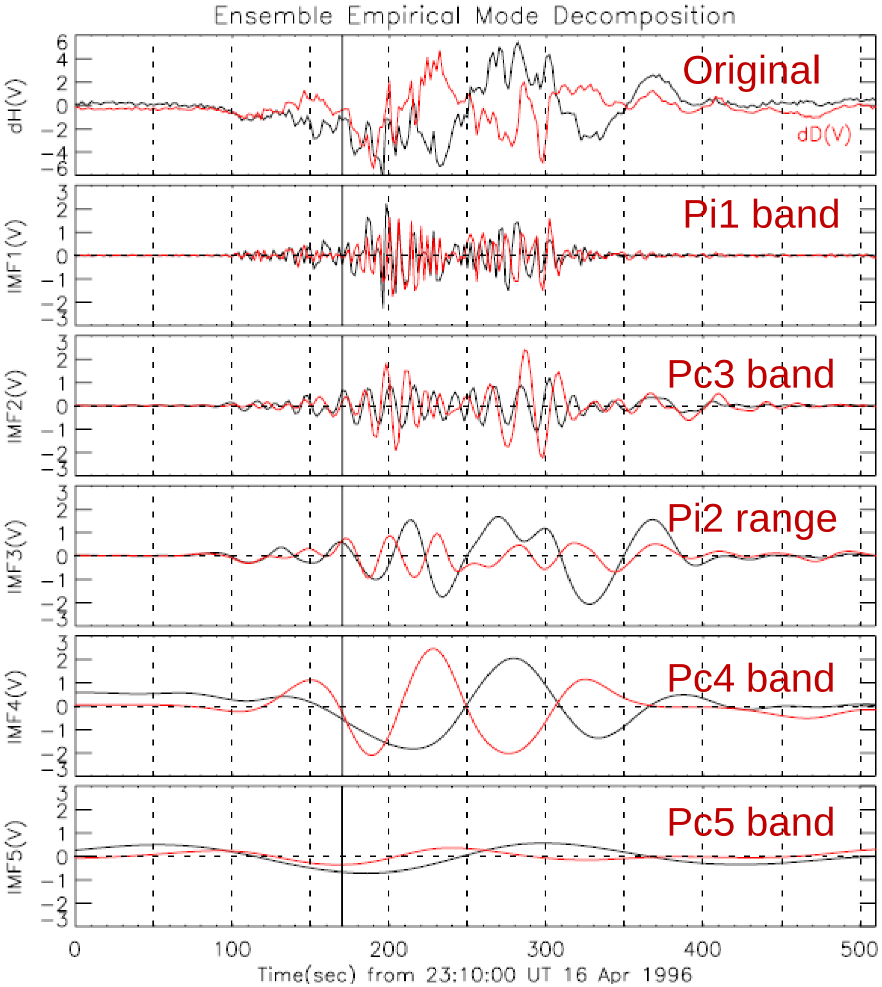

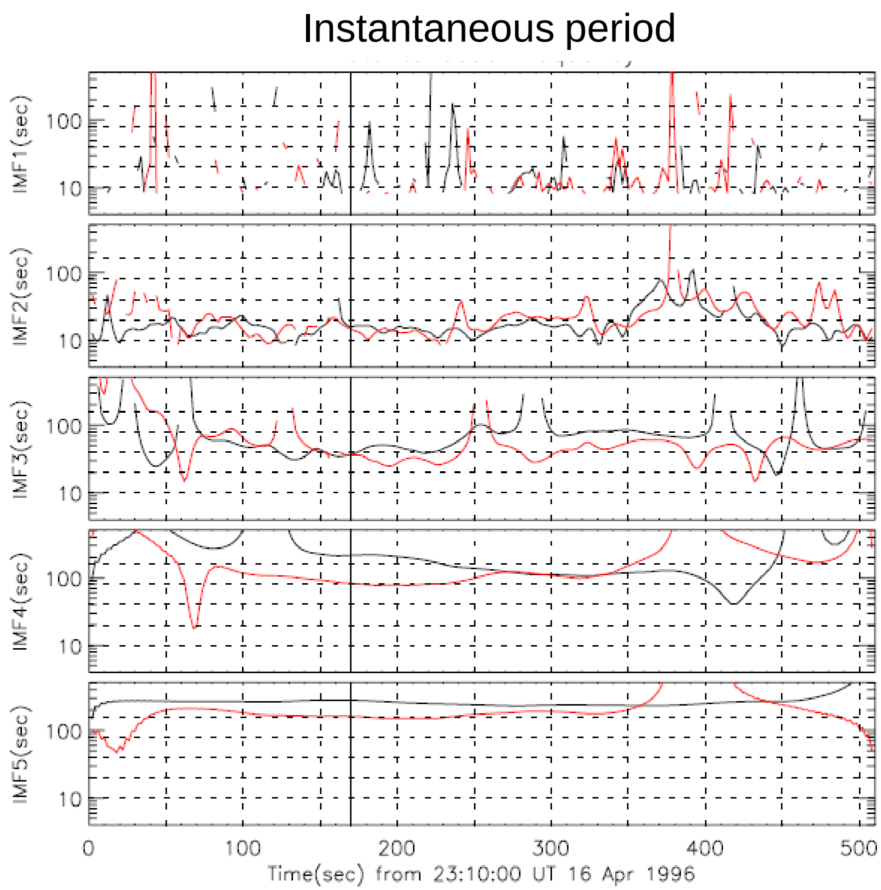

Applications – New Techniques

Wavelet-based substorm detector (AWESOME) for 1 October 2005 substorm seen with CARISMA array [Walsh et al., JGR 2010]. Contours represent time relative to auroral onset seen at GILL at 0416:00 (left) and ISLL at 0422:24 (right) overplotted onto IMAGE FUV data. Bottom panel is wavelet spectrogram from GILL. Wave onset in the Pi2 band is at 0416:00 UT.

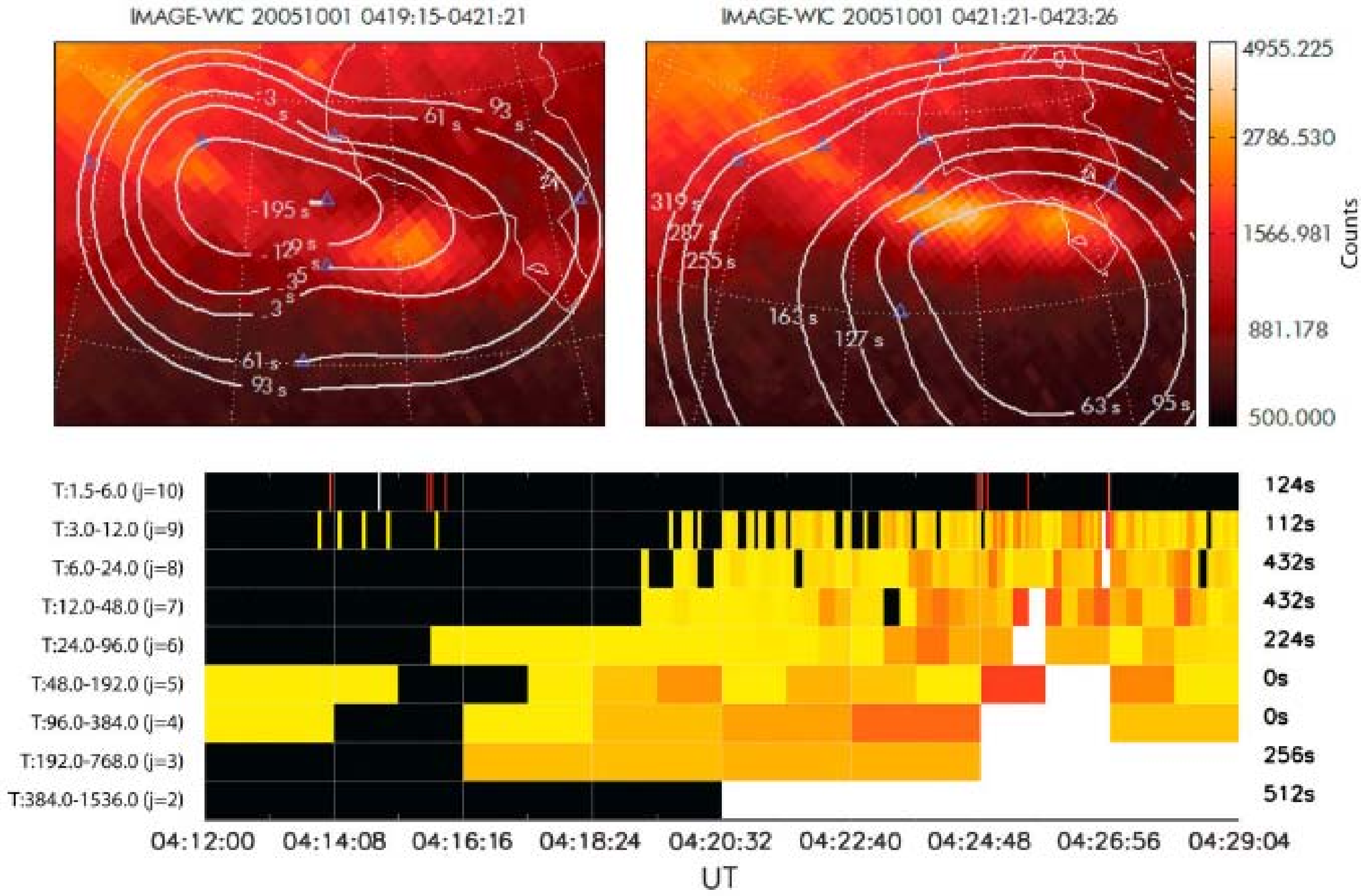

The End (for now)